NUMERICAL STUDIES OF BLACK HOLE-NEUTRON STAR BINARIES

A Dissertation

Presented to the Faculty of the Graduate School

of Cornell University

in Partial Fulfillment of the Requirements for the Degree of

Doctor of Philosophy

by

Francois Foucart

August 2011

NUMERICAL STUDIES OF BLACK HOLE-NEUTRON STAR BINARIES

Francois Foucart, Ph.D.

Cornell University 2011

Black hole-neutron star mergers are extremely energetic events with the potential to generate gravitational waves detectable by ground-based detectors. They can also form massive, hot accretion discs around a remnant black hole, which could power short gamma-ray bursts. Due to the strength of the gravitational interactions around the time of merger, black hole-neutron star binaries can only be studied in a general relativistic framework —- and as we lack analytical solutions to Einstein's equations of general relativity in the case of binary systems, numerical simulations are required to determine their evolution. In this thesis, we study black hole-neutron star binaries using the SpEC code. We show how to efficiently and accurately determine the initial conditions for numerical simulations, and study the influence on the dynamics of black hole-neutron star mergers of both the equation of state of nuclear matter — which is unknown but could be constrained through observations of compact binaries — and the spin of the black hole. We find that the dynamics of mergers is strongly affected by the radius of the star: small stars are harder to disrupt, form lower-mass discs and emit waves longer (and at higher frequency) than large stars. The component of the black hole spin aligned with the orbital angular momentum of the binary also modifies the disk formation process: high spins let the star approach closer to the black hole without plunging into it, subjecting it to stronger tidal forces and making it easier for the star to disrupt and form a massive disk.

BIOGRAPHICAL SKETCH

Francois Foucart was born in Brussels (Belgium) on August 30th 1982. The first 8 years of his life were spent in the small town of Court-St-Etienne, an hour South of the capital. His family then moved to Brussels, were Francois went to high school before starting an undergraduate degree in engineering at the Free University of Brussels. After two years he was given the opportunity to concurrently pursue an undergraduate degree at the Ecole Centrale Paris, and thus went to France. There, Francois got a first chance to get directly involved in research: international students — and even a french-speaking belgian was considered so — could replace large swaths of the school's program with which they were already familiar with a more personal project, which in this case focused on high-energy particle physics. This eventually led to an internship in CERN, and a change of course from applied sciences to theoretical physics.

Interactions with a more international crowd in Paris and Geneva also made him seriously consider moving farther away from Belgium. Back in Brussels for the last year of his engineering program, Francois applied for graduate school in the USA. A few months later, he was accepting an offer from Cornell and beginning his stay in Ithaca.

ACKNOWLEDGEMENTS

I wish to express my gratitude to all of those who have contributed to make my 6 years in Ithaca an enjoyable and enriching experience.

First of all Saul Teukolsky, whose continued help, advice and support I have greatly appreciated. The growing freedom that he allowed me over the years in setting research goals, while always remaining available and impressively knowledgeable about the research problems we faced, was extremely valuable. And the productive yet relaxed atmosphere maintained in his research group made working here a great pleasure.

My work in Cornell would also have been near impossible without the help of Larry Kidder, probably requested about 5 times a day and nonetheless always kindly given. Larry's in-depth knowledge of our code and constant input on my own research has been an extraordinary asset — only matched by his quality as a regular (and deadly) board game opponent.

It was a pleasure to work on a daily basis with other members of the SpEC collaboration: Matt Duez who begun the work on the numerical simulation of black hole-neutron star binaries to which I eventually attached myself and smoothly included me into that project, Harald Pfeiffer who was of great help during my first year in the collaboration and whom I will be glad to join next year in Toronto, Geoffrey Lovelace, Robert Owen, Curran Muhlberger, Dan Hemberger, Francois Limousin, Mark Scheel, Bela Szilagyi, Jeff Kaplan, Christian Ott and Brett Deaton.

I am thankful for the opportunity to work with Dong Lai on projects unrelated to this thesis, and to Dong himself for opening my eyes to new areas of astrophysics. Dong's ability to constantly come up with relevant ideas for new projects across a wide variety of astrophysical topics never ceased to amaze me,

and I greatly appreciated our collaboration. I also wish to thank Eanna Flanagan and Ritchie Patterson for serving on my committee.

Working in Cornell's astronomy department would not have been the same without all the graduate students who make it such a great place to be in. I am in particular grateful for Dave Tsang's enthusiasm as event organizer, and to all those who made our offices an enjoyable place to work in — and sometimes a surprising one for others to wander into.

Outside of Cornell, I wish to thank my girlfriend Erin and my family for their love and support. And I want to acknowledge the great — if not always academically productive —- influence that the wonderful residents of the Stewart Little Coop have had over my life in Ithaca.

This work was supported by the Sherman Fairchild Foundation, NSF grants Nos. PHY-0969111 and PHY-1005426, and NASA grant No. NNX09AF96G.

TABLE OF CONTENTS

LIST OF TABLES

LIST OF FIGURES

CHAPTER 1

INTRODUCTION

General relativity predicts that orbiting bodies lose energy and angular momentum through the emission of gravitational waves, an effect that has been famously observed in the Hulse-Taylor binary pulsar [51, 132]. For most astrophysical objects, these losses are too small to significantly affect their long term evolution — but in the case of compact objects (black holes, neutron stars and white dwarfs) formed at small separation, the resulting orbital decay can eventually lead to the merger of the two bodies. These mergers are the most promising sources for the direct detection of gravitational waves and will be observable by the next generation of ground-based detectors, Advanced LIGO and VIRGO [67, 30].

They are also extremely violent events : the transition from two compact stellar mass objects to the resulting single black hole or neutron star (surrounded in some cases by an accretion disc) occurs within a few milliseconds, with the potential to release very large amounts of energy. For that reason, black hole-neutron star and neutron star-neutron star binaries are amongst the most likely progenitors of short gamma-ray bursts [83] (see also [60] and references therein)— as well as remarkable laboratories for the study of physical processes in conditions unattainable within the earth's immediate surroundings : strong gravitational fields, matter above nuclear densities, large magnetic fields and neutrino radiation are all expected to play a role in these events.

With the development of large scale gravitational waves detectors came the need for a better theoretical understanding of compact binaries : the signal of a binary merger is not strong enough to be visible above the noise of the de-

tector without the help of matched filtering using gravitational wave templates. However, given the strength of the gravitational fields involved, these systems can only be described within a general relativistic framework. Unfortunately, there are no known analytical solutions to the equations of general relativity for the two-body problem. Analytical approximations to general relativity can offer a good description of the system, as long as the compact objects are widely separated. But they eventually break down over the last few orbits, and cannot describe mergers: in that regime, numerical simulations are required.

Over the last decade, our ability to solve numerically the equations of general relativity has dramatically improved. Orbiting neutron stars were first simulated within that framework in 2000 [120], while black hole-black hole [97, 8, 17] and black hole-neutron star [32, 118] binaries followed a few years later. These simulations have already offered us gravitational waveforms accurate enough for detection purposes in Advanced LIGO, as well as a better understanding of the possible qualitative behaviors of compact binary mergers. Among the surprising results obtained from these numerical simulations is the fact that, for binary black holes, mergers can result in unexpectedly large velocity kicks [19] allowing supermassive black holes to escape from low mass galaxies. For black hole-neutron star binaries, we learnt that the tidal disruption of the star and mass transfer onto the black hole can proceed very differently from what was predicted by previous simulations using approximate treatments of gravity (see Chapters 3-4).

In this thesis, we describe results from numerical studies of black hole-neutron star (BHNS) binaries in general relativity. In the rest of this chapter, we review general characteristics of BHNS systems. The formation mechanisms of

BHNS binaries and the qualitative characteristics of their merger are discussed in Section 1.1. Section 1.2 describes various ways in which they can be observed as well as the interaction between such experiments and numerical simulations, while Section 1.3 discuss the challenges associated with the numerical simulation of BHNS mergers. The following chapters deal with more specific questions related to BHNS systems. Chapter 2 describes the construction of initial data for the evolution of BHNS binaries. Chapter 3 discusses how the equation of state of the neutron star matter influences the dynamics of BHNS mergers, affecting both the gravitational waveform and the disruption of the star. Chapter 4 shows the effects of the black hole spin on BHNS mergers, and particularly the large influence it can have on the formation of a remnant accretion disc.

1.1 Black Hole-Neutron Star binaries

1.1.1 Formation and characteristics

The formation of black hole-neutron star binaries in tight orbits is a complex problem. Population synthesis codes make predictions about the evolutionary pathways that may lead from two main sequence stars in a binary system to a BHNS merger, but their accuracy remains severely limited by our ability to model complex physical events such as supernova explosions, the core-collapse of massive stars or mass transfer episodes, as well as uncertainties in the initial mass function and composition of stars in binaries [12]. A lower bound for the formation rate of binary neutron stars can be derived from observations of galactic binaries — but the lack of direct observation of black holes in compact binaries makes it impossible to do the same for binary black holes or BHNS bi-

naries. The theoretical uncertainties in the rate of BHNS mergers are thus fairly large: predictions from the LIGO collaboration [106] estimate that Advanced LIGO will detect about 10 BHNS mergers each year - but with a lower bound as low as 1 event every 5 years, and an upper bound of an event every day.

Core-collapse and black hole formation

One of the main source of errors in our understanding of the formation of BHNS binaries is the parametrization of core-collapse events. Main sequence stars in the mass range $10 - 20 M_\odot$ (where $M_\odot$ is the mass of the sun) are expected to create neutron stars through core-collapse supernovae, while heavier stars form black holes. In the case of black hole formation, two scenarios are possible. The core can directly form a black hole, in which case the amount of matter ejected during core-collapse is negligible and no velocity kick is imparted to the remnant black hole. But the collapse can also be delayed by the temporary formation of a protoneutron star, in which case a shock wave is still launched. If enough energy is available, part or all of the stellar envelope can then be ejected, and asymmetries in this ejection process give a velocity kick to the black hole.

Scenarios in which no matter is ejected during core-collapse are more likely for heavier stars, but a direct map between main sequence stars and core-collapse scenarios remains elusive: results depend heavily on the properties of the stellar envelope and on the model chosen for the strong stellar winds that are expected to be launched by such massive stars — as well as on the initial composition of the star itself [79]. However, this information is crucial to determine whether the system can form a BHNS binary. If the black hole is given a significant kick, the most likely outcome is a disruption of the binary: most black holes

in tight binaries are thus expected to be formed from "silent" core-collapse, in which no matter is ejected [12]. As heavier stars are much less common, the stellar mass at which "silent" core-collapse is possible is an important parameter in the determination of the event rate of BHNS mergers.

The physics of core-collapse events can also affect significantly the expected characteristics of BHNS binaries. Mass transfer events following black hole formation probably only slightly modify the mass and spin of the black hole [12]: these important parameters, whose influence is discussed in more detail in Section 1.1.2 and Chapter 4, are thus mostly determined by the results of core-collapse. As the mass distribution of main sequence stars favors lighter stars, most black holes in compact binaries are expected to have a mass close to the minimum mass allowing "silent" core-collapse. Belczynski et al. [12] estimate this to be around $10M_{\odot}$, in which case the favored mass ratio for BHNS binaries would be about 1:7. However, the exact value clearly varies with the choice of core-collapse model.

The spin of the black hole is even less constrained. Numerical simulations of core-collapse events are only beginning to probe BH spins [80], and do not follow their evolution long enough to accurately predict their final value. Observational measurements of black hole spins are still controversial, though current results seem to indicate that a wide variety of natal spins are possible [73] — leaving a fairly wide available parameter space.

It is also worth noting that, at this point in the evolution of the system, these spins are likely to be aligned with the orbital angular momentum of the binary: lacking an asymmetric supernova explosion, there is no reason to believe that the equatorial symmetry of the system should be broken.

Giant phase and mass transfer

Once a black hole has formed without unbinding the binary, the next uncertain phase is the evolution of the lighter companion (which, eventually, will form a neutron star) through its giant phase. For systems with tight enough orbits that they might eventually lead to a BHNS merger, the companion is expected to grow large enough for a common envelope to form around the binary. Our theoretical understanding of this phase is limited. It is expected that mass transfer from the companion onto the black hole occurs, and that the orbit of the binary tightens. The angular momentum lost by the binary is deposited in the stellar envelope, which is expelled. As this phase is short enough that the total mass accreted onto the black hole remains small ($\sim 0.1 - 0.3 M_{\odot}$), the ability of the common envelope phase to modify the mass and spin of the black hole is severely limited [12]: the effect of the common envelope phase on the population of BHNS binaries is mostly to help decrease the orbital separation of the binary, thus placing it in a configuration more likely to lead to a merger after the neutron star forms.

Neutron star formation

The final phase in the formation of a BHNS binary is the core-collapse event resulting in the formation of a neutron star. As opposed to black hole formation, for which we expect "silent" core-collapse to be the standard pathway towards BHNS binaries, the formation of a neutron star follows a supernova explosion in which most of the stellar envelope is expelled from the system. Thus, the resulting neutron star is likely to receive a velocity kick that can unbind or disrupt the binary. For studies of BHNS systems, this modification of the orbital

characteristics of the binary means that on top of the uncertainty regarding the magnitude of the black hole spin, we have to take into account the possibility that this spin is misaligned with respect to the orbital angular momentum of the system: the velocity kick is not constrained to be in the equatorial plane of the binary, and the inclination of the orbit will thus generally be modified by the explosion. As small velocity kicks are less likely to unbind the binary, relatively small misalignment angles are more common: Belczynski et al. [12] predict that for an initial black hole spin $S = 0.5M^2$, more than half of the systems will be misaligned by less than 40°. For relatively low mass black holes ($\sim 5M_\odot$), we show in Chapter 4 that the effects of spin misalignment are weak unless the spin is misaligned by more than $\sim 40^\circ$ — but these effects are likely to be larger for higher mass black holes.

The rotation speed of the neutron star is probably less important than the black hole spin — though it is also better constrained. Pulsars with spin frequencies up to $716\mathrm{Hz}$ have been observed [49], but most neutron stars have significantly slower rotation. As the orbital period of BHNS binaries is only a few ms at the time of merger, the spin of the neutron star is likely negligible in most astrophysical configurations. This would not be the case if the rotation period of the neutron star was tidally locked to the orbital period of the binary. However, the gravitational decay time in BHNS binaries is too short for tidal locking to be possible (regardless of the value of the viscosity inside the neutron star) [13]. Most studies of BHNS mergers thus limit themselves to the case of irrotational neutron stars, corresponding to the case of no spin-up from the initial negligible spin.

A more relevant parameter for BHNS mergers is the size of the neutron star.

The radius of a neutron star is a direct consequence of the equation of state of cold matter above nuclear density — which is currently a theoretical unknown. And it has significant consequences on the dynamics of BHNS mergers, in particular on the disruption of the neutron star (see Section 1.1.2 and Chapter 3). Observational constraints on neutron star radii are improving, but the interpretation of these experimental results remains difficult and controversial: from similar observations of X-ray bursts in pulsars, but using different assumptions for the physics of X-ray bursts and the atmosphere of neutron stars, Ozel et al. find fairly compact neutron stars ($R \sim 10\mathrm{km}$) [82], while Suleimanov et al. find incompatible lower limits $R > 14\mathrm{km}$ [126]. As for theoretical models, they span a similarly large range of radii. Using constraints from calculations of the equation of state of neutron-rich matter at low density, Hebeler et al. have recently argued that the radius of a $1.4M_{\odot}$ neutron star should be in the range $R_{\mathrm{NS}} = 9.7 - 13.9\mathrm{km}$ [48] — the strongest constraint today that does not use any information from the more controversial astrophysical measurements.

1.1.2 Mergers

Dynamics of BHNS mergers

As discussed in the previous section, the possible initial configurations of BHNS binaries are only partially constrained — in part because of theoretical uncertainties (determination of the most likely black hole mass, nuclear equation of state), and in part because of the physically available phase space (BH spin magnitude and orientation, neutron star magnetic fields, distribution of black hole masses,...). However, the value of theses initial parameters can significantly af-

fect the qualitative behavior of BHNS mergers, which is mainly determined by the strength of the tidal forces distorting and, in some cases, disrupting the neutron star.

For a massive body orbiting a black hole, the emission of gravitational waves causes the orbit of the particle to shrink slowly over time. As gravitational wave emissions also decrease the eccentricity of the orbit, we expect that towards the end of that process the orbit is nearly circular — regardless of the initial eccentricity of the binary (at least in the field : eccentric BHNS mergers might still be possible in globular clusters [124]). For point particles, stable circular orbits only exist a few Schwarzschild radii away from the black hole ($3R_S$ for a nonspinning black hole). When the point particle reaches the innermost stable circular orbit (ISCO), it plunges quickly into the hole. A similar behavior is expected for binary black holes : the holes spiral in following quasi-circular trajectories, until they are separated by only a few Schwarzschild radii. Then, they plunge towards each other, and merge into a single black hole.

The situation is more complex when one of the orbiting objects is of finite size. Tidal forces then distort the extended object (here, the neutron star). For fixed black hole and neutron star masses, these forces are stronger for smaller orbital separations and larger stars. Eventually, the tidal forces can be strong enough that the star no longer fits within its Roche lobe (the spatial region within which matter is gravitationally bound to the star). Then, an accretion flow transferring matter from the star to the black hole is created, together with a tidal tail containing matter ejected from the outer region of the Roche lobe (that matter can be either unbound, or launched on bound but extremely eccentric orbits). This is the configuration shown on the left panel of Fig. 1.1.

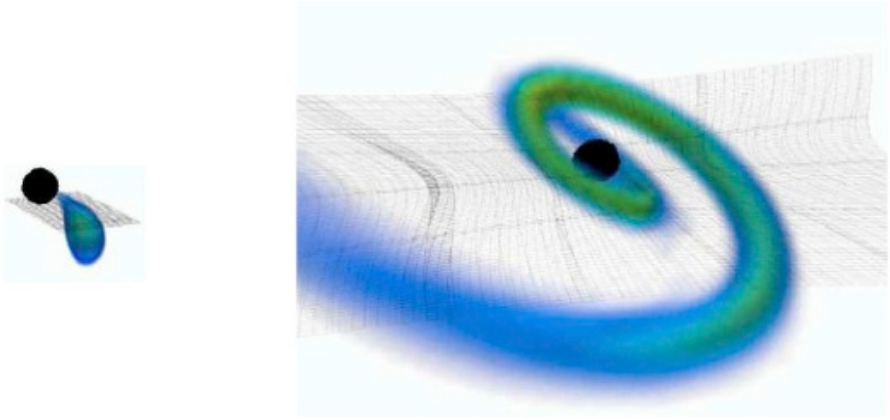

Figure 1.1: Tidal disruption of a BHNS binary : numerical simulation. *Left :* Disruption of the neutron star. *Right :* Formation of an accretion disc.

From this picture three different scenarios are a priori possible, though only two are observed in practice in simulations using an exact treatment of the general relativistic equations:

- The neutron star is too compact for tidal interactions with the black hole to have a significant effect before the star plunges towards the hole, and all the matter falls rapidly into the black hole. The binary behave approximately like binary black holes with similar masses.
- Tidal forces are strong enough for the star to overflow its Roche lobe while still orbiting the black hole. The disrupted star forms both an accreting flow onto the black hole and a trailing tidal tail. If mass transfer onto the black hole is unstable, most of the neutron star matter then rapidly accretes onto the black hole, while the rest divides itself into a forming accretion disc, bound matter on eccentric orbits in a tidal tail extending far away from the black hole and falling back over longer timescales ($\sim 1s$), and unbound ejecta. This is the final state shown on the right panel of Fig. 1.1.

- As before, the star overflows its Roche lobe — but mass transfer is now stable. During mass transfer, the orbital separation of the binary grows to the point where the neutron star once more fits within its Roche lobe, and accretion temporarily stops. Such episodes of stable mass transfers are known to occur for larger stars, and were originally predicted to be possible for BHNS binaries in circularized orbits. However, these early simulations used an approximate treatment of gravity. Simulations in full general relativity(GR) always find unstable mass transfer for BHNS binaries on low-eccentricity orbits (see Chapter 3 for more details).

The influence of the various parameters of the binary on that competition between tidal disruption and orbital plunge can easily be seen on the schematic representation of the various physical processes given in Fig. 1.2. The neutron star (in blue) and the black hole (in black) are represented at a separation such that the surface of the neutron star reaches the minimum radius at which elliptical orbits bound to the black hole exist (radius of the marginally bound orbit, the dashed line). This distance (as the ISCO, which lies slightly farther away from the hole), is proportional to the mass of the black hole and smaller when the component of the black hole spin aligned with the angular momentum of the orbit is large. The radius of the marginally bound orbit represents the smallest radius from which particle expelled in the tidal tail can fall back onto the black hole and form a bound accretion disc, while the ISCO corresponds to the beginning of the orbital plunge.

This spin dependence means that for large spins the star can fall deeper into the gravitational potential of the black hole before the plunge begins. It will thus experience stronger tidal forces, and be more likely to be disrupted (and

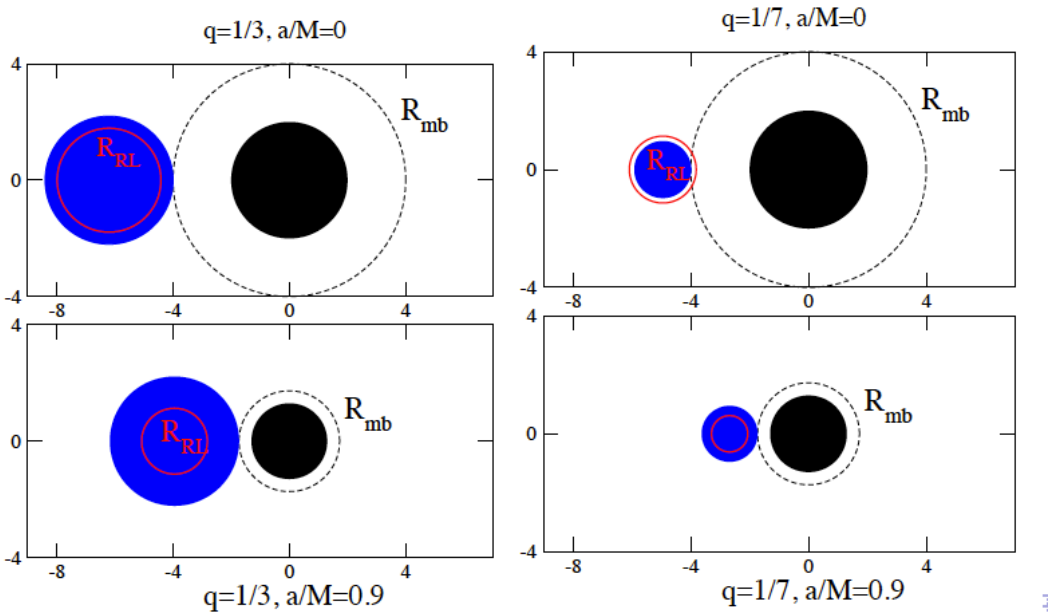

Figure 1.2: Strength of tidal effects in BHNS binaries at the time of merger for different mass ratios and BH spins. The neutron star (in blue) is represented at the time at which it reaches the radius of the marginally bound orbit (dashed line - the smaller radius for which particles can be in bound orbits around the BH). The red circle represent the average radius of the star's Roche lobe (Newtonian value), an indicator of whether tidal effects can disrupt the star and induce mass transfer / tidal tail formation. *Top Left:* Mass ratio of 1:3, non spinning BH; *Bottom Left:* Mass ratio of 1:3, BH spin $S = 0.9M^2$; *Top Right:* Mass ratio of 1:7, non spinning BH; *Bottom Right:* Mass ratio of 1:7, BH spin $S = 0.9M^2$.

form a massive disc and tidal tail). The strength of these tidal forces can be approximated by the ratio between the average size of the Roche lobe $R_{\rm RL}$ and the radius of the star $R_{\rm NS}$. In Newtonian physics, we have

$$\frac{R_{\rm NS}}{R_{\rm RL}} \sim \left(\frac{R_{\rm NS}}{M_{\rm NS}}\right)\left(\frac{M_{\rm BH}}{D_{\rm bin}}\right) q^{1/3}(1+q)^{2/3} \tag{1.1}$$

where $M_{\rm BH}$ is the mass of the black hole, $D_{\rm bin}$ is the orbital separation, and $q = M_{\rm NS}/M_{\rm BH}$ is the mass ratio. Mass transfer occurs for $R_{\rm NS}/R_{\rm RL} \gtrsim 1$. This average size of the Newtonian Roche lobe is represented in red in Fig. 1.2. Naturally,

this shows that larger stars are more likely to overflow their Roche lobe and be disrupted. It also indicates a significant dependence in the mass ratio q. For small mass ratios (i.e. large black hole masses), tidal forces are less efficient and disruption of the neutron star is less likely.

From this simple analysis, we can thus estimate that:

- Black holes spins with a large component aligned with the orbital angular momentum delay the plunge of the neutron star, and favor tidal disruption and accretion disc formation.
- Large neutron star radii allow tidal disruption at larger orbital separation, thus making accretion disc formation easier.
- Small black hole masses help Roche lobe overflow (though the above picture breaks down when the black hole and the neutron star have nearly equal masses).

These are, however, only trends. The transition point between plunge and tidal disruption, as well as the mass of the accretion disc or the orbital separation at which disruption occur, can only be obtained through numerical simulations performed in a GR framework. Additionally, other important characteristics of BHNS mergers cannot be properly described by simple Newtonian analogies, or even numerical simulations using approximate treatments of gravity. The stability region for mass transfer, for example, is different in general relativity. And when disruption occurs, Newtonian simulations predict the formation of larger accretion discs — though discs as large as $0.5M_{\odot}$ can form around rapidly spinning black holes in GR simulations (see Chapter 4). GR simulations also predict that the amount of unbound material ejected during the tidal disruption

of the star is negligible while non-GR simulations found massive neutron rich ejecta ($\sim 0.1 M_{\odot}$) — enough to contribute significantly to the formation of heavy elements in the universe through the r-process.

Nevertheless, these general trends have been confirmed by GR simulations, and give a good indication of the most important parameters to vary : the mass and spin (along the orbital angular momentum) of the black hole (see Chapter 4 and Appendix D), and the radius of the neutron star (see Chapter 3). Details of the nuclear equation of state beyond the neutron star radius, even though they affect the mass transfer and disc formation, are less relevant than the size of the star (Chapter 3). Components of the black hole spin misaligned with the orbital angular momentum cause precession of the orbit, which is observable in the gravitational wave signal — but they do not change significantly the qualitative behavior of the tidal disruption beyond the fact that both the tidal tail and the forming accretion disc will be misaligned with the black hole spin, at least for low mass black holes (Chapter 4). Other microphysical effects such as magnetic fields and neutrino radiation are expected to play an important role in the evolution of the final remnant over longer timescales, but their effect on the pre-merger dynamics is usually negligible (except for unrealistically large magnetic fields $B \gtrsim 10^{17} G$, as shown for orbiting binary neutron stars by Giacomazzo et al. [44]).

The final remnant

Numerical simulations have shown that the merger of a BHNS binary can have two different outcomes. One possibility is that the star plunges into the black hole as a solid body, and the post-merger remnant is simply a distorted black

hole that rings down rapidly towards a static solution as is the case in the merger of binary black holes systems. The other possibility is that the star is disrupted before the plunge, leaving a significant amount of matter outside of the black hole — in which case the post-merger configuration remains a complex system with the potential to emit energetic electromagnetic and neutrino radiation over longer timescales $\sim 1s$. Material in the tidal tail has too much angular momentum to simply fall back onto the black hole. Instead, the tidal tail forms an accretion disc which accretes at a super-Eddington rate onto the hole, while being more slowly replenished by material from the tail falling back towards the black hole. Because of the large amounts of energy available in the disc, as well as the likelihood that these remnants could launch ultra-relativistic jets in the presence of magnetic fields, such remnants are amongst the most likely progenitors of short gamma-ray bursts (see Sec. 1.2.2). They are also significantly more complex to simulate numerically than binary mergers. Simulations in full GR are required (at least until the metric approaches a quasi-stationary configuration), and physical processes that could be neglected before — such as magnetic fields and neutrino cooling — are now crucial elements in their evolution. Additionally, the evolution of the system has to be followed over significantly longer timescales.

Current numerical codes are unable to carry a simulation encompassing all the physical effects relevant to the evolution from an orbiting BHNS binary to a gamma-ray burst — though progress towards the inclusion of more realistic microphysics in existing GR codes is bringing us closer to that goal. What recent results do offer is an understanding of which systems create a significant accretion disc (as discussed in the previous section), and what the initial characteristics of that disc are.

The amount of matter available for disc formation varies widely with the mass ratio and black hole spin considered, but is typically of the order of $0.1 - 0.2 M_{\odot}$ when disruption does occur (more for very high spins). Part of that matter is in a thick accretion disc ($H/r \sim 0.2$, where H is the half-thickness of the disc), brought to high temperatures through shock heating ($T \gtrsim 1\mathrm{MeV}$). The rest is in a cold tidal tail, with material slowly falling back and feeding the accretion disc. In GR simulations, nearly all of the material in that tail is gravitationally bound to the black hole. The exact amount of unbound ejecta could be affected by inaccuracies in the evolution of the low-density regions, as well as by neglected physical effects (e.g. reheating from nuclear reactions), but is likely to remain small compared to the mass of the accretion disc. Typically, the accretion timescale for the disc material is initially of order $0.1s$. However, the velocity profile of the disc indicates that it should be subject to the magnetorotational instability(MRI), which grows over much shorter timescales [43]. It is thus clear that the long-term evolution of the accretion disc, as obtained in the absence of magnetic fields, cannot be trusted. Including magnetic fields and, probably, neutrino radiation (the leading source of cooling in such a disc) is required to study them further — as well as to extract information on potential observable counterparts to the gravitational wave signal of BHNS mergers.

1.2 Observational motivations

1.2.1 Gravitational waves

As opposed to binary neutron stars, which have been observed directly within the Milky Way, BHNS binaries remain undetected. But the next generation of gravitational wave detectors should allow us to fill that void. Detection of the gravitational waves emitted by compact objects is a very delicate measurement: the Advanced LIGO detector, composed of 4km long interferometers located in Hanford (WA) and Livingston (LA), should be sensitive to relative variations $h \sim 8 \times 10^{-23}$ in the length of its arms in the $100\mathrm{Hz}$ band [67]. By working jointly with the VIRGO detector (Italy) [30], it could observe BHNS binaries up to distances of about $1\mathrm{Gpc}$, as long as the signal can be extracted by matching it to an analytical waveform — that is, one known a priori [106]. The event rate for those mergers, as already mentioned, is fairly uncertain. In fact, knowledge of the event rate would already provide interesting constraints on population synthesis models.

Advanced LIGO and VIRGO will offer a direct measurement of the existence of gravitational waves, which have until now only been observed through their effects on the orbital evolution of binary systems — a remarkable feat in itself. But the information that we might be able to extract from gravitational wave astronomy goes significantly farther than simply a more direct proof of existence. It offers an entirely new way to observe the universe : from the big bang to compact binaries and supernovae explosions, gravitational waves offer a new way to approach observational astronomy and cosmology.

The gravitational waves emitted by orbiting BHNS binaries cover most of the LIGO band, with the merger expected to occur at frequencies of order $1\mathrm{kHz}$. The merger is thus at frequencies slightly out of the most favorable LIGO band (see Fig. 1.3). There are plans to tune Advanced LIGO's frequency response to study the kHz region with more accuracy once detections are routine. Nevertheless, the gravitational waves from orbiting BHNS binaries at lower frequencies should already contain a wealth of information on the physical characteristics of BHNS systems : masses, spins and even the equation of state all leave their imprint on the waveform. However, it is not clear whether the current accuracy of theoretical waveforms would allow us to perform parameter estimates from Advanced LIGO waveforms : the precision required for such measurements is much higher than what is needed for detection purposes.

For theoretical waveforms obtained by matching an analytical approximation (valid at large separation) to a numerical waveform (computed at small separation), there are mainly two sources of error : the error contained in the analytical approximation, which increases if the matching is done at a smaller separation, and the numerical error from the simulation, which for a given numerical resolution increases with the length of the simulation. Recent studies of the error in such hybrid waveforms indicate that current numerical simulations are probably too short for accurate parameter estimates [15, 72]. It thus seems unlikely that the gravitational wave signal from orbiting compact binaries will offer more than a rough estimate of the parameters of the system without significant improvements to numerical waveforms.

In the case of BHNS mergers, another important source of information comes from the gravitational wave signal emitted around the time at which the star is

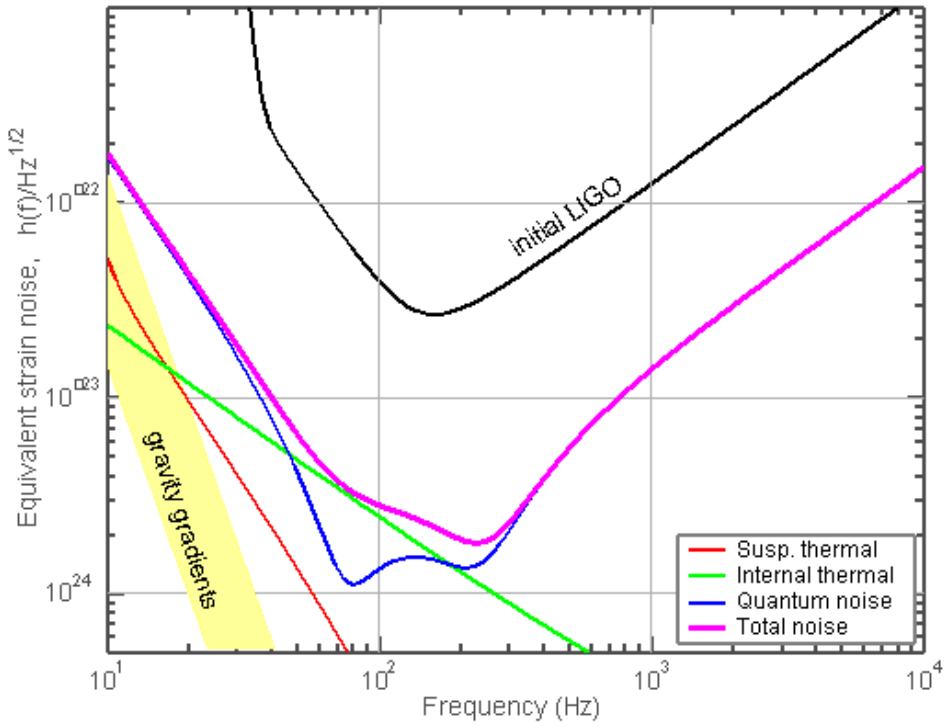

Figure 1.3: Noise curve of the Advanced LIGO detector, as given on the LIGO website [67]

tidally disrupted. The orbital separation at which this disruption occurs is a function of the spin of the black hole, the masses of the compact objects, and the radius of the neutron star. As tidal disruption of the star causes an abrupt cutoff in the gravitational wave emission, with the amplitude of the waves rapidly decreasing at higher frequencies, it offers a fairly sensitive measurement of the parameters of the binary.

For binary neutron stars, Read et al. [100] estimate that disruption would allow measurements of the neutron star radius with an accuracy of $\Delta R \sim 1\mathrm{km}$ for a system optimally oriented at a distance of $100\mathrm{Mpc}$, if we use Advanced LIGO in either its 'broadband' (optimized for burst searches) or 'narrow-band' (optimized for pulsar detection) configuration —- both of which have reduced noise

in the high-frequency regime compared with the 'standard' configuration optimized for the detection of NS-NS binaries. The waveforms of BHNS binaries have not been as extensively studied— but the larger range of masses and spins expected in such systems is likely to complicate these measurements. From their study of the gravitational waves emitted by a range of BHNS binaries (with nonspinning black holes), Shibata et al. [117] argue that a detector with better sensitivity at high frequencies than Advanced LIGO will be needed to extract useful information from the cutoff frequency in the gravitational waves emitted by BHNS mergers.

Gravitational wave astronomy is thus an exciting new field of study, which will only begin to offer results in the upcoming years. Detections of compact binaries through gravitational waves will be possible soon — and offer early constraints on population synthesis models. But accurate parameter estimates, which would offer important information on the results of supernova explosions and stellar core-collapse as well as constraints on the equation of state of matter above nuclear densities, will likely have to wait for improvements to both detector technology and numerical simulations.

1.2.2 Short gamma-ray bursts

Gamma-ray bursts (GRB) were first observed in the 1960's by the Vela satellites, gamma-ray detectors originally built by the US for the detection of nuclear tests by the USSR. This discovery, along with the fact that the bursts were not of solar system origin, was only made public in 1973 [55]. More detailed studies of GRBs had to wait for the results of the BATSE instrument aboard the

Compton Gamma Ray Observatory (1991-2000) and, more recently, the HETE-2 (2000-2006), SWIFT (2004) and FERMI (2008) experiments.

BATSE offered the first catalogue of GRBs. From the isotropic distribution of sources, it was deduced that GRBs were probably of extra-galactic origin [74]. This theory was confirmed in recent years: the SWIFT telescope is equipped with an X-ray detector that can determine the sky location of GRBs (through their X-ray afterglow) with enough accuracy to allow optical follow-ups. From these follow-ups, it has been possible to determine the host galaxies of some GRBs (see [65] and references therein).

GRBs are the most energetic events observed in the universe ($10^{48} - 10^{51}\mathrm{ergs}$). Since the results of the BATSE experiment, they have been typically divided into two classes: long bursts, which last more than 2s and have softer spectra, and short bursts, which last less than 2s and have harder spectra [57]. This classification is still widely used today, although the distinction between the two classes is not always clear, and the need for a third class has been suggested [50]. Long gamma-ray bursts, which are the most frequent, are located in star forming galaxies and are generally associated with core-collapse supernovae (see [135] for a review). Short gamma-ray bursts (SGRB), on the other hand, have been observed in old elliptical galaxies and can only be explained through an older population of stars. Given the energies involved and the population they are associated with, the most likely progenitors for SGRBs appear to be the mergers of binary neutron stars and BHNS binaries [65].

How exactly to get from the merger of a BHNS or a NS-NS binary to a short gamma-ray burst remains unexplained. A central engine composed of a spinning black hole and a massive accretion disc has the potential to release large

amounts of energy through winds, collimated jets, neutrino radiation and electromagnetic radiation [65]. In simulations of binary neutron stars, the growth of collimated field lines along the rotation axis of the central remnant has been observed and could help the creation of a collimated ultra-relativistic outflow and a SGRB [102]. Simulation of the outflow itself is still beyond the reach of these numerical simulations, because of the low densities involved, but these results give a first indication that large ordered magnetic fields can grow when the remnant of binary neutron star mergers are evolved over a long enough timescale : in Rezzolla et al. [102], the field grows from a turbulent magnetic field $B \sim 10^{12}G$ to a poloidal field $B \sim 10^{15}G$ over about 35ms.

More generally, GR simulations of compact binaries have shown that a broad class of systems (for both BHNS and NS-NS) can lead to a final remnant with strong potential to be a SGRB progenitor. The discs described in Sec. 1.1.2, and studied in more detail in Chapters 3-4, are a priori capable of powering such bursts, as are those observed in NS-NS simulations. As more realistic microphysical effects are added to these numerical simulations, it should become possible to shed light on at least some of the channels allowing the creation of SGRBs, and to constrain the initial conditions for which compact binaries can create them.

1.3 Numerical Relativity

Numerical simulations of compact object binaries are necessary to obtain accurate gravitational waveforms for the last orbits before merger, as well as to get reliable information about the qualitative features of the merger itself : analyt-

ical approximation to the equations of general relativity are only accurate for large orbital separations, and numerical evolutions can give misleading results when an approximate form of Einstein's equations is used (see Sec. 1.1.2-1.2). However, Einstein's equations as written in their original form are not suitable for numerical evolutions — alternative formulations had to be derived for GR simulations to be feasible. Additionally, Einstein's equations impose constraints on the evolved metric variables (similar to the requirement in Maxwell's equations that $\mathrm{div}\boldsymbol{B} = 0$ at all times). If the constraints are satisfied at the initial time and the evolution is exact, Einstein's equations guarantee that the constraints remain satisfied at later times. However, numerical simulations have finite accuracy: the constraints will not be exactly satisfied, and constraint-violating mode may grow rapidly. This introduces an additional complication to numerical evolution: the growth of constraint violating modes has to be controlled.

The existence of these constraints also means that the computation of initial data for simulations in GR is not trivial: the initial data itself has to satisfy the constraints, while representing a configuration that is astrophysically relevant.

In Section 1.3.1, we discuss some important issues regarding the determination of the initial configuration used in GR simulations — a topic that is studied in more detail in Chapter 2. Section 1.3.2 then offers an overview of the methods used in our simulations of compact binaries for the stable evolution of Einstein's equations as well as issues specific to the evolution of fluids in GR.

1.3.1 Initial data

The initial data for GR simulations has to satisfy two types of constraints : the mathematical constraints required for the initial data to be compatible with Einstein's equations, and the astrophysical constraints used to make the initial data correspond to a realistic situation.

The choice of initial data is typically made using the 3+1 decomposition, in which spacetime is foliated by 3-dimensional spatial hypersurfaces parametrized by a time coordinate t. The metric is then

$$ds^2 = -\alpha^2 dt^2 + \phi^4 \tilde{\gamma}_{ij} \left(dx^i + \beta^i dt\right) \left(dx^j + \beta^j dt\right), \tag{1.2}$$

where α is the lapse, ϕ the conformal factor, $\tilde{\gamma}_{ij}$ the conformal 3-metric and β^i the shift. The mathematical constraints on the metric components on a surface of constant t can then be written as a set of elliptical equations of the type

$$\nabla^2 \phi = ... \tag{1.3}$$

$$\nabla^2 (\alpha\phi) = ... \tag{1.4}$$

$$M^{ijk} \nabla_i \nabla_j \beta_k = ... \tag{1.5}$$

where the right-hand sides are functions of the stress-energy tensor and the metric variables and their derivatives (see Section 2.2.1 for a more detailed discussion of the constraints). In this formalism, the free parameters for the initial data are the conformal metric $\tilde{g}_{ij}$, the trace of the extrinsic curvature K_{ij} ($\sim$ the derivative of the metric along the normal to the spatial slice, see eq. [2.9]), and their derivatives along the 'time' coordinate t. These freely specifiable functions, combined with a choice of boundary conditions for the variables α, ϕ and β^i, will determine the physical properties of the initial configuration.

In the case of a binary system, it is fairly natural to require that the time derivatives vanish in the coordinate frame comoving with the compact objects (quasi-equilibrium condition). This assumption would be exact for a binary in circular orbit in the absence of gravitational radiation, and remains very accurate except during the plunge. Let us note, however, that this condition fixes the time derivatives of the free variables but introduce a new freedom: the choice of the comoving frame. We generally choose a frame rotating at constant angular velocity Ω and with a radial velocity $v_r = ar$. Ω and a then determine the eccentricity and orbital phase of the binary.

Choosing $\tilde{g}_{ij}$ and K is more difficult. We use either flat space ('conformally flat' initial data), or some superposition of analytical solutions for isolated objects. However, neither of these choices is exact for a binary with finite orbital separation. In practice, this means that in numerical simulations the binary will relax from the chosen initial data to a more physical quasi-stationary orbit — usually through quasi-normal ringing of the black hole(s), the emission of 'unphysical' gravitational waves, and/or oscillations in the star(s). Reducing the importance of these unphysical effects and choosing the initial parameters so that the final configuration corresponds to a binary with the desired physical parameters (mass and spin of the compact objects, orbital parameters) is one of the main challenges in our choice of initial data.

For BHNS and NS-NS binaries, an additional complication comes from the necessity to determine the initial value of the matter fields (density ρ, temperature T, velocity u_i). The assumption of quasi-equilibrium allows us to determine the density : the requirement that the matter fields are constant in the comoving frame turns out to give an algebraic relation between the metric and matter

fields, up to a constant fixing the mass of the star. The temperature can quite naturally be set to $T = 0$, as the temperature in the star is expected to be negligible compared to the Fermi energy of the degenerate neutrons. The velocity, however, has to be solved for: the requirement that the fluid in the star is in an irrotational configuration gives us an elliptic equation for the velocity potential Ψ, where $\nabla_i \Psi \sim u_i$.

Finally, the equations for the metric and the matter fields are coupled: ρ and Ψ are source terms in the elliptic equations for α, ϕ and β, while knowledge of the metric is required to solve for Ψ and ρ. Solving the whole system thus requires the following ingredients:

- An elliptic solver to find the constrained metric variables α, ϕ and β as well as the velocity potential Ψ, when the source terms of the various elliptic equations are known.
- A prescription for the free functions $\tilde{g}$, K and their time derivatives, so that the initial data is as close as possible to the desired physical configuration.
- An iterative procedure allowing us to solve the coupled problems of satisfying the constraints (5 elliptic equations), determining the fluid velocity (1 elliptic equation), and finding the matter density within the star (1 algebraic equation with a free parameter chosen iteratively so that the star has the desired mass). The procedure must converge towards a self-consistent solution with the desired physical properties.

Chapter 2 details the numerical methods used to choose initial data for our simulations, and presents tests of the accuracy of the algorithm. We verified that at large orbital separations our results agree with analytical approximations to

Einstein's equations, as well as with previous numerical results by Taniguchi et al. [131]. Through the use of spectral methods we obtained exponential convergence for the solution, at least in the case of simple equations of state. We also adapted methods used for binary black holes to obtain low-eccentricity orbits [88] and high spin [69] to black hole-neutron star systems. The resulting algorithm is thus capable of efficiently generating accurate initial data for a wide range of black hole-neutron star systems, with orbital parameters reproducing the most likely astrophysical configurations.

Increased accuracy requirements as well as the need to generate initial data for misaligned black hole spins led to regular improvements to the initial data solver after the publication of Chapter 2. These recent modifications are discussed in Appendix A.

1.3.2 Numerical Evolutions

The numerical simulation of black hole-neutron star binaries requires the evolution of two sets of coupled equations, each with its own numerical challenges. First, we have to solve Einstein's equations — a set of 10 nonlinear second order differential equations that, in their original formulation, are not well adapted to numerical evolutions. Then, we have to evolve the relativistic hydrodynamics equations in such a way as to properly handle the shocks that may appear in the fluid, as well as other discontinuities such as the surface of the star. In the following sections, we briefly describe each set of equations as well as the methods used to solve them. Then, we present the algorithms chosen in the SpEC code used for our numerical simulations [2].

Einstein's Equations : Generalized Harmonic Formulation

Einstein's equations for general relativity are usually written through the relation between the Ricci tensor $R_{\mu\nu}$ and the stress-energy tensor $T_{\mu\nu}$,

$$R_{\mu\nu} - \frac{1}{2} g_{\mu\nu} R = 8\pi G T_{\mu\nu} \tag{1.6}$$

where $g_{\mu\nu}$ is the metric, R the trace of the Ricci tensor, and G the gravitational constant. The Ricci tensor can be expressed as a second order nonlinear differential operator acting on the metric components:

$$R_{\mu\nu} = \partial_\lambda \Gamma^\lambda_{\mu\nu} - \partial_\nu \Gamma^\lambda_{\lambda\mu} + \Gamma^\lambda_{\lambda\sigma}\Gamma^\sigma_{\mu\nu} - \Gamma^\lambda_{\nu\sigma}\Gamma^\sigma_{\lambda\mu} \tag{1.7}$$

$$\Gamma^\alpha_{\beta\gamma} = \frac{1}{2} g^{\alpha\lambda} \left(\partial_\beta g_{\gamma\lambda} + \partial_\gamma g_{\beta\lambda} - \partial_\lambda g_{\beta\gamma} \right), \tag{1.8}$$

where the $\Gamma^\alpha_{\beta\gamma}$ are the connection coefficients of the metric.

For numerical evolutions, we foliate the 4 dimensional spacetime into a set of 3 dimensional space-like hypersurfaces with coordinates x^i, parametrized by the 'time' coordinate t : the 3+1 decomposition, as for the initial data.

Note that despite this notation, there is no guarantee that curves of constant x^i are timelike: depending on the choice of foliation and coordinates x^i, they may also be null or space-like. More generally, the mathematical properties of Einstein's equations in the 3+1 decomposition depend on the choice of foliation and coordinates — and for most choices, the resulting evolution equations will not be well-posed for numerical simulations.

In our simulations, we use the generalized harmonic formulation of Einstein's equations [68]. In that formalism, the coordinates are taken to be the solutions of the wave equation

$$g_{\mu\nu} \nabla_\sigma \nabla^\sigma x^\nu = -g^{\alpha\beta} \Gamma_{\mu\alpha\beta} = H_\mu(x, g), \tag{1.9}$$

where the H_μ are algebraic functions of the coordinates and the metric. Lindblom et al. [68] showed that for any such choice of H_μ, Einstein's equations are hyperbolic: the evolution equations for the metric $g_{\mu\nu}$ are of the form

$$g^{\alpha\beta}\nabla_\alpha\nabla_\beta g_{\mu\nu} = S(g, \partial_\lambda g, x). \tag{1.10}$$

These equations are second order in time and space (where by 'time' we mean the evolution variable t). For numerical simulations, we reduce them to first order by defining the variables

$$\kappa_{\alpha\mu\nu} = \partial_\alpha g_{\mu\nu}. \tag{1.11}$$

Then the generalized harmonic equations can be written as first order differential equations for the variables $\kappa_{\alpha\mu\nu}$ and $g_{\mu\nu}$.

An additional complication comes from the constraints that these equations have to satisfy at all times. When discussing initial data, we have already seen that Einstein's equations include a set of constraints on the metric variables that have to remain negligible in numerical simulations. Other constraints come from the reduction to first order [eq.(1.11) should always be valid], and the gauge condition [eq.(1.9)]. Analytically, if the constraints are satisfied in the initial data they will remain satisfied at all times. But numerically, the constraints are never exactly satisfied: the initial data is imperfect, and numerical errors in the evolution can also create constraint-violating modes. In general some of these modes grow exponentially, rapidly destroying the accuracy of the numerical evolution.

To avoid the growth of constraint-violating modes, Pretorius [97] introduced a damping term proportional to the amplitude of these modes in the evolution equations (a modification first proposed by Gundlach et al. [47]). Following

the same method, Lindblom et al. [68] add terms proportional to the various constraints of the generalized harmonic system, in such a way that

- The constraint-violating modes are damped
- The evolution equations for the metric variables and for the constraints are hyperbolic
- The evolution equations are "linearly degenerate", a condition that guarantees that shocks will not form when evolving the metric quantities from smooth initial data.

Unfortunately, choosing damping parameters that satisfy the first condition is not easy. Acceptable values are known for perturbations around flat space. But for curved spacetimes, their determination remains in large part a trial-and-error process. Nonetheless, the generalized harmonic formulation has proven to be a reliable method for the evolution of Einstein's equations (though not the only one — the Baumgarte-Shapiro-Shibata-Nakamura formulation [11, 113] is a widely used alternative).

Numerical Simulations and Black Hole Singularities

Regardless of the formulation chosen for the evolution of Einstein's equations, another problem is likely to arise: in the presence of black holes, we have to deal with physical singularities. Two main techniques have been developed to cope with this issue. The first, called moving punctures, lets singularities move across the numerical grid: simulations using finite difference codes have shown that singular spacetimes can be evolved stably as long as the singularity does not pass through a grid point [8, 17]. This surprising result, as well as the

demonstrated ability of puncture codes to treat the accretion of matter onto the singularity [34], greatly simplifies the evolution of black holes when using finite difference methods.

The alternative is to excise from the evolution domain a region inside the apparent horizon of the black hole. Within the apparent horizon, it is possible to find closed surfaces for which the flow of information is purely ingoing: no knowledge of the fields inside the surface is needed to evolve the region outside of the surface. Thus, if we excise the region delimited by such a surface, no boundary condition is needed. The obvious advantage of this method is that the numerical grid does not contain any singularity. The disadvantage is the need to maintain at all times the property that no information flows into the numerical grid from the excision boundary: we have to use a numerical grid comoving with the black holes (so that the singularities remain within the excision regions), and control the coordinate system close to the excision surface so that it does not distort in a way that would allow information to escape from the excised region.

Fluid Evolution : Conservative Schemes

In the evolution of the fluid equations, two considerations dominate the choice of an evolution scheme: the possibility that shocks and/or discontinuities will exist within the numerical grid, and the importance of enforcing as much as possible physical conservation laws (conservation of energy, momentum, baryon number).

The relativistic equivalents to the standard conservation laws are the conser-

vation of baryon number and the Bianchi identities:

$$\nabla_\mu(\rho_0 u^\mu) = 0 \tag{1.12}$$

$$\nabla_\mu T^{\mu\nu} = 0 \tag{1.13}$$

where ρ_0 is the baryon density, u^μ is the 4-velocity of the fluid and $T^{\mu\nu}$ is the stress-energy tensor. These equations lead to 5 evolution equations, which can be written in conservative form:

$$\partial_t \boldsymbol{U} + \nabla \cdot \boldsymbol{F}(\boldsymbol{U}) = \boldsymbol{S}(\boldsymbol{U}) \tag{1.14}$$

where $\boldsymbol{U}$ are the evolved conservative variables, $\boldsymbol{F}$ are the fluxes and $\boldsymbol{S}$ the source terms, both of which are functions of the conservative variables $\boldsymbol{U}$, but do not depend on their derivatives. The advantage of this formulation is that in a finite difference scheme the fluxes can be computed at cell boundaries, and the numerical divergences computed in such a way that Gauss' theorem

$$\int \nabla \cdot \boldsymbol{F}(\boldsymbol{U}) dV = \oint \boldsymbol{F}(\boldsymbol{U}) \cdot d\boldsymbol{S} \tag{1.15}$$

is true to roundoff accuracy. With such a scheme, numerical errors will for example affect the value of the baryon density, but the total baryon mass will remain constant to much better accuracy.

The ability of these conservative schemes to respect conservation laws to high accuracy makes them a staple of hydrodynamical simulations. But in general relativity, they come with their own difficulty: the conservative variables $\boldsymbol{U}$ are different from the standard "primitive" variables $\boldsymbol{P}$ in which the equation of state of the fluid is given, and from which the source terms, fluxes and the stress-energy tensor are computed (the primitive variables in our code are the baryon density, temperature, and velocity of the fluid, as well as the electron

fraction and the magnetic field in simulations for which the influence of these variables is taken into consideration).

The conservative variables are known algebraic functions of the primitive variables, but the reverse is not true: getting the primitive variables from the conservative variables requires the use of root-finding algorithms. And, more importantly, there is no guarantee that the problem has a solution: some choices for the value of the conservative variables are not physical, and do not correspond to any real value of the primitive variables. Numerical errors can cause the evolved conservative variables to leave the physically allowed parameter space, in which case it is important to have prescriptions on how to modify them without introducing large errors in the evolution. These problems usually arise in the low-density regions, where relative numerical errors are large — modifications to the conservative variables should never be required in the high-density regions in which we expect the numerical simulation to be reliable. In practice, the numerical treatment of the low-density regions has proved to be critical to the stability and the accuracy of the code. A discussion of the methods used in our code, including an extension to magnetohydrodynamics, is given in Appendix B.

Fluid Evolution : Shocks

The equations of hydrodynamics are also known to develop shocks. This problem has been widely studied in Newtonian gravity, and the methods developed in that framework have been transposed to general relativistic simulations. In the presence of shocks, the standard methods to take numerical derivatives or interpolate functions do not converge. But shock capturing methods have been

developed, which restore first-order convergence in the neighborhood of the shock, and remain accurate to higher order (depending on the chosen method) away from the shock.

With the conservative evolution scheme that we just described, the only computation sensitive to the presence of shocks is the reconstruction of the fluxes $\boldsymbol{F}$ on cell boundaries, which requires interpolation of the fields known at cell centers. If a shock-capturing reconstruction method is used to compute $\boldsymbol{F}$, general relativistic hydrodynamical codes have been shown to properly handle shocks (see [28] for shock-tests in our numerical code).

Black Hole-Neutron Star Evolutions with SpEC

Our numerical simulations of BHNS binaries are performed using the Spectral Einstein Code (SpEC [2]). Other numerical studies of compact binaries in general relativity use finite difference methods for the evolution of Einstein's equations and that of the fluid variables. In SpEC, a different approach has been chosen: finite difference methods are still used for the fluid equations, but Einstein's equations are solved on a separate numerical grid, using pseudo-spectral methods.

For smooth functions (C^∞) spectral evolutions are known to be particularly efficient, as numerical errors decrease exponentially with resolution. This property is no longer true in the presence of shocks or sharp surfaces (as encountered in BHNS simulations at the surface of the star, or during disruption), but the evolution of Einstein's equations away from those sharp features can still be very efficiently resolved using spectral methods. Numerical grids for the evolu-

tion of compact binaries have to extend far away from the binary itself in order to properly extract the emitted gravitational wave signal, and in that extended region where no matter is present spectral methods are particularly efficient at solving Einstein's equations.

By contrast, the numerical grid on which we need to evolve the fluid equations can be of very limited size: before disruption, it only needs to cover the small region in which the neutron star is located. The main advantage of the two-grid method is thus that the fluid equations only need to be solved in a very small region, while only the numerical grid on which we solve Einstein's equations has to extend much farther. On the other hand, the two-grid method comes with an extra cost: as the two sets of equations are coupled, the communication of source terms between the two grids is necessary. We thus have a trade-off between reduced evolution cost and increased communication cost. The situation is more favorable to the two-grid method before disruption, when the finite difference grid is small, but this choice becomes less efficient at late times, when an extended tidal tail can form and require the finite difference grid to extend far away from the central black hole.

Taking full advantage of the two-grid methods thus requires the finite difference grid to follow as closely as possible the evolution of the fluid. Ideally this would be done continuously by smoothly changing the map between the coordinates of the finite difference grid and those of the spectral grid so that the finite difference grid remains as small as possible while covering all regions in which a significant amount of matter is present. In practice however, the main computational cost of grid-to-grid communication is to set up the interpolation for a given map between the two grids — doing multiple interpolations with

the map fixed is significantly faster. We thus choose to modify the map between the two grids discontinuously, interpolating the fluid variables onto a new finite difference grid whenever the current grid becomes poorly adapted to the fluid configuration. In Appendix C, we discuss in more detail how the finite difference grid is modified during BHNS evolutions.

The two-grid method with which we evolve BHNS binaries in SpEC thus consists of:

- A pseudo-spectral grid on which Einstein's equations are evolved (using the generalized harmonic formalism). This grid extends far out into the wave zone, while the region immediately around the black hole is excised from the computational domain. As spectral methods are more efficient if the variables are expended on basis functions adapted to the geometry of the problem, the numerical domain is divided into subdomains of various shapes: spheres are used around the compact objects and in the wave zone, while cubes, cylinders and wedges cover the regions in which we cannot take advantage of an approximate spherical symmetry. A typical domain decomposition to solve the initial data problem (which also uses spectral methods) is given in Fig. 2.1. The pseudo-spectral grid used for numerical evolutions is subdivided in a very similar fashion, except that we relax the requirement that the surface of the star is at the boundary between two subdomains.
- A control system meant to keep the location of the compact objects fixed on the pseudo-spectral grid. This allows us to keep the excision surface inside the apparent horizon of the black hole, and maintain approximate spherical symmetry in the regions around the original location of the com-

pact objects. For spinning black holes, the control system is also used to keep the apparent horizon mostly spherical — which helps with the efficiency of the spectral decomposition around the black hole, but also keeps the excision surface adapted to the current shape of the horizon. This last point is critical for evolutions using excision: when the excision surface becomes too distorted with respect to the horizon, it becomes increasingly likely that the evolution will no longer be well-defined in the absence of a boundary condition on that surface.

- A finite difference grid on which the fluid equations are evolved in conservative form. The variables on cell faces are computed using shock-capturing interpolation methods, while the fluxes $\boldsymbol{F}$ are computed using an approximate Riemann solver (see Duez et al. [28] for details). Interpolation on the faces can be second, third of fifth order accurate away from shocks and sharp surfaces (depending on the choice of reconstruction method), and first-order accurate otherwise. Overall, the finite difference code used is second-order convergent as long as shocks and surfaces form a region of measure 0. A low-density atmosphere is imposed outside of the star, and the evolution of low-density regions is approximated in such a way as to avoid large error growth due to numerical errors in the atmosphere.
- A framework to handle grid-to-grid communication at each timestep, as well as modify the map between the two grids when the finite difference grid becomes poorly adapted to the matter distribution
- An adaptive timestepper for the evolution in time: we usually choose the fifth-order Dormand-Prince integrator.

These methods have been used successfully to evolve BHNS systems through their last 2-3 orbits for equal mass systems [28], as well as for a range of equations of state (Chapter 3) and black hole spins (Chapter 4) for binaries with $M_{\rm BH} = 3M_{\rm NS}$. Population synthesis models currently favor the formation of BHNS binaries with more massive black holes ($M_{\rm BH} \sim 7M_{\rm NS}$). Those systems are more costly to evolve, as the maximum timestep of the evolution is determined by the grid spacing in the region surrounding the NS, which remains fixed, while the orbital timescale becomes significantly longer. Additionally, the systems studied in Chapters 3-4 all fall in the class of binaries for which the star disrupts before the plunge, and an accretion disc and tidal tail forms. For more massive black holes, it becomes possible for the star to plunge before disrupting, at least for low black hole spins — and the challenges related to the evolution of these "fast" mergers, in which the whole star is rapidly accreted onto the black hole, are different from those encountered in simulations with less massive black holes. These qualitative differences, as well as some results for BHNS binaries with $M_{\rm BH} = 7M_{\rm NS}$, are discussed in Appendix D.

CHAPTER 2

INITIAL DATA FOR BLACK HOLE–NEUTRON STAR BINARIES: A FLEXIBLE, HIGH-ACCURACY SPECTRAL METHOD

This chapter was originally published in Phys.Rev.D. in 2008 [40].

2.1 Introduction

Over the last few years, the prospect of gravitational wave detection by ground based experiments such as LIGO [67] and VIRGO [30] has encouraged rapid developments in the field of numerical relativity. Most of that effort was aimed at the evolution of compact binaries, sources of waves potentially observable by those detectors. Binary neutron stars were the first to be successfully evolved in a fully relativistic framework, and have been studied regularly over the last eight years [120, 27, 75, 53, 115, 4, 7]. Evolutions of binary black holes (BBH) followed a few years later [97, 8, 17], and continue to be an extraordinarily active area of research (see [98] and references therein).

The third type of compact binary, black hole–neutron star (BH-NS) binaries, has not been as widely studied yet. The evolution of the black hole singularity and the presence of matter combine the difficulties of evolving both binary black holes and binary neutron stars. And the system has its own specific challenges, notably the accretion of the neutron star matter onto the black hole. Such binaries are, however, worth studying not only for their interest as gravitational wave sources, but also as potential sources of gamma-ray bursts [65]. The first evolutions of such systems were announced very recently [32, 118], and such evolutions will allow more extensive study of their wave emission, merger, ac-

cretion disk formation, and so on.

The choice of a suitable initial configuration for binary evolutions has been a long-standing problem. Not only do the Einstein equations include constraints on the initial data, but also choosing a starting point that represents a realistic astrophysical situation is not trivial. Because of their computational cost, numerical simulations of compact binaries usually start just a few orbits away from merger. The two objects are close enough that the nonlinearity of the Einstein equations is important. In that regime, there is no known way of prescribing the exact state of the system. The most common assumption is that the binary has had time to settle into a quasiequilibrium state, the system being approximately time-independent in the corotating frame. Furthermore, as the viscous forces within the star are expected to be small, we do not expect much change in the spin of the star as the orbital radius decreases. For an initially nonspinning neutron star, this would lead to an irrotational velocity profile, another standard assumption. Because of gravitational wave emission, there is no exact equilibrium state, however. Accordingly, these conditions cannot be perfectly satisfied, a problem we will discuss in more detail later on.

Previous results on initial data for BH-NS evolutions include the early work of Taniguchi et al. [128] and Sopuerta et al. [123], as well as more recent initial configurations generated by Taniguchi et al. [129, 130, 131] and Grandclement [46]. Both Taniguchi and Grandclement use codes based on the LORENE package [107], and their most recent publications are similar in accuracy, computational cost, and numerical results.

In this paper, we present an alternative numerical scheme for the solution of this problem. Our code is based on the spectral elliptic solver (SPELLS) devel-

oped by the Cornell-Caltech collaboration [93], and originally used by Pfeiffer [89, 86] for the study of binary black holes (BBH) initial data. For our numerical tests, the mathematical formulation of the problem will be very similar to [131] and [46], allowing easy evaluation of the performance of our code.

Our motivation for using SPELLS is the remarkable flexibility of its multidomain spectral methods. This allows us to efficiently adapt the configuration of our numerical grid to the geometry of the system and yields high-precision results at a very reasonable computational cost. As we will see in Sec. 2.2, elliptic equations form the core of the initial data problem. Using LORENE, each of those equations has to be approximated by two Poisson equations, with coupled source terms. These two sets of equations are then solved through an iterative method. The variables are fields with an approximate spherical symmetry around one of the compact objects. However, as the source terms for the BH fields include terms centered around the NS, obtaining high-precision initial data requires a large angular resolution.

With SPELLS, by contrast we do not have to limit ourselves to spheres around the compact objects. We can instead choose among a wide variety of subdomain geometries and coordinate mappings. As the basis functions of our spectral expansion are more adapted to the geometry of the solution, a significantly smaller number of collocation points are necessary to reach a given accuracy.

In Sec. 2.4.2, we will see that the main sources of error in our initial data are the approximations introduced by the quasiequilibrium formulation. Using SPELLS, we can rapidly solve the initial data problem for a large variety of configurations to a precision allowing us to resolve these errors. We will show that they appear to be significantly lower than quoted in [131, 46]. For the clos-

est binaries, when the distortion of the star limits the precision of any spectral method, such precision is no longer possible — at least using our current numerical grid. But our error remains reasonable, reaching the level of the deviations from equilibrium mentioned in [131] for the most extreme cases.

In addition to the high-precision initial data our results provide for evolutions of BH-NS binaries, they should also make it possible to explore the limits of the quasiequilibrium formalism. Such studies are already possible for BBH binaries, as shown in [24]. On the BH horizon, the deviations from equilibrium computed in [24] are similar to our own results.

Using SPELLS, we are also able to study initial data for a spinning BH by abandoning the assumption of conformal flatness. Earlier results showed that initial configurations built using a Kerr-Schild conformal metric were significantly inferior to their conformally flat counterparts [129, 130]. Here, adapting a method developed by Lovelace for BBH [69], we show that a *modified* Kerr-Schild metric can lead to high-precision initial data. In Sec. 2.4.4 we present our results for spinning and nonspinning black holes using this modified Kerr-Schild conformal metric.

We review the formulation of the initial value problem in Sec. 2.2, and present in more detail our numerical methods in Sec. 2.3. Then, in Sec. 2.4, we discuss some tests of our code, including isolated stars and binaries that are directly comparable to previous results. Through convergence tests, we obtain a good estimate of the amplitude of constraint violations and of our error in global quantities such as the ADM (Arnowitt-Deser-Misner) energy and linear and angular momentum. Such convergence tests for fully consistent initial data in the presence of matter have, to our knowledge, only been published previ-

ously in the case of NS-NS binaries (see for example [45], specifically Figs. 4 to 7), and up to relative precisions slightly better than 10^{-5}. Our estimates will confirm that we are able to resolve deviations from quasiequilibrium except for strongly distorted stars.

Finally, adapting a method developed by Pfeiffer et al. [88] for BBH binaries, we demonstrate the possibility of reducing the eccentricity of the system, leading to initial configurations more realistic than quasiequilibrium orbits.

2.2 The initial data problem

The construction of initial data on a spatial slice containing matter typically involves two types of conditions. First, from the Einstein equations we know that any initial data will have to satisfy the Hamiltonian and momentum constraints, which we will write as a set of elliptic equations. Second, we want the resulting configuration to represent a physically reasonable situation. The mass of each object, its spin, their initial separation, and the ellipticity of the orbit are all parameters we want to control, and the initial state and physical properties of the fluid have to be carefully chosen. In this section, we will describe the different equations used to enforce those conditions, and their formulation in our numerical solver.

2.2.1 Constraints

We impose the constraints on our initial spatial slice by solving the extended conformal thin sandwich (XCTS) system, a set of 5 elliptic equations based on

the conformal thin sandwich decomposition proposed by York [139]. Here, we start from the formulation used by Pfeiffer [86] for BBH binaries, adding the matter contribution as fixed source terms in the XCTS equations.

The metric tensor is written in its 3+1 form:

$$\begin{aligned} ds^2 &= g_{\mu\nu} dx^\mu dx^\nu \\ &= -\alpha^2 dt^2 + \gamma_{ij} \left(dx^i + \beta^i dt\right) \left(dx^j + \beta^j dt\right), \end{aligned} \tag{2.1}$$

where α is the lapse, β^i the shift, and γ_{ij} the 3-metric induced on a spatial slice at constant t. The normal $\mathbf{n}$ to such a slice and the tangent to the coordinate line $\mathbf{t}$ are then related by

$$t^\mu = \alpha n^\mu + \beta^\mu. \tag{2.2}$$

We treat the matter as a perfect fluid and write the stress-energy tensor as

$$T_{\mu\nu} = (\rho + P)\, u_\mu u_\nu + P g_{\mu\nu}, \tag{2.3}$$

where ρ is the fluid energy density, P its pressure, and u_μ its 4-velocity. In practice, we will use projections of $T_{\mu\nu}$:

$$E = T^{\mu\nu} n_\mu n_\nu = (\rho + P) \frac{1}{1 - \gamma_{ij} U^i U^j} - P, \tag{2.4}$$

$$S = \gamma^{ij} \gamma_{i\mu} \gamma_{j\nu} T^{\mu\nu} = E + 3P - \rho, \tag{2.5}$$

$$J^i = -\gamma^i{}_\nu T^{\nu\tau} n_\tau = U^i \frac{1}{1 - \gamma_{ij} U^i U^j} (\rho + P), \tag{2.6}$$

where U^i is the fluid 3-velocity in the inertial frame, defined in terms of the 4-velocity $\mathbf{u}$, the normal $\mathbf{n}$ to the spatial slice studied, and the Lorentz factor γ_n as

$$\mathbf{u} = \gamma_n (\mathbf{n} + \mathbf{U}). \tag{2.7}$$

If the system is close to equilibrium, it is convenient to choose the coordinate system so that ∂_t is an approximate Killing vector. We will thus try to solve the

system in coordinates comoving with the binary. In such a coordinate system, the shift increases in magnitude with the distance from the center of rotation and diverges at spatial infinity. This is a difficulty for numerical solvers. Furthermore, to control the eccentricity of the binary, we choose to give the system an initial radial velocity of the form $\mathbf{v} = \dot{a}_0 \mathbf{r}$. This also leads to a diverging term in the shift at large distances.

We thus further decompose the shift vector as

$$\boldsymbol{\beta} = \boldsymbol{\beta}_0 + \boldsymbol{\Omega} \times \boldsymbol{r} + \dot{a}_0 \boldsymbol{r}, \tag{2.8}$$

where $\boldsymbol{\beta}_0$ is the shift in the inertial frame and $\boldsymbol{\Omega}$ the orbital angular velocity of the system. In practice, we solve for $\boldsymbol{\beta}_0$ instead of $\boldsymbol{\beta}$, as $\boldsymbol{\beta}_0$ conveniently vanishes at spatial infinity. We turn now to the extrinsic curvature, defined as

$$K_{\mu\nu} = -\frac{1}{2}\mathcal{L}_n g_{\mu\nu}, \tag{2.9}$$

where $\mathcal{L}_n$ is the Lie derivative along the normal $\boldsymbol{n}$. In the conformal thin sandwich formalism, $K_{\mu\nu}$ is divided into its trace K and trace-free part A^{ij}:

$$K^{ij} = A^{ij} + \frac{1}{3}\gamma^{ij} K. \tag{2.10}$$

The decomposition is completed by the use of conformal transformations ac-

cording to the scheme [1]:

$$\gamma_{ij} = \phi^4 \tilde{\gamma}_{ij}, \tag{2.11}$$

$$E = \phi^{-6} \tilde{E}, \tag{2.12}$$

$$S = \phi^{-6} \tilde{S}, \tag{2.13}$$

$$J^i = \phi^{-6} \tilde{J}^i, \tag{2.14}$$

$$A^{ij} = \phi^{-10} \tilde{A}^{ij}, \tag{2.15}$$

$$\alpha = \phi^6 \tilde{\alpha}. \tag{2.16}$$

Denoting the time derivative of the conformal spatial metric by $\tilde{u}_{ij} = \partial_t \tilde{g}_{ij}$, Eqs. (2.9) and (2.10) link $\tilde{A}^{ij}$ and the shift by

$$\tilde{A}^{ij} = \frac{1}{2\tilde{\alpha}} \big[(\tilde{L}\beta)^{ij} - \tilde{u}^{ij} \big], \tag{2.17}$$

where the conformal longitudinal operator $\tilde{L}$ is

$$(\tilde{L}V)^{ij} = \tilde{\nabla}^i V^j + \tilde{\nabla}^j V^i - \frac{2}{3} \tilde{\gamma}^{ij} \tilde{\nabla}_k V^k. \tag{2.18}$$

The XCTS formulation of the constraints is then a set of 5 coupled elliptic equations, with the conformal factor ϕ, the densitized lapse $\alpha\phi = \tilde{\alpha}\phi^7$, and the shift $\boldsymbol{\beta}$ (or, in practice, the inertial shift $\boldsymbol{\beta}_0$) as variables:

$$\begin{aligned} 2\tilde{\alpha} \Big\{ \tilde{\nabla}_j \big[\frac{1}{2\tilde{\alpha}} (\tilde{L}\beta)^{ij} \big] - \tilde{\nabla}_j \Big(\frac{1}{2\tilde{\alpha}} \tilde{u}^{ij} \Big) \\ - \frac{2}{3} \phi^6 \tilde{\nabla}^i K - 8\pi \phi^4 \tilde{J}^i \Big\} &= 0 \end{aligned} \tag{2.19}$$

[1] A conformal transformation of the matter quantities E, S and J^i is necessary for the Hamiltonian constraint to have a unique solution [137]. But different choices for the ratio between conformal and physical quantities are valid. Our choice of ϕ^6, which differs from [86], guarantees that volume integrals of the matter terms for fixed $\tilde{E}$, $\tilde{S}$ and $\tilde{J}^i$ are independent of the conformal factor ϕ. Indeed, the physical volume element on the spatial slice is $dV = \phi^6 \sqrt{\tilde{\gamma}} d^3x$, where $\tilde{\gamma}$ is the determinant of the conformal metric, and thus $\int E dV = \int \tilde{E} d^3x$. The full XCTS system is known to have non-unique solutions for vacuum [95, 70]; this may carry over to spacetimes with matter, but we have not observed non-uniqueness in the course of the present work.

$$\tilde{\nabla}^2\phi - \frac{1}{8}\phi\tilde{R} - \frac{1}{12}\phi^5 K^2 + \frac{1}{8}\phi^{-7}\tilde{A}_{ij}\tilde{A}^{ij} + 2\pi\phi^{-1}\tilde{E} = 0 \tag{2.20}$$

$$\tilde{\nabla}^2\left(\tilde{\alpha}\phi^7\right) - \left(\tilde{\alpha}\phi^7\right)\left[\frac{1}{8}\tilde{R} + \frac{5}{12}\phi^4 K^2 + \frac{7}{8}\phi^{-8}\tilde{A}_{ij}\tilde{A}^{ij} + 2\pi\phi^{-2}\left(\tilde{E} + 2\tilde{S}\right)\right] = -\phi^5\left(\partial_t K - \beta^k\partial_k K\right). \tag{2.21}$$

Here, $\tilde{E}$, $\tilde{S}$, and $\tilde{J}^i$ determine the matter content of the slice, and we are free to choose $\tilde{\gamma}_{ij}$, $\tilde{u}_{ij}$, K, and $\partial_t K$. Eqs. (2.19) and (2.20) are the momentum and Hamiltonian constraints, while Eq. (2.21) can be derived from the evolution equation for K^{ij}. (For more details on the XCTS system, and its derivation, see [94].)

For quasiequilibrium initial conditions, a natural choice for the free variables is to set the time derivatives to zero. The choice of $\tilde{\gamma}_{ij}$ and K is, however, less obvious. Taniguchi et al. [129, 130] showed that a conformally flat metric ($\tilde{\gamma}_{ij} = \delta_{ij}$) with maximal slicing ($K = 0$) gives good results — better than using a Kerr-Schild background at least. For the tests in this paper, we will make the same choice. In Sec. 2.4.4, however, we will show that different choices lead to acceptable initial data, and make it possible to construct spinning BHs.

2.2.2 Hydrostatic equilibrium

The initial state of the matter within the neutron star is, in general, unknown. However, we can make some reasonable approximations. First, we will require the fluid to be in a state of hydrostatic equilibrium in the comoving frame. Following the method described by Gourgoulhon et al. [45], we use the first inte-

gral of the Euler equation,

$$h\alpha\frac{\gamma}{\gamma_0} = \text{constant}, \tag{2.22}$$

where h is the fluid enthalpy and we define the Lorentz factors

$$\gamma = \gamma_n\gamma_0\left(1-\gamma_{ij}U^iU_0^j\right), \tag{2.23}$$

$$\gamma_0 = \left(1-\gamma_{ij}U_0^iU_0^j\right)^{-1/2}, \tag{2.24}$$

$$\gamma_n = \left(1-\gamma_{ij}U^iU^j\right)^{-1/2}, \tag{2.25}$$

$$U_0^i = \frac{\beta^i}{\alpha}. \tag{2.26}$$

As before, U^i is the fluid 3-velocity in the inertial frame, while U_0^i is the 3-velocity of a comoving observer. For a corotating binary, we simply have $U^i = U_0^i$, while for an irrotational configuration, there should exist a velocity potential Ψ [45] such that

$$U^i = \frac{\phi^{-4}\tilde{\gamma}^{ij}}{h\gamma_n}\partial_j\Psi. \tag{2.27}$$

The equation of continuity is then

$$\frac{\rho_0}{h}\nabla^\mu\nabla_\mu\Psi + \left(\nabla^\mu\Psi\right)\nabla_\mu\frac{\rho_0}{h} = 0, \tag{2.28}$$

where ρ_0 is the baryon density. This is an elliptic equation in Ψ, which we can rewrite more explicitly in our variables as

$$\begin{aligned}\rho_0\Bigg\{ &-\tilde{\gamma}^{ij}\partial_i\partial_j\Psi + \left[\tilde{\gamma}^{ij}\tilde{\Gamma}^k_{ij} + \tilde{\gamma}^{ik}\partial_i\left(\ln\frac{h}{\alpha\phi^2}\right)\right]\partial_k\Psi \\ &+\frac{h\beta^i\phi^4}{\alpha}\partial_i\gamma_n + hK\gamma_n\phi^4\Bigg\} = \tilde{\gamma}^{ij}\partial_i\Psi\partial_j\rho_0 - \frac{h\gamma_n\beta^i\phi^4}{\alpha}\partial_i\rho_0.\end{aligned} \tag{2.29}$$

For a star in a binary, the main contribution to the potential Ψ comes from the movement of the star along its orbit. It is thus convenient to decompose Ψ as proposed by Gourgoulhon et al. [45]:

$$\Psi = \Psi_0 + W^i x^j\delta_{ij}, \tag{2.30}$$

$$W^i = \left(\frac{\beta^i\phi^4h\gamma_n}{\alpha}\right)_{\text{CenterNS}}. \tag{2.31}$$

W^i is the inertial velocity at the center of the star, and (2.30) effectively separates the motion of the star relative to its center from its orbital motion.

Note that Eq. (2.29) is derived assuming the existence of an exact helicoidal Killing vector (for more details on the derivation of (2.29) from (2.28), read Teukolsky [133] and Shibata [116]). This is, in general, not compatible with our choice of free variables in the XCTS equations. The error we introduce is most easily seen if we consider the evolution equation for the conformal factor,

$$\partial_t \ln \phi = \frac{1}{6}\left(-\alpha K + \nabla_k \beta^k\right). \tag{2.32}$$

For Eq. (2.29) to be exact, we need $\partial_t \ln \phi = 0$, while in the XCTS equations we assume that we are free to choose $K = 0$. As nothing guarantees that $\nabla_k \beta^k = 0$ — and in fact, we can check in practice that this term does not vanish — there is a contradiction within our equations[2].

Such approximations are inevitable, as there is no exact equilibrium solution to the binary problem. In practice, we will see that our numerical scheme is sufficiently accurate that they represent our main source of error. Better choices for K, or for our other free variables, might reduce these errors. However, within the quasiequilibrium formalism, we cannot hope to make them completely disappear. In fact, even though the contradiction here was shown using the hydrostatic conditions, a quasiequilibrium formulation creates very similar problems in vacuum. (A discussion of deviations from quasiequilibrium in BBH binaries can be found in [24], and the amplitude of the time derivative of the conformal factor observed there for irrotational binaries is similar to our results for BH-NS

[2]The most natural way to get rid of that contradiction would be to use equation (2.32) as the definition of K. The quantity $\partial_t \ln \phi$ would then be a free variable, and could be set to 0. However, Pfeiffer showed [86] that such a choice makes the operator of the XCTS system noninvertible. Alternatively, inserting (2.32) in an iterative scheme driving $\partial_t \ln \phi$ to 0 seems to be unstable both for BBH [24] and BH-NS binaries.

binaries.)

Finally, to close our system of equations we need to choose an equation of state (EOS). Here, we will consider a polytropic fluid, with polytropic index $\Gamma = 2$. The pressure P, energy and baryon density ρ and ρ_0, internal energy $\epsilon\rho_0$, and enthalpy h then obey the following relations:

$$P = \kappa\rho_0^\Gamma, \tag{2.33}$$

$$h = 1 + \epsilon + \frac{P}{\rho_0}, \tag{2.34}$$

$$\rho = (1+\epsilon)\rho_0, \tag{2.35}$$

$$\epsilon\rho_0 = \frac{P}{\Gamma - 1}. \tag{2.36}$$

The method used, however, is independent of the EOS chosen — as long as, given h, we can retrieve P, ρ, and ρ_0. Indeed, we only use the EOS to reconstruct the matter quantities $\tilde{E}$, $\tilde{J}$, $\tilde{S}$, and ρ_0 needed in Eqs. (2.19), (2.20), (2.21) and (2.29) from the enthalpy h. We use a $\Gamma = 2$ polytrope as a reasonable first approximation to the nuclear equation of state, which will allow direct comparison with previous numerical results in Sec. 2.4.3.

2.2.3 Boundary Conditions

Building initial data for BH-NS binaries requires us to solve a set of elliptic equations: the constraints (2.19),(2.20), and (2.21) and, in the case of irrotational binaries, an additional equation for the potential Ψ, (2.29). We thus have to provide boundary conditions at infinity and on the BH horizon for the XCTS variables ϕ, $\alpha\phi$, and β^i, and on the surface of the NS for the potential Ψ.

At infinity (or, in practice, at $R = 10^{10}M$, the outer boundary of our compu-

tational domain), we require a flat Minkowski metric in the inertial frame:

$$\boldsymbol{\beta}_0 = 0, \tag{2.37}$$

$$\alpha\phi = 1, \tag{2.38}$$

$$\phi = 1. \tag{2.39}$$

We excise the BH interior. Assuming that the BH is in equilibrium and that the excision surface is an apparent horizon leads to the set of conditions derived by Cook and Pfeiffer [24]:

$$\tilde{s}^k \tilde{\nabla}_k \ln\phi = -\frac{1}{4}\left(\tilde{h}^{ij}\tilde{\nabla}_i \tilde{s}_j - \phi^2 J\right), \tag{2.40}$$

$$\beta_\perp = \beta^i s_i = \alpha, \tag{2.41}$$

$$\beta^i_\parallel = \beta^i - \beta_\perp s^i = \Omega^{\rm BH}_j x^c_k \epsilon^{ijk}, \tag{2.42}$$

where $s^i = \phi^{-2}\tilde{s}^i$ is the outward unit normal to the surface, h^{ij} its 2-metric, $x^c_i = x_i - c_i$ are the Cartesian coordinates relative to its center, J is a projection of the extrinsic curvature on the excision surface defined in Eq. (28) of [24], and $\Omega^{\rm BH}$ is a free parameter determining the spin of the black hole. For a corotational BH, $\Omega^{\rm BH} = 0$, while the value required to obtain a nonspinning black hole is *a priori* unknown. A good first approximation, suggested in [24], is $\Omega^{\rm BH} = \Omega$, the orbital angular velocity. This choice typically leaves the BH with a spin an order of magnitude lower than in a corotational binary. For better results, we follow the method introduced by Caudill et al. [20] for BBH: we iterate over the value of $\Omega^{\rm BH}$ to drive the BH spin to zero. This iterative method can be used to generate a BH of arbitrary spin.

The last boundary condition required on the apparent horizon is only a gauge choice. However, that choice impacts the amplitude of the deviations

from quasiequilibrium [24]. For conformally flat initial data, we will impose

$$\partial_s (\alpha\phi) = 0, \tag{2.43}$$

a choice that already gave good results for BBH binaries. We will discuss in Sec. 2.4.4 how this condition is modified when we choose a different conformal metric.

Finally, on the surface of the star, the boundary condition for Ψ can be directly inferred from (2.29): when the density tends towards 0, we are left with the equation

$$\tilde{\gamma}_{ij}\partial_i\Psi\partial_j\rho_0 = \frac{h\gamma_n\beta^i\phi^4}{\alpha}\partial_i\rho_0. \tag{2.44}$$

As $\tilde{\nabla}\rho_0$ should be along the normal to the surface of the star,(2.44) is a boundary condition on the normal derivative of Ψ.

2.2.4 Orbital Angular Velocity

In the construction of BH-NS initial data, the orbital angular velocity Ω is, in general, a free parameter. Indeed, together with the initial radial velocity, it determines the eccentricity and orbital phase of the orbit. Here, we consider binaries a few orbits before merger, where the trajectory is expected to be quasicircular. As a first approximation, we can require force balance at the center of the NS, as proposed by Taniguchi et al. [128]:

$$\nabla \ln h = 0. \tag{2.45}$$

Force balance guarantees that the binary is initially in a circular orbit. As it neglects the infall velocity, it leads to a slightly eccentric orbit, but still constitutes

a good first guess. Using Eq. (2.22), (2.45) can be written as a condition on the lapse α and the Lorentz factors γ and γ_0:

$$\nabla \ln h = \nabla \left(\ln \frac{\gamma_0}{\alpha \gamma} \right) = 0, \tag{2.46}$$

or, using the definitions (2.24) and (2.26),

$$\nabla \ln \left(\alpha^2 - \gamma_{ij} \beta^i \beta^j \right) = -2 \nabla \ln \gamma. \tag{2.47}$$

Effectively, this is a condition on the orbital angular velocity Ω, if we remember that the shift is decomposed according to (2.8). Defining $\mathbf{b}$ to be the unit-vector along the axis passing through the centers of both compact objects, we determine the angular velocity from

$$b^i \nabla_i \ln(\alpha^2 - \gamma_{ij} \beta^i \beta^j) = -2 b^i \nabla_i \ln \gamma. \tag{2.48}$$

In theory, the angular velocity appears on both sides of the equation, but we only write explicitly the left-hand side, keeping γ constant. We then check that Ω converges when (2.48) is inserted in our iterative solving procedure, described in Sec. 2.3.3.

As we only solve (2.47) along the direction $\mathbf{b}$, we still have to impose force balance along the transverse directions. To do so, we include a correction term when computing the enthalpy: if h_0 is the enthalpy computed from Eq. (2.22), we use as the effective value of h

$$h = h_0 \big[1 - (\nabla_\perp \ln h_0) \cdot (\mathbf{r} - \mathbf{c}_{\rm NS}) \big], \tag{2.49}$$

where $\nabla_\perp = \nabla - \mathbf{b}(\mathbf{b} \cdot \nabla)$ and $\mathbf{c}_{\rm NS}$ is the location of the center of the NS.

This choice drives the maximum of the enthalpy towards $\mathbf{c}_{\rm NS}$. If the equilibrium was exact, $\nabla_\perp \ln h_0$ would vanish. For our quasiequilibrium binaries, its norm is less than 10^{-6}.

An alternative method of imposing quasiequilibrium is to use the Komar mass M_K. If we have a timelike Killing vector, then M_K and $M_{\rm ADM}$, the ADM energy, should be equal. This condition is less convenient to impose during the solution, as global quantities like M_K and $M_{\rm ADM}$ cannot be reliably computed when the constraints are violated. However, we can use this equality as a test of our initial data, and verify that $(M_K - M_{\rm ADM})$ gets small as we converge.

When we start applying the procedure described by Pfeiffer et al. [88] to reduce the eccentricity of the system, the situation is slightly different. We then prescribe the value of the orbital angular velocity as well as the initial radial velocity. Eq. (2.48) is no longer useful. Instead, we adapt Eq. (2.49) so that it fixes the position of the star in all three spatial directions, replacing $\nabla_\perp$ by ∇.

Note that if ∂_t is not an exact Killing vector, the equality between Komar and ADM mass is lost. We can then use $(M_K - M_{\rm ADM})$ only as an indicator of deviations from an exact equilibrium state. For low-eccentricity binaries with a nonzero infall velocity, those deviations are significantly larger than when the angular velocity is fixed by Eq. (2.48), and the infall velocity set to zero.

2.2.5 Observing physical quantities

We have just seen that, for quasiequilibrium configurations, computing the Komar mass and the ADM energy could be useful in finding the optimal angular velocity, or to ascertain how far from equilibrium our initial data are. To ensure that our initial configuration has the desired physical properties, a few additional quantities have to be computed.

First, we want to be able to fix the mass of the compact objects. For a spinning BH, we define the irreducible mass $M_{\rm BH}^{\rm irr}$, ADM energy in isolation $M_{\rm BH}^{\rm ADM}$, and spin parameter $a_{\rm BH}$,

$$M_{\rm BH}^{\rm irr} = \sqrt{\frac{A_{\rm AH}}{16\pi}} \tag{2.50}$$

$$M_{\rm BH}^{\rm ADM} = \frac{(M_{\rm BH}^{\rm irr})^2}{\sqrt{(M_{\rm BH}^{\rm irr})^2 - a_{\rm BH}^2/4}} \tag{2.51}$$

$$a_{\rm BH} = \frac{J_{\rm BH}}{M_{\rm BH}^{\rm ADM}}, \tag{2.52}$$

where $J_{\rm BH}$ is the angular momentum of the BH. For the NS, we compute the baryon mass

$$M_{\rm NS}^b = \int_{\rm NS} \rho_0 \phi^6 \sqrt{\frac{\tilde{\gamma}}{1-\gamma_{ij}U^iU^j}} dV. \tag{2.53}$$

Here, $\tilde{\gamma}$ is the determinant of the conformal 3-metric $\tilde{\gamma}_{ij}$.

To check quasiequilibrium, we would like to know the ADM energy and the Komar mass of the system. Measuring the total angular momentum is also useful, mainly for comparisons with post-newtonian (PN) predictions or other numerical initial data. Those quantities are typically defined as integrals on S_∞, the sphere at infinity, which is not convenient for computations. Integrating by parts, we can transform these expressions into integrals on any sphere S enclosing all matter and singularities and, when needed, a volume integral on V, the region of our initial slice lying outside of S. Assuming conformal flatness, $K = 0$, and no constraint violations, this gives:

$$\begin{aligned} M_{\rm ADM} &= -\frac{1}{2\pi} \oint_{S_\infty} \delta^{ij} \partial_i \phi dS_j \\ &= -\frac{1}{2\pi} \left(\oint_S \delta^{ij} \partial_i \phi dS_j - \frac{1}{8} \int_V \phi^5 K_{ij} K^{ij} dV \right), \end{aligned} \tag{2.54}$$

$$
\begin{aligned}
M_K &= \frac{1}{4\pi} \oint_{S_\infty} \delta^{ij} \partial_i \alpha dS_j \qquad (2.55)\\
&= \frac{1}{4\pi} \Bigg[\oint_S \delta^{ij} \partial_i \alpha dS_j + \int_V \big(\alpha \phi^{-4} \delta^{ik} \delta^{jl} K_{ij} K_{kl} \\
&\quad -2\phi^{-1} \delta^{ij} \partial_i \alpha \partial_j \phi \big)\, dV \Bigg], \\
J^z_{\rm ADM} &= \frac{1}{8\pi} \oint_{S_\infty} \left(x K^{yl} - y K^{xl} \right) dS_l \qquad (2.56)\\
&= \frac{1}{8\pi} \oint_S \left(x K_{yi} - y K_{xi} \right) \delta^{il} \phi^2 dS_l .
\end{aligned}
$$

The decomposition into surface and volume integrals is not unique, but we found these expressions convenient, as the contribution of the volume terms decreases at least as $1/r$ away from the center of mass, reducing our sensitivity to small numerical errors at spatial infinity.

To make sure that the axis of rotation of the binary passes through the origin of our numerical grid, we also require that the ADM linear momentum vanishes. It is computed in a very similar way:

$$
\begin{aligned}
P^i_{\rm ADM} &= \frac{1}{8\pi} \oint_{S_\infty} K^{ij} dS_j \qquad (2.57)\\
&= \frac{1}{8\pi} \oint_S \delta^{ik} \delta^{jl} K_{kl} \phi^2 dS_j ,
\end{aligned}
$$

and our solver moves the position of the BH center so that $P_{\rm ADM}$ is driven to zero.

Finally, when discussing boundary conditions, we have seen that for irrotational binaries the correct value of the parameter $\Omega_{\rm BH}$ is unknown. We thus need to find the value that makes the BH spin vanish. To compute the spin, we use approximate Killing vectors on the apparent horizon, following a method [81] similar to the work of Cook and Whiting [25].

2.2.6 Conversion to Physical Units

In this paper, and in our numerical code, the system of units is based on the arbitrary choice of a unit mass: the ADM energy of the BH in isolation. Combined with the convention $G = c = 1$, this choice is enough to determine all units of interest for BH-NS binaries. For applications, it is necessary to express results in astrophysical units. In this section, we give the conversion formulas.

We first define the ADM mass of the neutron star $M_{\rm NS}^{\rm ADM}$ as the ADM mass of an isolated NS of baryonic mass $M_{\rm NS}^{b}$. The total ADM mass of the binary at infinite separation is then

$$M_0 = M_{\rm NS}^{\rm ADM} + M_{\rm BH}^{\rm ADM}, \tag{2.58}$$

and the mass ratio is defined as

$$\mathcal{R} = \frac{M_{\rm BH}^{\rm ADM}}{M_{\rm NS}^{\rm ADM}}. \tag{2.59}$$

Isolated neutron stars of given polytropic index are completely described by their ADM mass and their compactness

$$\mathcal{C} = \frac{M_{\rm NS}^{\rm ADM}}{R_0}, \tag{2.60}$$

where R_0 is the areal radius. Furthermore, stars of equal compactness but different masses are related by a simple scaling law. This can be seen by defining the length scale

$$R_{\rm poly} = \kappa^{\frac{1}{2(\Gamma-1)}} \tag{2.61}$$

and dimensionless quantity

$$q = \frac{P}{\rho_0}. \tag{2.62}$$

The whole problem is then invariant [10] under the transformation

$$t' = \frac{t}{R_{\rm poly}} \tag{2.63}$$

$$\mathbf{r}' = \frac{\mathbf{r}}{R_{\rm poly}} \tag{2.64}$$

$$q'(\mathbf{r}', t') = q(\mathbf{r}, t). \tag{2.65}$$

In numerical simulations, we can thus retrieve all possible configurations by keeping only $\mathcal{C}$ and $\mathcal{R}$ as free parameters, and choosing $M_{\rm BH}^{\rm ADM} = 1$. Systems with different masses but the same neutron star compactness will obey the previous scaling, with

$$R_{\rm poly} = R^*_{\rm poly} \frac{M_0 \mathcal{R}}{1+\mathcal{R}}, \tag{2.66}$$

and $R^*_{\rm poly}$ the value of $R_{\rm poly}$ when $M_{\rm BH}^{\rm ADM} = 1$.

We also define

$$\zeta(\mathcal{C}) = \frac{M^b_{\rm NS}}{M^{\rm ADM}_{\rm NS}}, \tag{2.67}$$

a quantity which, for a given compactness, can easily be obtained from the solution of the Tolman-Oppenheimer-Volkoff (TOV) equation. Then, if the baryon mass of the star is expressed in solar masses,

$$M^b_{\rm NS} = m_{\rm NS} M_\odot, \tag{2.68}$$

the BH ADM energy will be

$$M_{\rm BH}^{\rm ADM} = \frac{\mathcal{R}}{\zeta} m_{\rm NS} M_\odot. \tag{2.69}$$

It is now straightforward to retrieve the meaning of our units of distance and time. A code distance d corresponds to the physical distance

$$D = d\left(\frac{M_{\rm BH}^{\rm ADM} G}{c^2}\right) = d\left(\frac{\mathcal{R} m_{\rm NS}}{\zeta}\right) \times 1.48{\rm km}, \tag{2.70}$$

while a code time t is equal to

$$T = t\left(\frac{M_{\rm BH}^{\rm ADM} G}{c^3}\right) = t\left(\frac{\mathcal{R} m_{\rm NS}}{\zeta}\right) \times 4.94\mu{\rm s}. \tag{2.71}$$

Note, however, that for D to represent an actual physical distance, d has to be the proper separation

$$d = \int ds, \tag{2.72}$$

and not the coordinate distance on our numerical grid.

In our tests, we choose $\mathcal{R} = 1$ and $\kappa = 51.76$, which gives $\mathcal{C} = 0.149$ and $\zeta = 1.075$. The conversion is thus

$$D = d\left(\frac{m_{\rm NS}}{1.3}\right) \times 1.79{\rm km} \tag{2.73}$$

$$T = t\left(\frac{m_{\rm NS}}{1.3}\right) \times 5.97\mu{\rm s}. \tag{2.74}$$

2.3 Numerical Methods

Turn now to the numerical methods used to solve the initial data problem, and to the way the solver enforces simultaneously the various constraints on the system derived in Sec. 2.2. In this paper, we focus on the case of irrotational binaries with no initial radial velocity, even though the solver has also been used for single stars, corotational binaries, and infalling binaries. The chosen configuration is the most challenging of the four cases: the method for the other cases can be derived by omitting the irrelevant steps from what we present here.

The core of the problem is the two sets of elliptic equations, the XCTS system (2.19),(2.20), and (2.21), and the irrotational condition on the potential Ψ (2.29). To solve these equations, we use the multidomain spectral elliptic solver

(SPELLS) developed by the Cornell-Caltech collaboration, as described by Pfeiffer et al. [93]. Improvements to SPELLS since the publication of [93], mainly the introduction of cylindrical subdomains, have increased its efficiency by about a factor of 3. The performance of the solver on distorted subdomains — such as a subdomain with a boundary chosen to follow the surface of the neutron star — has also been improved, allowing us to solve the initial data problem in the presence of matter without Gibbs oscillations at the surface of the star.

SPELLS has already been used successfully to solve the XCTS system for BBH binaries [86, 88]. Here, when solving for the XCTS variables, we consider the matter terms as fixed, while in (2.29), only the potential Ψ is variable. We will detail in Sec. 2.3.3 how to combine the two groups of equations, as well as the additional conditions of force balance (2.45), vanishing ADM linear momentum and BH spin, and known BH and NS masses. But first we discuss some aspects of the solution of the elliptic equations themselves: the numerical grid, and specifics of the irrotational potential equation.

2.3.1 Domain Decomposition

Numerical Grid

The flexibility of the multidomain method used by SPELLS allows us to use relatively complex subdomain decompositions, adapting the numerical grid to the geometry of the problem at hand. It also makes it possible to solve directly the whole XCTS system as a single set of nonlinear equations, without further decomposition of the XCTS variables, and using a relatively low number of grid points.

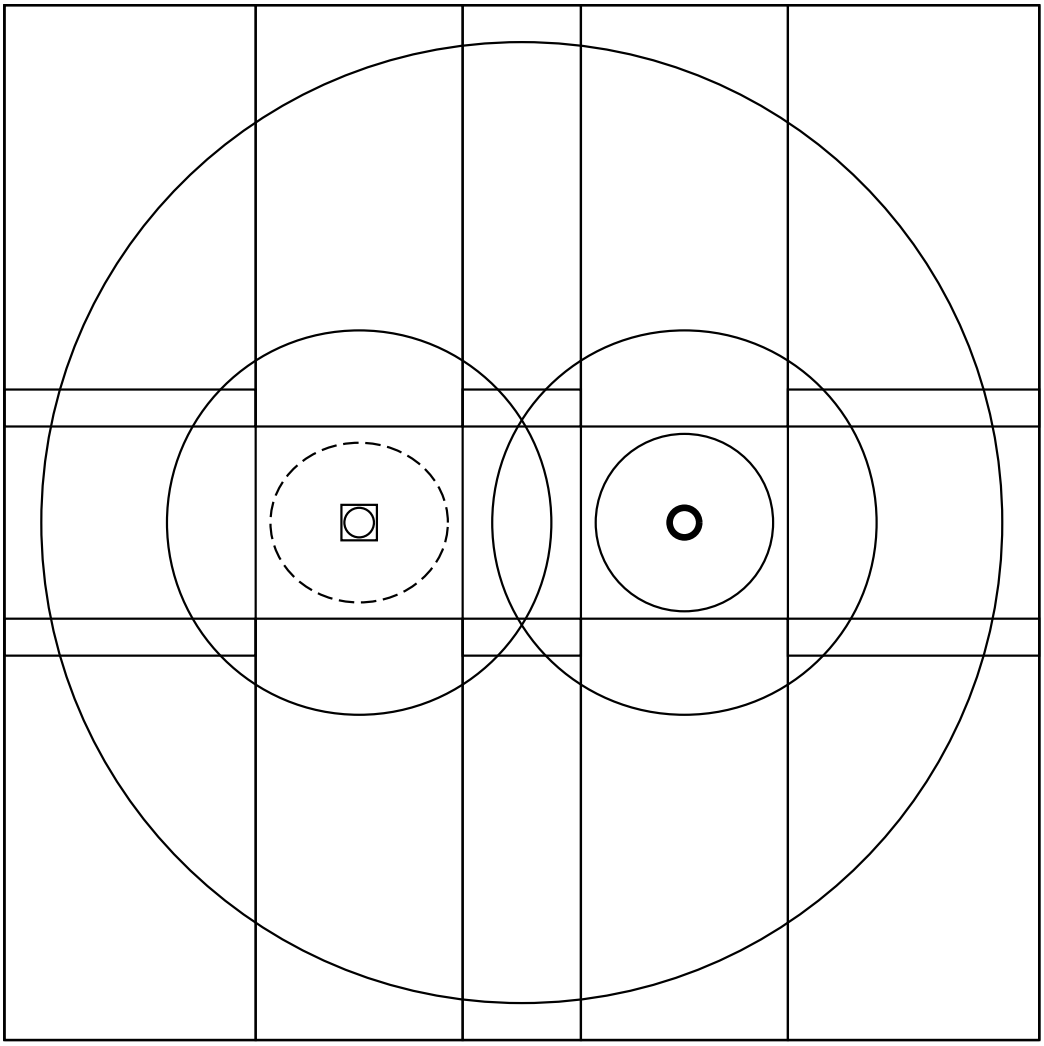

Figure 2.1: Subdomain decomposition close to the compact objects, in the equatorial plane. The apparent horizon of the BH (right) is an inner boundary of the numerical domain, while the surface of the NS (dashed line) is the boundary between the two spherical shells on the left.

For binaries in SPELLS, we build the numerical grid from 14 subdomains, as follows (see Fig. 2.1):

- Around the BH, we use two concentric spherical shells and require their innermost boundary to be an apparent horizon.
- The neighborhood of the NS is covered by an outer spherical shell with inner boundary mapped to the surface of the neutron star. This outer spherical shell touches an inner spherical shell which covers the whole neutron star, except a small region at the center. To avoid having to deal with regularity conditions at the center of a full sphere, the central region is covered by a cube overlapping the inner spherical shell.
- Three rectangular parallelepipeds cover the region surrounding the axis passing through the centers of the compact objects: one between the BH and the NS, and one on each side of the binary.
- Five cylindrical shells around the same axis cover the intermediate field region. Their innermost boundary is, for three of them, within the parallelepipeds, and for the other two, within the outer shell surrounding each compact object.
- The far-field region is covered by a spherical shell, with a $1/r$ coordinate mapping allowing us to place the outer boundary at spatial infinity (or, in practice, at $R = 10^{10}M$).

At the second highest resolution, which we use as a reference to estimate the accuracy of the solution, the cube at the center of the star has $11\times11\times11$ collocation points, the spherical shells around the compact objects have $19\times18\times36$ points, the parallelepipeds $13\times20\times20$ points, the cylinders $14\times15\times13$ (15 in the angular

direction) or 14×15×20 (the higher resolution for the subdomains closer to the compact objects), and the outer sphere 12×10×20. For comparison, the numerical grid used in [131] is built out of spherical shells with resolution 41×33×32 or 49×37×36 around the black hole, and 25×17×16 around the neutron star.

To make convergence tests, we will need a single measure of the resolution used. For a domain decomposition using subdomains with different basis functions and number of collocation points, this definition is certainly not unique. We will use

$$N^{1/3} = \left(\sum_{\text{Subdomains}} N_i \right)^{1/3}, \tag{2.75}$$

where N_i is the number of collocation points in subdomain i. For our second highest resolution, $N^{1/3} = 44.0$, while for Ref. [131] $N^{1/3} > 78.7$.

Surface Fitting

Discontinuities in variables within a subdomain spoil spectral convergence. The surface of the star is a discontinuity, so we make it the boundary between two subdomains. (Note, however, that it is possible to reach a good level of precision — of the order of the error coming from deviations from quasiequilibrium — simply by including the surface in the interior of a thin spherical shell.)

The surface of the star is approximated by an expansion in spherical harmonics,

$$R_{\text{surf}} = \sum_{lm} c_{lm} Y^{lm}(\theta, \phi), \tag{2.76}$$

where the center of the star, as defined in Eq. (2.45), is the origin of the spherical coordinates. To determine the coefficients c_{lm}, we solve the equation $h(R_{ij}, \theta_i, \phi_j) = 1$ along each collocation direction (θ_i, ϕ_j) of the numerical grid.

Then, we project onto spherical harmonics the function $R(\theta, \phi)$ defined by its values R_{ij} in each collocation direction.

To avoid Gibbs oscillations, we force the surface to be at the boundary between two spherical shells, S_0 and S_1. This is done by a coordinate transformation $R \to R'$ fixing the radius of the common boundary between S_0 and S_1 to be the given function $R_{\rm bound}(\theta, \phi)$. This function is expanded in spherical harmonics, and will be equal to $R_{\rm surf}$ when the solver converges, as explained in Sec. 2.3.3. If S_0 is defined in the original coordinates by $R_0 < R < R^*$, and S_1 by $R^* < R < R_1$, the map is, in S_0,

$$R'(\theta, \phi) = \frac{R_{\rm bound}(\theta, \phi) - R_0}{R^* - R_0}(R - R_0) + R_0, \tag{2.77}$$

while in S_1 we have

$$R'(\theta, \phi) = \frac{R_{\rm bound}(\theta, \phi) - R_1}{R^* - R_1}(R - R_1) + R_1. \tag{2.78}$$

The exact value of R^* is not important, as long as $R_0 < R^* < R_1$. However, having $R^* \sim R_{\rm bound}$ is usually convenient, as it leads to $R \sim R'$.

The validity of the Y_{lm} expansion is evaluated by observing the convergence of the coefficients c_{lm} as the resolution increases. Results for a test irrotational binary are discussed in Sec. 2.4.2.

2.3.2 Irrotational flow

Once the domain decomposition has been chosen, the XCTS equations can be solved without further modification. The irrotational equation (2.29), however, has specific problems that require further attention.

First, the coefficient of the leading order term — the Laplacian — vanishes on the surface of the star. As the equation is preconditioned by the inverse of a finite difference approximation of the flat Laplacian, convergence will become extremely poor close to the surface, where (2.29) is very different from Laplace's equation. We thus change the preconditioning operator from an approximation of $-\nabla^2 u$ to an approximation of $-\rho_0 \nabla^2 u + u$. The leading order term will then be properly represented within the star, while, when the density decreases, the operator becomes the identity and no preconditioning is done.

Another problem is related to the inconsistencies in the quasiequilibrium formulation, already discussed in Sec. 2.2.2. Indeed, we know that, for a perfect equilibrium, Eq. (2.29) will admit an infinite number of solutions (the potential is only defined up to a constant term). But, if we have instead a quasiequilibrium situation, Eq. (2.29) is not an exact representation of the continuity equation anymore. And nothing guarantees that a solution even exists. We found in practice that when using Eq. (2.29) as written, the convergence of the solver stops before we reach an acceptable precision.

Different solutions to this problem were tried, involving small modifications of Eq. (2.29). Here small means "at most of the order of the deviations from quasiequilibrium." The results presented here were obtained by replacing K in (2.29) by the value required to ensure that $\partial_t \ln \phi = 0$ using Eq. (2.32). Of course, this does not solve the inconsistency — K is still set to 0 in the XCTS equations — but it guarantees that Eq. (2.29) has a solution, allows the system to converge, and does not introduce any new source of error.

Another method, mathematically less satisfactory but leading to equivalent results, is to allow for a small correction in (2.29), for example, by adding the

mean value of the potential, $\tilde{\Psi}$, to the boundary condition (2.44) and requiring that $\tilde{\Psi}$ is driven to zero (or, in practice, the small value required to counter the error coming from our choice of K) as we converge.

2.3.3 Building quasiequilibrium binaries

As discussed previously, knowing how to solve each set of elliptic equation is only part of the problem. Here, we outline how the solver links all of the requirements together and ensures convergence towards a solution representing the desired physical situation.

At a fixed resolution, we solve according to the following algorithm:

1. Solve the XCTS system (2.19), (2.20), and (2.21), with fixed conformal matter quantities $\tilde{E}$, $\tilde{S}$ and $\tilde{J}^i$. The new value of the XCTS variables is determined by the relaxation formula $u_n = (1-\lambda)u_{n-1} + \lambda u^*$, where λ is an arbitrary parameter (we typically use 0.3) and u^* the value of u found by solving the XCTS equations. In fact, knowing that we will use a relaxation formula, we do not even solve the equations exactly at each iteration; an approximate solution is good enough, and saves a lot of computer time.
2. Impose symmetry across the equatorial plane (this step is not required, but we know that this symmetry should be respected, and enforcing it strictly accelerates convergence).
3. Evaluate the position of the surface of the star, $R^n_{\rm surf}$, and compare it to the evaluation made during the previous iteration, $R^{n-1}_{\rm surf}$. If both agree within a certain precision — we use the condition $||R^n_{\rm surf} - R^{n-1}_{\rm surf}||_2 <$

$0.1||R^n_{\rm surf} - R_{\rm bound}||_2$, where $R_{\rm bound}$ is the function used in the mapping (2.77) — modify the numerical grid by setting $R_{\rm bound} = R^n_{\rm surf}$.

4. Compute the ADM linear momentum $\mathbf{P}^n_{\rm ADM}$, and compare it to the value computed during the previous iteration, $\mathbf{P}^{n-1}_{\rm ADM}$. If $||\mathbf{P}^n_{\rm ADM} - \mathbf{P}^{n-1}_{\rm ADM}|| < 0.1 \times ||\mathbf{P}^n_{\rm ADM}||$, move the center of the BH. The change in the position of the center, $\delta\mathbf{c}$, is chosen so that, if the system was Newtonian, the total linear momentum would vanish: $\delta\mathbf{c} \times \mathbf{\Omega} = \mathbf{P}^n_{\rm ADM}$. We also change the radius of the excision surface (the inner boundary of the shells around the BH) to drive $M^{\rm ADM}_{\rm BH}$ to its desired value.

5. Solve Eq. (2.48) to find the new angular velocity.

6. Get the spin of the BH, and change the parameter $\Omega^{\rm BH}$ in the boundary condition (2.42) to drive the spin to 0 — or any other desired value, if the BH is not irrotational. The new value of $\Omega^{\rm BH}$ is chosen by linear interpolation, using the last two values of the spin.

7. Determine the constant in the Euler first integral (2.22) so that the baryon mass of the NS (2.53) is set to its target value.

8. Apply correction (2.49) to the value of the enthalpy.

9. Solve the irrotational equation (2.29) for Ψ. The new value of Ψ is determined using the same relaxation formula as for the XCTS variables.

10. If the desired precision has not been reached, go back to 1.

From this description, it is clear that the accuracy of the results depends on the convergence of the many parameters updated during the iterative procedure. We will discuss in Sec. 2.4.2 various tests verifying that they all reach an acceptable precision.

2.4 Tests and Results

As mentioned earlier, the main motivation to build a code generating BH-NS initial data using a multidomain spectral method is the possibility of rapidly reaching high levels of precision. As an example, we will focus on a sequence of irrotational, equal-mass BH-NS binaries. In Sec. 2.4.2, we show through convergence tests that, over a large range of initial separations likely to be chosen as starting points for future evolutions, we can construct initial data with enough precision to resolve deviations from quasiequilibrium. Trying to reach higher precision, even if mathematically possible, would be of little interest: the additional information would not be physically meaningful.

We then turn, in Sec. 2.4.3, to another interesting test of our results: comparing them to a similar sequence generated by Taniguchi et al. [131], and to predictions from the 3PN approximations computed by Blanchet [14], as well as Mora and Will [76]. With accurate estimates of our errors, we discuss how far deviations of the numerical results from the 3PN approximations can be trusted, and their potential interpretation.

Finally, we end this section with a discussion of two different types of initial configurations: binaries built using a modified Kerr-Schild conformal metric to construct systems with a spinning BH, and binaries with an initial radial velocity, which can be used to generate systems with low-eccentricity orbits.

Table 2.1: Domain decomposition for a single TOV star. For spherical shells, the three numbers denote the resolution in radial, polar and azimuthal directions.

	Central Cube	Inner Shells	Outer Shell
R0	7×7×7	7×6×12	8×6×12
R1	9×9×9	10×9×18	9×7×14
R2	11×11×11	13×12×24	10×8×16
R3	13×13×13	16×15×30	11×9×18

2.4.1 TOV Star

Before tackling binaries, we test our algorithm on an isolated, nonrotating NS. This effectively means that only steps 1, 2, 3, and 7 of our solution procedure are not trivial. Although the position of the surface is known analytically, for the purpose of this test we rely on the iterative surface fitting method to find it. An "exact" solution is easily computed by direct integration of the TOV equations. We compared the central density, ADM mass, Komar mass, and central lapse: all converge exponentially with resolution.

Figure 2.2 shows the difference between the exact and computed density profiles. We can see that the spectral convergence of the error holds at all radii.

For this simple case, the domain decomposition consists of just a cube covering the center of the star, two spherical shells whose common boundary matches the surface, and a third shell with an $1/r$ mapping extending to $R = 10^{10}M$. The resolutions R0 to R3 used in the test are described in Table 2.1.

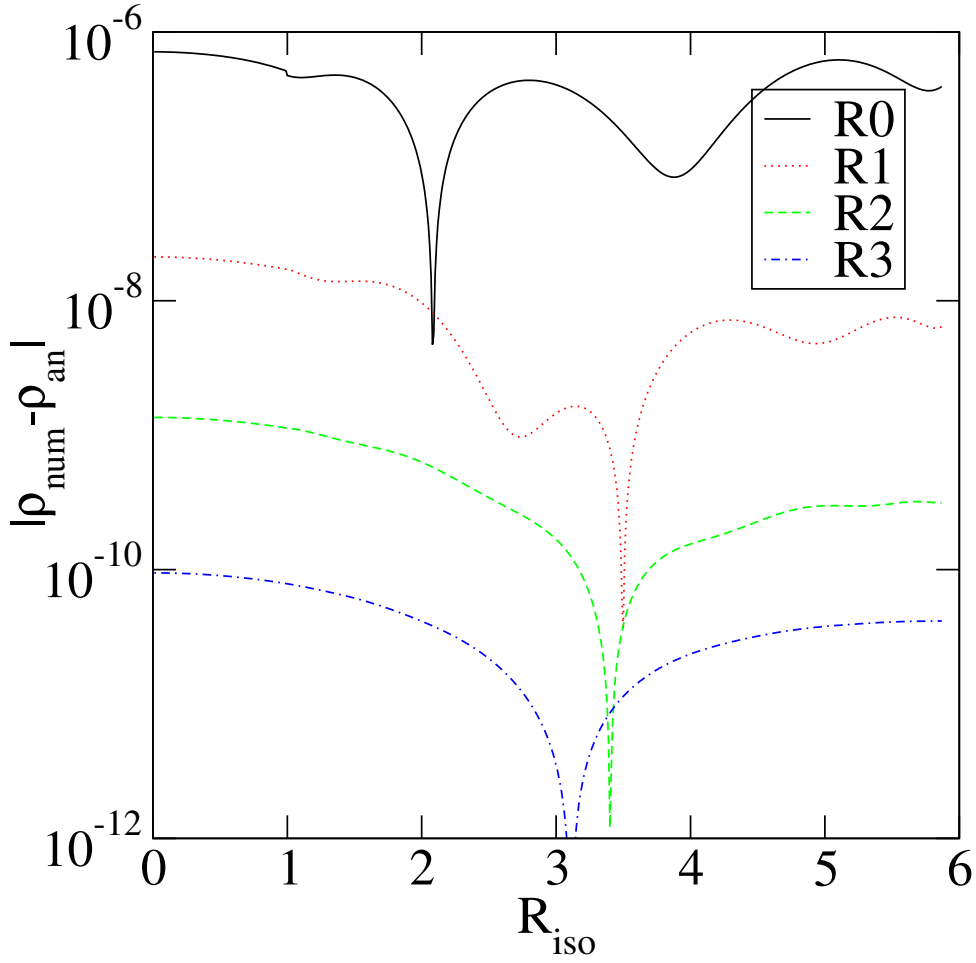

Figure 2.2: Error in the energy density for an isolated NS as a function of the isotropic radius $R_{\rm iso}$. The reference configuration is obtained by numerical integration of the TOV equations. The spikes in the error function are due to a change in the sign of $(\rho_{\rm num} - \rho_{\rm an})$

2.4.2 Irrotational binaries

To test the performance of our solver for binary systems, we use the iterative method from Sec. 2.3.3 to construct a sequence of equal-mass, irrotational binaries. The NS has an ADM mass in isolation of 1 (in code units: see Sec. 2.2.6 for a conversion in astrophysical units), and a parameter $\kappa = 51.76$, leading to a compaction similar to that used in Ref. [131], Table IV. Our results are detailed

Table 2.2: Sequence of irrotational, equal-mass BH-NS binaries. We give here the coordinate distance between the centers of the two compact objects d, the orbital angular velocity Ω, the binding energy E_b, the angular momentum J, and the difference between Komar and ADM energies. For the four closest configurations, marked by an asterisk, the numerical error estimated from the convergence of energy measurements is larger than the deviations from quasiequilibrium, approximated by $\delta M = M_K - E_{\rm ADM}$, so that δM might not be resolved. The error in E_b reaches about 5×10^{-5} at $d/M_0 = 8.406$, an order of magnitude larger than at $d/M_0 = 9.007$.

$\frac{d}{M_0}$	ΩM_0	$\frac{E_b}{M_0}$	$\frac{J}{M_0^2}$	$\frac{\lvert E_{\rm ADM} - M_K \rvert}{M_0}$
18.505	0.01169	-6.1490×10^{-3}	1.19460	7.7×10^{-7}
16.506	0.01377	-6.8103×10^{-3}	1.14241	9.5×10^{-7}
14.506	0.01653	-7.6289×10^{-3}	1.08815	1.4×10^{-6}
12.506	0.02037	-8.6634×10^{-3}	1.03177	2.0×10^{-6}
11.506	0.02288	-9.2879×10^{-3}	1.00284	2.6×10^{-6}
10.507	0.02596	-1.0002×10^{-2}	0.97353	3.4×10^{-6}
9.507	0.02981	-1.0821×10^{-2}	0.94408	4.4×10^{-6}
9.257	0.03092	-1.1043×10^{-2}	0.93675	5.0×10^{-6}
9.007	0.03211	-1.1273×10^{-2}	0.92947	5.4×10^{-6}
8.857	0.03285	-1.1416×10^{-2}	0.92514	$5.6 \times 10^{-6}*$
8.757	0.03337	-1.1509×10^{-2}	0.92225	$6.0 \times 10^{-6}*$
8.557	0.03445	-1.1706×10^{-2}	0.91656	$6.6 \times 10^{-6}*$
8.406	0.03530	-1.1853×10^{-2}	0.91237	$8.2 \times 10^{-6}*$

in Table 2.2.

We look at three different sources of error.

- The iterative procedure. To estimate that error, we study the convergence,

at fixed resolution, of all the parameters changing between iterations.

- Truncation errors. We observe the convergence of the solution with the number of collocation points by solving each configuration at four different resolutions, R0 to R3, as detailed in Table 2.3.The second highest resolution, R2, is our standard numerical grid, as defined in Sec. 2.3.1, and the highest resolution, R3, is used as an approximation of the exact solution.
- Deviations from equilibrium. We know that the quasiequilibrium formalism contains intrinsic contradictions. A useful estimate of the error thus created is the difference between the Komar and ADM energies. In the presence of an exact timelike Killing vector, both would be equal, but here the difference can be seen as an indication of how far from equilibrium we are.

All the graphs presented in this section correspond to a binary with rescaled coordinate separation $d/M_0 = 11.507$. A summary of our results for the whole sequence is in Table 2.2. Typically, the numerical error rises as the separation decreases. The difference between Komar and ADM mass can be resolved up to $d/M_0 = 9$. Numerical errors then start to increase rapidly to reach, for our closest binary, values around 5×10^{-5}. By that point, the solver does not converge at resolution R3 anymore, and we thus use R1 as our reference and R2 as an estimate of the exact solution.

Convergence of the iterative procedure

To verify the convergence at fixed resolution, observe Figs. 2.3 and 2.4. The iterative procedure converges if all parameters modified within one step converge,

Table 2.3: Domain decomposition for binary systems. A description of the different subdomains can be found in Sec. 2.3.1. The three numbers denote the resolution in radial, polar,and azimuthal directions for spherical shells, and in radial, polar, and axial directions for the cylinders. The cylinders have two different resolutions (HR/LR), the highest being used for the two subdomains directly surrounding one of the compact object. Finally, for the parallelepipeds, the first number corresponds to the resolution along the axis passing through the centers of both compact objects.

	Cube	Inn. Shells	Out. Shell	Parall.	Cyl.(HR/LR).
R0	9×9×9	13×12×24	8×6×12	9×12×12	10×9×12/9
R1	10×10×10	16×15×30	10×8×16	11×16×16	12×12×16/11
R2	11×11×11	19×18×36	12×10×20	13×20×20	14×15×20/13
R3	12×12×12	22×21×42	14×12×24	15×24×24	16×18×24/15

while the residuals from the two elliptic solves (i.e., the constraint violations and the deviations of the fluid from an irrotational configuration) vanish. In Fig. 2.3, we show the evolution of three of these parameters while iterating at our lowest resolution R0: the angular velocity Ω, derived from the Eq. (2.48), the constant in the Euler first integral (2.22), which controls the mass of the NS, and the areal mass of the BH, controlled by the radius of the excision surface. The difference between the parameter at a given step and its final value at the highest resolution is shown. We see that, even though the resolution is low, all parameters converge to a relative precision below 10^{-5}. At the reference resolution R2, the relative precision is better than 10^{-7}.

In addition to the overall convergence, Fig. 2.3 shows abrupt changes, especially in the evolution of the BH mass. These can easily be understood if we remember how the mass of the BH is fixed: the radius of the excision boundary

is modified whenever the linear ADM momentum converges. We then change our numerical grid and the location of the apparent horizon. Every time we regrid, the BH mass will at first be very close to its desired value, then reach a new equilibrium when the system adapts to its new boundary condition. The mass just before regridding — when the error is maximal — is thus the best estimate of our precision.

We also monitor the evolution of a number of quantities that should tend towards zero as the system converges: the total linear momentum (to ensure that the axis of rotation passes through the origin of our coordinate system), the BH spin (as we want irrotational binaries), the quantity $\nabla_\perp \ln h$ in Eq. (2.49), and the L2 norm of modes violating the equatorial symmetry (before we manually impose it). The last converges quickly to relative precisions of order 10^{-7}, and down to about 10^{-10} at resolution R2, while the behavior of $P_{\rm ADM}$ and $J_{\rm BH}$ is shown on Figure 2.4. As in Fig. 2.3, we plot the evolution at our lowest resolution, R0. We observe rapid convergence, with once more some oscillations due to the occasional modification of the numerical grid. At the reference resolution R2, both $P_{\rm ADM}$ and $J_{\rm BH}$ vanish to a precision better than 10^{-9}. From Figs. 2.3 and 2.4, we can thus safely consider that the iterative method detailed in Sec. 2.3.3 does indeed converge at fixed resolution.

The last parameter, $\nabla_\perp \ln h$ (not plotted), does not however completely vanish, even at our highest resolution. In fact, it converges rapidly towards a fixed, small value of order 10^{-7}. This is most likely because the equilibrium is not perfect — and, indeed, when the deviations from exact equilibrium increase, so does the final value of $\nabla_\perp \ln h$.

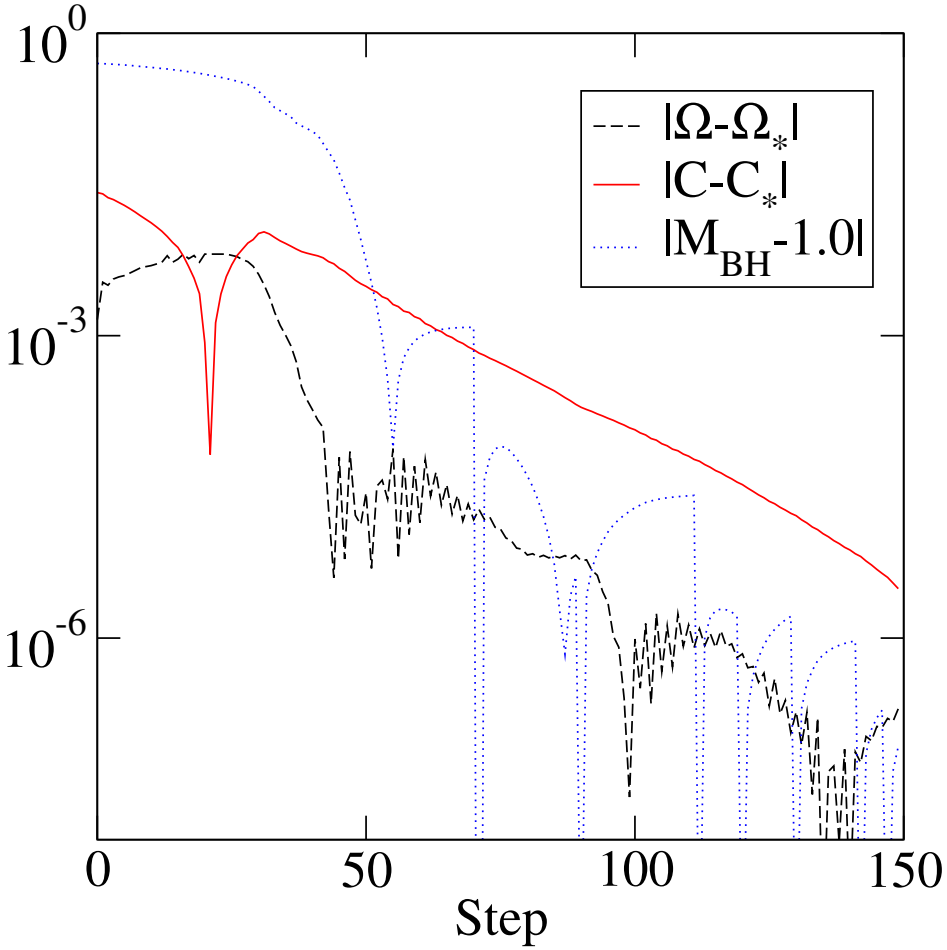

Figure 2.3: Convergence of the angular velocity, the Euler constant (which controls the mass of the star) and the mass of the BH while iterating at the lowest resolution R0 for an equal-mass binary with initial separation $d/M_0 = 11.507$. The values plotted are the differences from the final results at the highest resolution R3. One step is defined as a passage from point 1 to point 10 in the iterative procedure described in Sec. 2.3.3

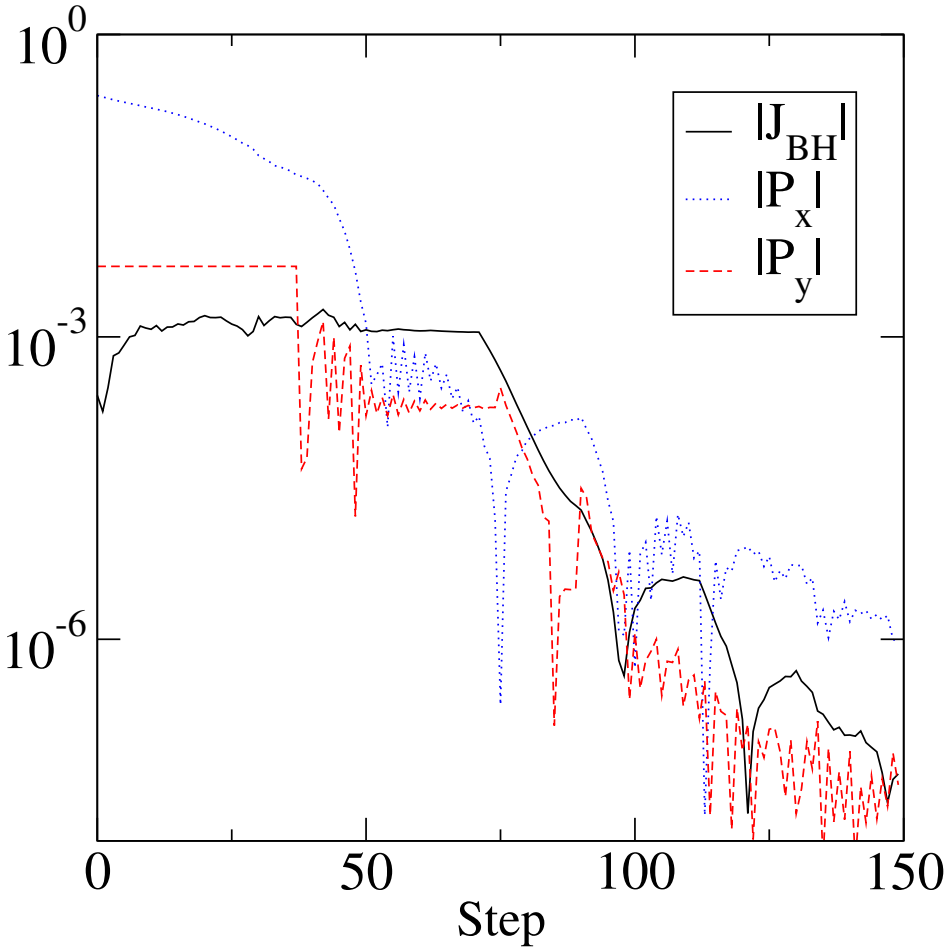

Figure 2.4: Convergence of the spin of the BH J_{BH} and the total linear momentum P_{ADM} at our lowest resolution R0 for an equal-mass binary with initial separation $d/M_0 = 11.507$.

Spectral convergence of the solution

Having established that the iterative procedure works as intended, we turn to an estimate of the precision of the initial data obtained, that is, the differences between the solutions at different resolutions. As we use a spectral representation, we expect exponential convergence of all variables. We report the convergence of the constraint violations, the performance of the surface fitting method, and the convergence of a set of measured global quantities ($M_{\rm ADM}$, $J_{\rm ADM}$, M_K,

and the position of the BH center $\mathbf{c}_{\rm BH}$).

Fig. 2.5 shows the residual of the elliptic equations corresponding to the Hamiltonian and momentum constraints. At the end of an elliptic solve at any given resolution, it should vanish at all collocation points. In order to obtain a meaningful estimate of the error, we thus evaluate the residual on the numerical grid corresponding to the next higher resolution. The exponential convergence is clearly seen, and we can deduce from Fig. 2.5 that the norm of the constraints at resolution R2 is around 10^{-8}.

The performance of the surface fitting method can be evaluated from Fig. 2.6, where we show the convergence of the surface at different resolutions. The error is estimated by the L2 norm of the difference between the coefficients of the expansion in spherical harmonics (2.76) at the current resolution and their final values at our highest resolution. The exponential convergence allows us to easily estimate the error in the position of the surface. For this configuration the position of the surface is known within better than 10^{-6} code units. For highly distorted stars however, this error becomes significant, and provides the easiest way to check during the computation whether the angular resolution is high enough or not.

Finally, in Fig. 2.7 we show the convergence of the measured ADM energy and angular momentum with resolution. For both quantities, the reference for comparison is the value measured at the highest resolution R3. We see good convergence over 2 orders of magnitude. Similar figures can be obtained for different binary separations — though as discussed earlier, our ability to solve accurately at high resolution decreases when the star becomes too distorted.

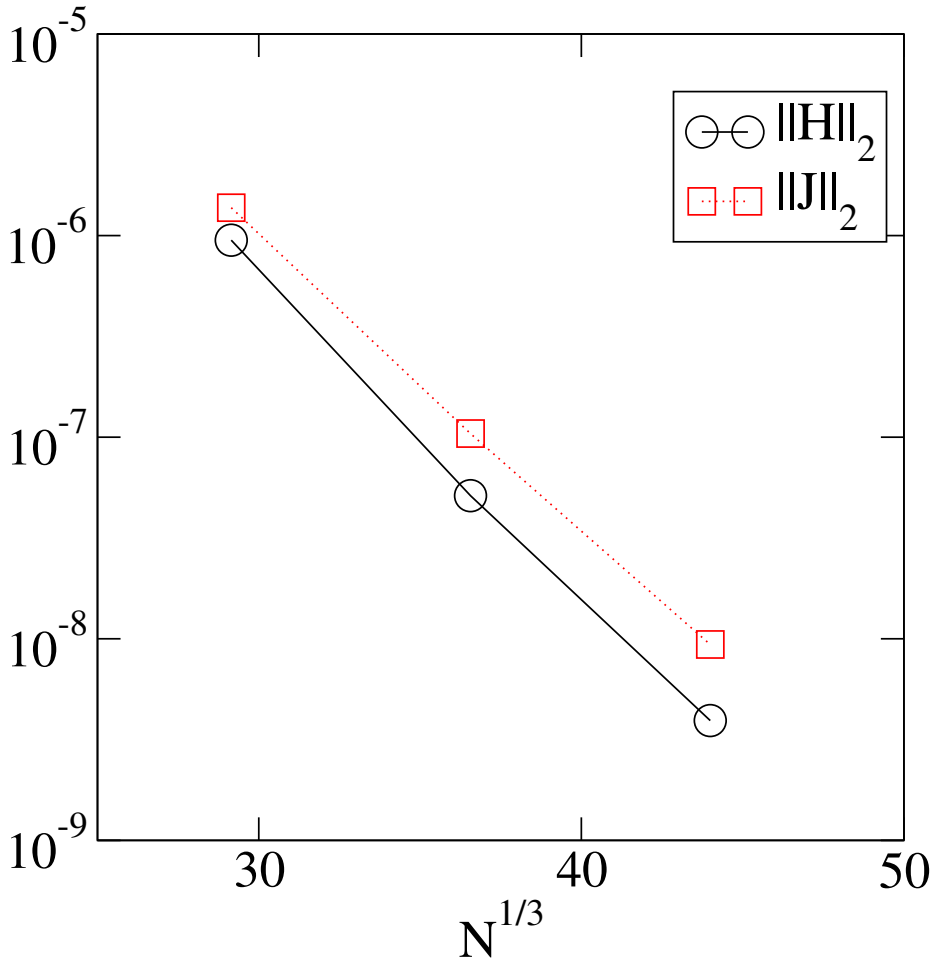

Figure 2.5: Convergence of the Hamiltonian and momentum constraints with resolution for an equal-mass binary at a separation $d/M_0 = 11.507$.

Deviations from equilibrium

Also in Fig. 2.7, we plot the convergence of the position of the BH center, which confirms that the center of the numerical grid is indeed the center of rotation of the system, and the convergence of the difference between the ADM and Komar energies δM, a measure of the deviation from quasiequilibrium. We see that this difference is resolved to a very high precision, much lower than its actual value of 2.6×10^{-6}. As the ADM energy itself is also resolved to a precision

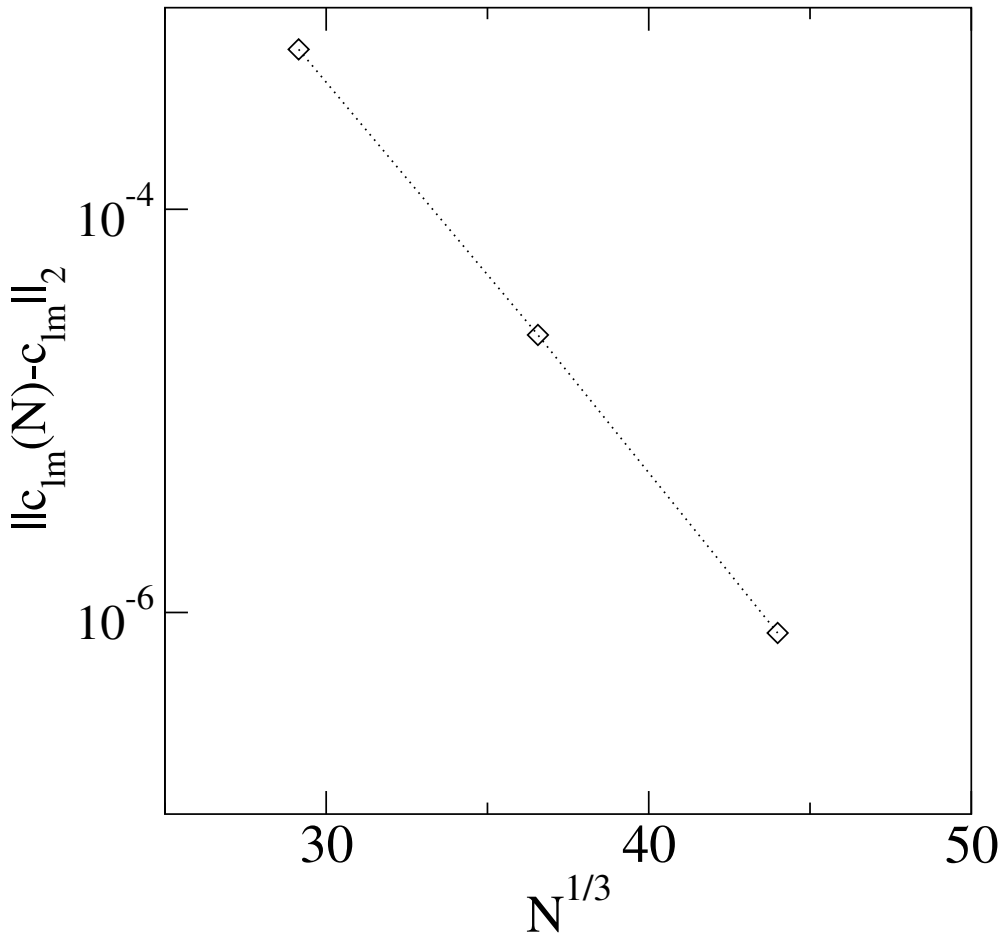

Figure 2.6: Convergence of the surface fitting method measured as the evolution of the error in the coefficients of the expansion of $R_{\rm surf}$ in spherical harmonics, computed here as the difference with our results at our highest resolution.

significantly better than 10^{-6}, we see that our main sources of imprecision are the inconsistencies inherent in the quasiequilibrium approximation.

Both the numerical errors and the deviations from quasiequilibrium increase as the separation decreases, but, as the star approaches its mass-shedding limit, the numerical error increases much more rapidly. As previously mentioned, they are roughly comparable for a rescaled coordinate separation $d/M_0 = 9$. The decrease in performance at lower separations is not, however, a serious

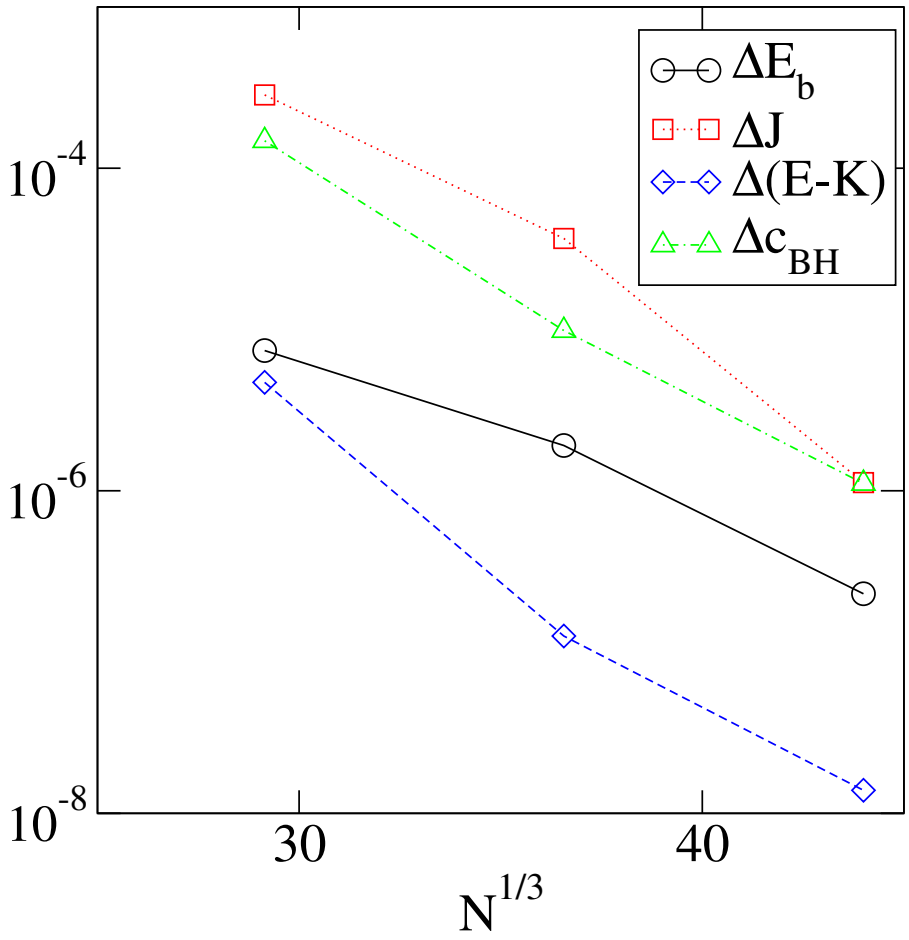

Figure 2.7: Convergence of the ADM energy, ADM angular momentum, difference between Komar and ADM energies, and position of the center of the BH with resolution for an equal-mass binary at a separation $d/M_0 = 11.507$. We plot $\Delta E_b = (E_b - E_b^*)/M_0$, $\Delta J = (J - J^*)/M_0^2$, $\Delta(E - K) = (\delta M - \delta M^*)/M_0$, and $\Delta c = ||\mathbf{c}_{\rm BH} - \mathbf{c}^*_{\rm BH})||_2$, where the reference results E_b^*, J^*, δM^* and $\mathbf{c}^*_{\rm BH}$ are those at resolution R3 ($N^{1/3} = 51.5$). The difference δM between M_K and $E_{\rm ADM}$, an indication of how close to equilibrium the system is, reaches 2.6×10^{-6} at the highest resolution. This is significantly larger than the estimated error in either $E_{\rm ADM}$, or δM shown in the figure.

problem. By that point, the radial velocity of any real binary will already be significant, and so would other deviations from the idealized quasiequilibrium state. Any evolution looking for such levels of precision should probably start from a larger separation. Results at small coordinate separations are, however, interesting for more qualitative predictions. For example, Taniguchi et al. [131] use them to determine which configurations are likely to reach the innermost stable orbit before the star gets disrupted. We will thus keep them as useful approximations, without expecting the same precision as for more widely separated objects.

2.4.3 Comparison with previous results

As a last test of our code, we compare the initial data generated using the iterative method described in Sec. 2.3.3 to 3PN approximations and previous numerical results. For these comparisons, we use the sequence of equal-mass, irrotational binaries detailed in Table 2.2. The 3PN values were obtained in the point-mass, circular orbit approximation by Blanchet [14]. We also use results from Mora and Will [76] to take into account eccentricity and finite size effects. For the numerical comparison, we use the data from Table IV of Taniguchi et al. [131]. These last results are given to 3 significant digits, the actual precision being unknown to us. Their error in the quasiequilibrium condition — our sole basis for comparison — is, at most separations, around an order of magnitude higher than what we observe in our initial data. This error is, however, small enough to allow comparisons of both numerical results with the 3PN approximations.

Table 2.4: Choice of 3PN models used as references. The eccentricity e is defined as in [76], Eq. (2.3)

	Source	Finite size	e	Orbital pos.
3PN-B	Blanchet [14]	No	0	—
3PN-M0	Mora and Will [76]	Yes	0	—
3PN-MP	Mora and Will [76]	Yes	0.01	Pericenter
3PN-MA	Mora and Will [76]	Yes	0.01	Apocenter

Four different models are compared. The first corresponds to the results of Blanchet [14], where the orbits are circular and the compact objects are modeled as point masses. The second adds finite size effects to the model. Most corrections made by Mora and Will [76] to the point-mass model vanish in the case of an irrotational binary, and only the tidal effects add a significant contribution. We compute them according to Eq. (3.6a) of their work. The last two models include some eccentricity. The exact eccentricity of our initial data is, in general, unknown. However, we can get reasonable estimates from evolutions starting at separation $d/M_0 = 12$. We will give the 3PN results for binaries with an eccentricity $e = 0.01$. At a given eccentricity, the binding energy and ADM momentum reach extrema at the pericenter and the apocenter. We thus present the 3PN results at those two points, giving an order of magnitude estimate of the influence of the eccentricity. A summary of the parameters chosen for the four models is given in Table 2.4.

In Fig. 2.8, we show results for the binding energy for various binary separations, where both numerical simulations seem to be in good agreement. For our results, the precision reached is good enough to measure deviations from the

3PN predictions neglecting eccentricity. We observe differences of order 10^{-5} for configurations where our expected precision is about an order of magnitude better. In Fig. 2.9, we show the deviations from the simplest 3PN model (3PN-B) over a large range of separations. The behavior at small separation is not resolved well enough to note anything other than the divergence of the numerical and 3PN predictions when the star reaches its disruption point. But for most of the sequence, we observe that the numerical results are clearly below the 3PN predictions, the difference between the two results decreasing at the largest separations.

It is also easy to see that tidal effects cannot explain these results. They contribute at the same order of magnitude, but tend to *increase* the energy of the system. However, Fig. 2.9 shows that our results are still compatible with the 3PN predictions if we include the influence of eccentricity. Indeed, its effects can decrease the energy of the system if we are closer to the apocenter than the pericenter — and, in fact, we know from short evolutions that this is the case for our initial data (see Table 2.7).

A similar comparison can be made using the total angular momentum $J_{\rm ADM}$, as shown in Fig. 2.10. The agreement between both numerical calculations is clearly visible, even in the regime where they deviate from the 3PN models of circular orbits. This should not be surprising, as both sets of numerical results use essentially the same formulation of the problem. As was the case for the energy, results for $J_{\rm ADM}$ can only be reconciled with the 3PN predictions if we assume a small eccentricity and an initial state closer to the apocenter than to the pericenter.

Overall, these results show that our precision is good enough to resolve de-

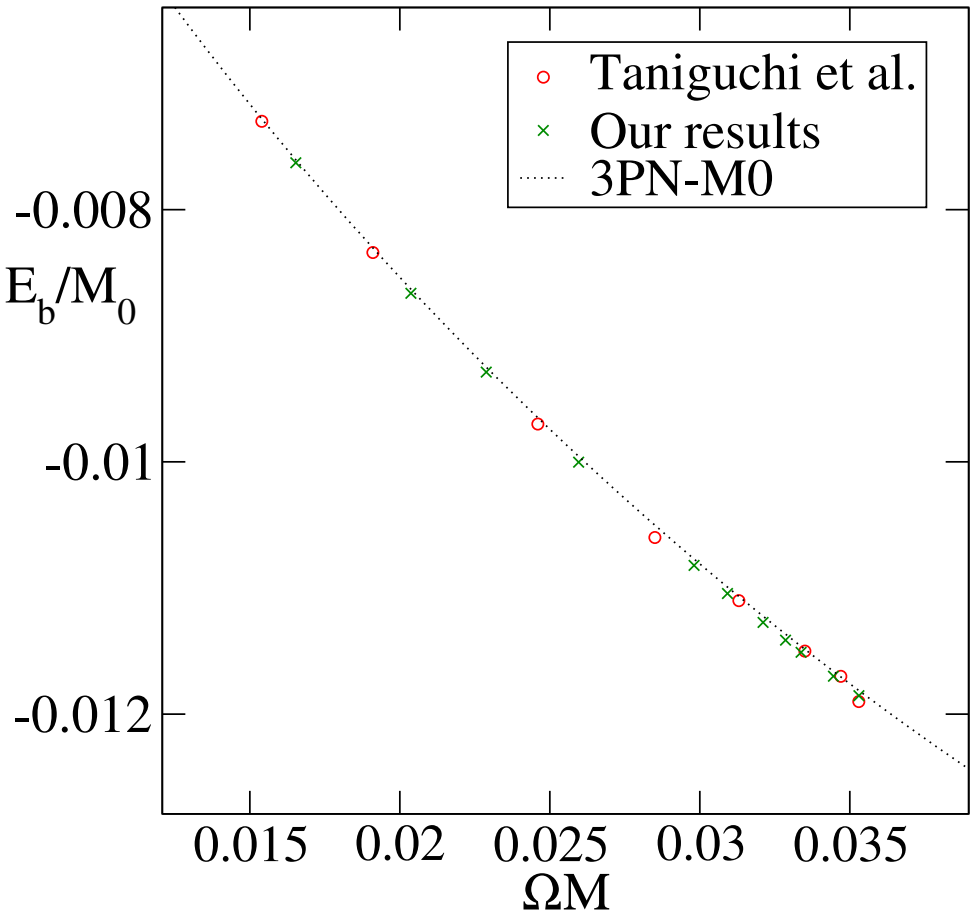

Figure 2.8: Binding energies of equal-mass binaries for initial data from our solver, from Taniguchi et al. [131], and from 3PN predictions for model 3PN-M0 (see Table 2.4).

viations from the point-mass, circular orbit 3PN predictions. We have thus the potential to study the main effects contributing to these deviations in irrotational BH-NS binaries: tidal effects in the neutron star, influence of the eccentricity of the orbit, and spurious gravitational effects due to the inconsistency of the quasiequilibrium formulation.

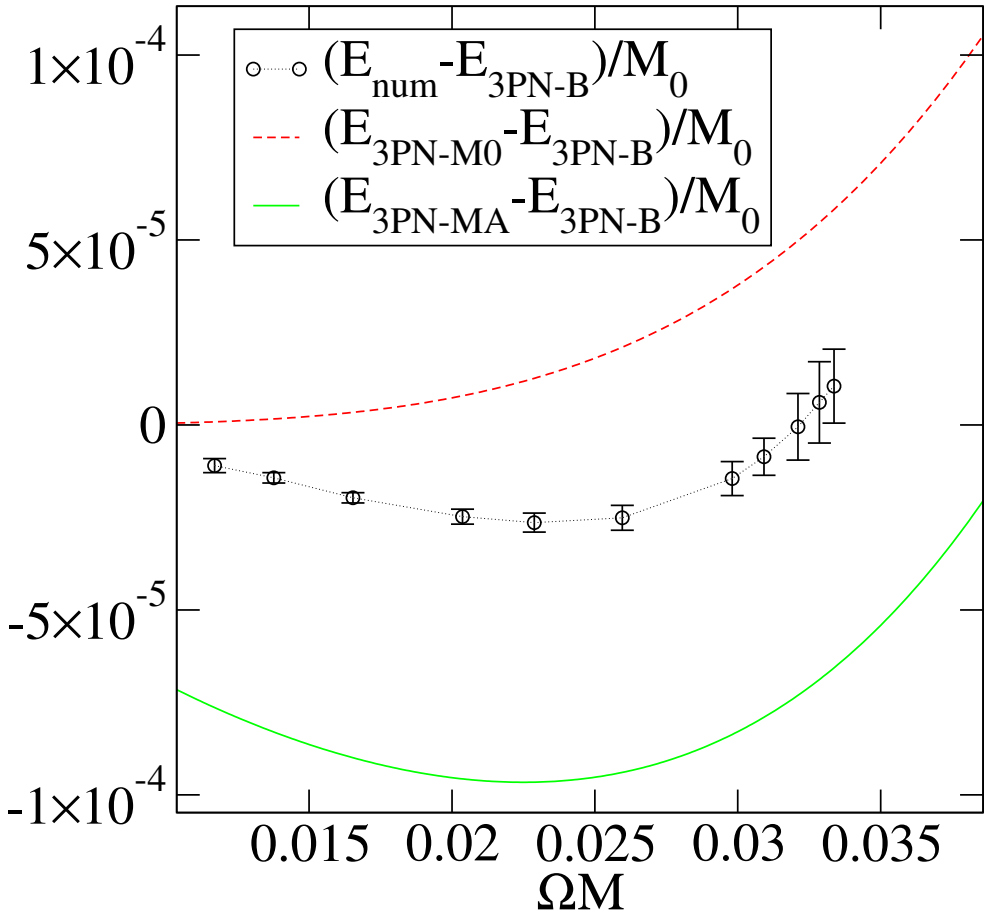

Figure 2.9: Difference between our results for the binding energy of a sequence of quasiequilibrium equal-masses binaries, and the 3PN predictions from model 3PN-B. The errors represented here come from the difference between the ADM and the Komar energies, except for the 3 closest binaries, for which the numerical error can no longer be neglected. We also represent the influence of tidal effects (from model 3PN-M0) and eccentricity (model 3PN-MA). Any binary with an eccentricity $e = 0.01$, initially closer to its apocenter than to its pericenter, should have a binding energy between the results from models 3PN-M0 and 3PN-MA. Model 3PN-MP, representing an eccentric binary at its pericenter, is not plotted here, but predicts even higher energies than model 3PN-M0.

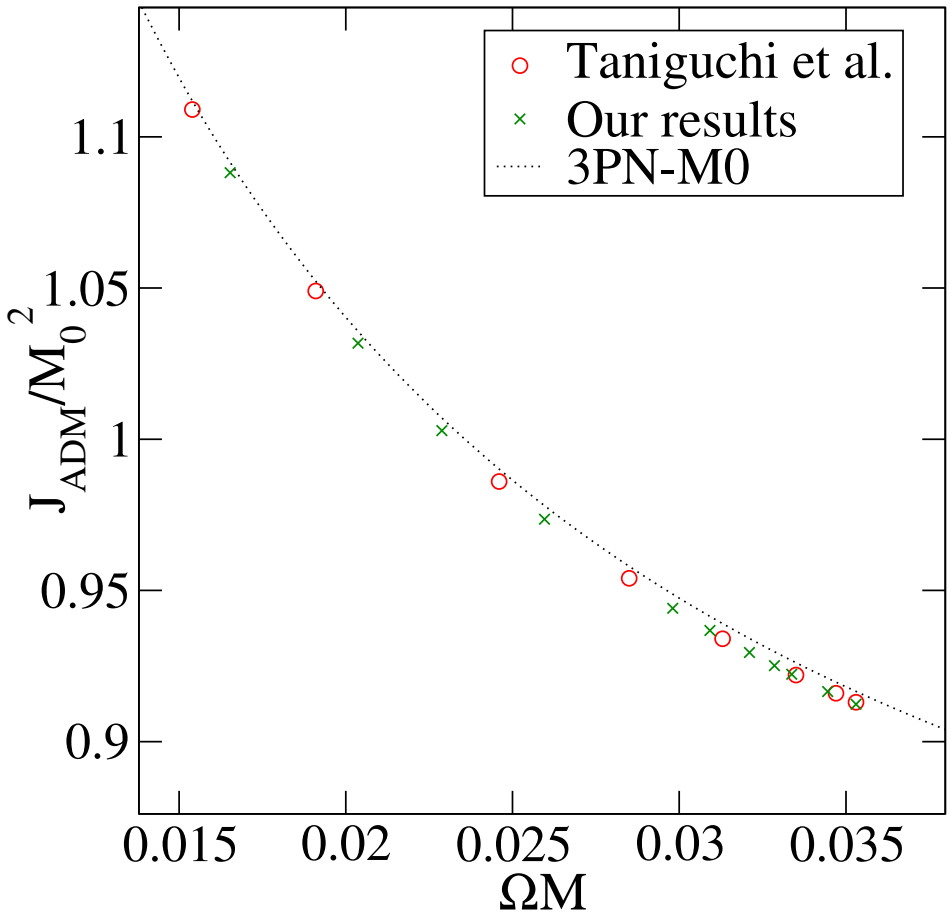

Figure 2.10: Angular momentum of equal-mass binaries for initial data generated by our solver, initial data from Taniguchi et al. [131], and 3PN predictions. We see that both numerical results are in very good agreement, even when they begin to diverge from the 3PN models of circular orbits.

2.4.4 Spinning black holes

For nonspinning or slowly spinning BHs, the conformally flat metric we have used until now performs extremely well. However, if we want to generate rotating BHs, being able to use a different conformal metric is critical. The natural choice for such BHs would be a Kerr-Schild conformal metric. Unfortunately, early results from Taniguchi et al. [129] have shown that this leads to strong

deviations from quasiequilibrium: the difference between the Komar and ADM energies in [129] is of the order of the binding energy. Here, we describe the use of a modification of the Kerr-Schild metric, already applied to BBH by Lovelace et al. [70].

We define $\gamma_{ij}^{KS}(a_{\rm BH}, \mathbf{v}_{\rm BH})$ and $K^{KS}(a_{\rm BH}, \mathbf{v}_{\rm BH})$ as the 3-metric and trace of the extrinsic curvature of a black hole with spin parameter $a_{\rm BH}$ and boost velocity $\mathbf{v}_{\rm BH}$, written in Kerr-Schild coordinates. Then, we choose the free parameters of the XCTS equations as follows:

$$\tilde{\gamma}_{ij} = \delta_{ij} + [\gamma_{ij}^{KS}(a_{\rm BH}, \mathbf{v}_{\rm BH}) - \delta_{ij}]e^{-(r_1/w)^4}, \tag{2.79}$$

$$K = K^{KS}(a_{\rm BH}, \mathbf{v}_{\rm BH})e^{-(r_1/w)^4}, \tag{2.80}$$

$$\mathbf{v}_{\rm BH} = \mathbf{\Omega} \times \mathbf{c}_{\rm BH} \tag{2.81}$$

where r_1 is the coordinate distance to the center of the BH $\mathbf{c}_{\rm BH}$, and the width w is chosen as half the coordinate distance between the two compact objects. This choice ensures that close to the BH, the metric is nearly γ_{ij}^{KS}, while away from the hole, we recover conformal flatness and maximal slicing. The introduction of the exponential damping $e^{-(r_1/w)^4}$ is the most important difference between the choices of conformal metric and extrinsic curvature in [70] and [129]. That change is indeed necessary to avoid large deviations from equilibrium.

To take advantage of the similarities between this initial configuration and a Kerr black hole, we also change the boundary condition imposed on the lapse. If the lapse of an isolated Kerr-Schild BH is $\alpha^{KS}(a_{\rm BH}, \mathbf{v}_{\rm BH})$, our boundary condition on the excision surface will be

$$\alpha = \alpha^{KS}(a_{\rm BH}, \mathbf{v}_{\rm BH})e^{-(r_1/w)^4} \tag{2.82}$$

instead of (2.43). To get as close as we can to a Kerr-Schild BH, we modify the

shape of the excision surface. The subdomain containing the apparent horizon is now a spherical shell in coordinates (r_K, θ, ϕ). The Kerr radius r_K is defined as the largest positive root of the equation $r_K^4 - r_K^2(r^2 - a^2) - (\mathbf{a} \cdot \mathbf{r})^2 = 0$, where r is the coordinate distance to the center of the BH, and $\mathbf{a} = \mathbf{J}/M_{\rm BH}^{\rm ADM}$ is the spin parameter. The excision surface is then the oblate surface $r_K = \text{constant}$, and we choose the constant so that $M_{\rm BH}^{\rm ADM} = 1$.

Once these choices have been made, no further modifications of our numerical methods are required. We test the performance of these new data sets on two types of BH-NS binaries. First, we consider configurations with a nonspinning BH, which allows direct comparison with the conformally flat initial data. Then, we move to BHs with a spin $J_{\rm BH} = 0.5(M_{\rm BH}^{\rm ADM})^2$, with the direction of $J_{\rm BH}$ opposite to the orbital angular momentum, and verify that comparable results can be obtained. Tables 2.5 and 2.6 summarize the properties of the resulting binaries. Different spins aligned with the rotation axis can be obtained using the same method. We tested our procedure up to spins of 0.9, and note that, as for BBH initial data [70], the deviations from quasiequilibrium tend to increase with the spin of the BH (the difference between Komar and ADM mass reaches about 10% of the binding energy for a spin of 0.9). The choices of the conformal metric and the lapse boundary condition seem to have a major influence on the amplitude of these deviations. Better choices will probably help reduce the deviations observed for rapidly rotating BHs.

We first note that, for equivalent resolutions, the new configurations are less precise by typically an order of magnitude. Also, as we want the width w to be large compared to the radius of the apparent horizon, we should avoid close binaries. Deviations from quasiequilibrium are also significantly larger, but not

Table 2.5: Same as Table 2.2, but for BH-NS binaries built with a modified Kerr-Schild conformal metric, as described in Sec. 2.4.4. The spin of the BH is still 0.

$\frac{d}{M_0}$	ΩM_0	$\frac{E_b}{M_0}$	$\frac{J}{M_0^2}$	$\frac{\lvert E_{\rm ADM}-M_K\rvert}{M_0}$
18.489	0.01171	-6.15×10^{-3}	1.195	8.4×10^{-6}
16.990	0.01321	-6.64×10^{-3}	1.155	8.8×10^{-6}
15.490	0.01507	-7.20×10^{-3}	1.116	9.3×10^{-6}
13.991	0.01741	-7.87×10^{-3}	1.074	1.0×10^{-5}
12.491	0.02042	-8.67×10^{-3}	1.032	1.1×10^{-5}
11.492	0.02295	-9.30×10^{-3}	1.003	1.1×10^{-5}
10.493	0.02605	-1.00×10^{-2}	0.974	1.3×10^{-5}

Table 2.6: Same as Table 2.5, but the BH now has a spin $J_{\rm BH}=-0.5$.

$\frac{d}{M_0}$	ΩM_0	$\frac{E_b}{M_0}$	$\frac{J}{M_0^2}$	$\frac{\lvert E_{\rm ADM}-M_K\rvert}{M_0}$
18.368	0.01182	-6.03×10^{-3}	1.081	2.9×10^{-5}
16.881	0.01335	-6.50×10^{-3}	1.043	3.4×10^{-5}
15.395	0.01523	-7.04×10^{-3}	1.004	4.0×10^{-5}
13.908	0.01759	-7.68×10^{-3}	0.964	4.7×10^{-5}
12.422	0.02065	-8.43×10^{-3}	0.924	5.6×10^{-5}
11.431	0.02321	-9.01×10^{-3}	0.896	6.2×10^{-5}
10.441	0.02636	-9.67×10^{-3}	0.869	6.8×10^{-5}

nearly as much as in [129], where an unmodified Kerr-Schild background was used. In [129], the difference between Komar and ADM energies was of the order of the binding energy, while here it is only about 0.15% of that value. Direct comparison between our results for a flat conformal metric and Table 2.5 also shows that both sets of initial configurations are in agreement.

As long as the BH is not rotating, the new conformal metric does not lead to any noticeable advantage over the conformally flat background — though the initial burst of gravitational radiation might end up being smaller. For rotating BHs, however, a conformally flat metric is no longer appropriate, while a modified Kerr-Schild metric allows us to solve the initial data problem. Deviations from quasiequilibrium will increase once more, but for a BH spin $J_{\rm BH} = -0.5$, we can still solve for the binding energy within a fraction of a percent. The norm of the constraints is also below 5×10^{-6} for our closest binaries, making these initial configurations perfectly suitable for future evolutions.

Our ability to reach high accuracy at a relatively low resolution is particularly important for the construction of these spinning configurations. Indeed, the slower convergence rate makes it significantly harder to obtain useful initial data. Moreover, as the geometry around each compact object become less and less spherical, being able to easily adapt our numerical grid becomes even more necessary. These first results show that the construction of spinning BHs is perfectly possible without much modification of our basic formalism — and improvements in the choice of the conformal metric and/or the excision boundary conditions might further improve the quality of such initial configurations.

Table 2.7: Orbital parameters of three irrotational BH-NS binaries, after 0, 1, and 2 steps of the iterative procedure designed to reduce the eccentricity of their orbits. The initial radial velocity of an observer comoving with the NS is $v_r = \dot{a}_0 d_0/2$, the eccentricity is measured from the parameters of the fit (2.83) according to $e = B/\omega d_0$, and the orbital phase ϕ is 0 at pericenter and π at apocenter.

	v_r	ΩM_0	e	ϕ/π	$\frac{\lvert E_{\rm ADM}-M_K\rvert}{M_0}$
Step0	0	0.02157	1.0×10^{-2}	0.68	2.3×10^{-6}
Step1	$-9.36(-4)$	0.02161	4.4×10^{-3}	1.18	2.8×10^{-4}
Step2	$-7.20(-4)$	0.02165	6.5×10^{-4}	1.59	2.9×10^{-4}

2.4.5 Low-eccentricity binaries

The initial configurations discussed in this paper correspond to binaries only a few orbits away from merger. Such systems are expected to have nearly circular orbits as, because of gravitational wave emission, the eccentricity decreases as a power law of the distance between the objects [85]. The influence of the eccentricity on observable quantities such as the gravitational waveform can be significant. For instance, it is one of the dominant effects limiting the comparison between high-accuracy BBH evolutions and post-Newtonian expansions presented in [16], even though the initial eccentricity of their binary is lower than 6×10^{-5}.

Evolutions of BH-NS systems are far from being as precise. But the force balance condition we used until now leaves the binaries with eccentricities of order 0.01 — enough to be noticeable in evolutions. We thus want to decrease the eccentricity of the initial data so that its influence on the orbit is at most of the order of the precision of the evolution code.

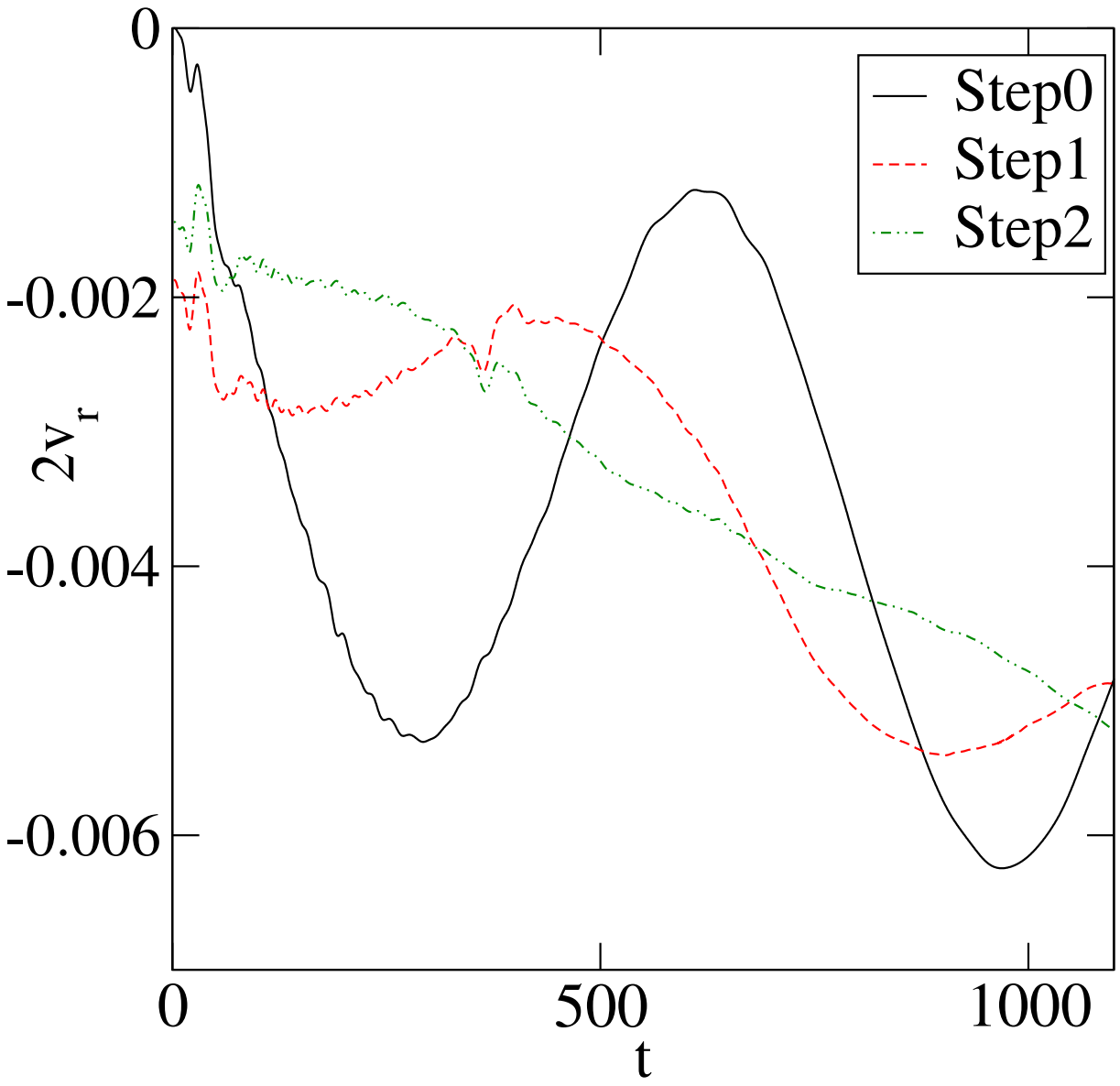

Figure 2.11: Evolution of equal-mass binaries after 0, 1 and 2 steps of our iterative method reducing the eccentricity. We plot the time derivative of the coordinate separation between the BH and the NS, $2v_r = \dot{d}$.

Here, we show that the iterative method already used to reduce the eccentricity of BBH [88] can be applied successfully to BH-NS binaries. For all evolutions described in this section, we used the mixed finite difference-spectral code described in Duez et al. [29].

The eccentricity and orbital phase of our binaries are determined by the choice of orbital angular velocity Ω and infall velocity $\dot{a}_0\mathbf{r}$. Until now, we have been determining Ω through Eq. (2.45), choosing $\dot{a}_0 = 0$. Now, we will use such configurations as a first approximation to the low-eccentricity solution, and try to determine from its evolution better values of Ω and $\dot{a}_0$.

To do so, we record the coordinate separation between the center of the compact objects, d, and fit its time derivative by the formula

$$\dot{d} = A_0 + A_1 t + B \sin(\omega t + \phi), \tag{2.83}$$

where the parameters A_0, A_1, B, ω, and ϕ are all determined by the fit. For a Keplerian orbit, we would have $A_0 = A_1 = 0$, and an eccentricity $e = B/\omega d_0$, where $d_0 = d(t = 0)$. We use this definition of e as an approximation of the eccentricity of the system. As in [88], we then choose the corrections to Ω and $\dot{a}_0$ so that a Keplerian orbit with the same parameters d, ω, ϕ, and B would become circular:

$$\delta\dot{a}_0 = -\frac{B\sin\phi}{d_0}, \tag{2.84}$$

$$\delta\Omega = -\frac{B\omega\cos\phi}{2d_0\Omega_0}. \tag{2.85}$$

For the fit (2.83) to be accurate, we need to evolve the binaries for at least one and a half orbits. Furthermore, as the initial spurious burst of gravitational radiation in the data disturbs the early motion of the binary, we also exclude points at $t < 100M$ from the fit.

As a first example, we consider a binary at initial coordinate separation $d/M_0 = 12.0$, and evolve it using the fully relativistic numerical code described in [29]. From this evolution, we determine that the eccentricity of the initial data constructed by requiring force balance (2.45) and $\dot{a}_0 \mathbf{r} = 0$ is of order $e = 0.01$. We then go twice through the iterative method we just described. The orbital parameters of the three binaries we evolved are listed in Table 2.7 while in Fig. 2.11, we show the time derivative of the coordinate separation, $\dot{d}$. Two iterations reduce the eccentricity by about an order of magnitude. Decreasing the eccentricity further would demand evolutions at a higher resolution, increasing the computational cost, but does not in principle involve any new difficulties. We also find that the difference between ADM energy and Komar mass increases by about 2 orders of magnitude during eccentricity removal (see Table 2.7).

2.5 Discussion

In this paper, we presented a new method for the construction of initial data for BH-NS binaries, based on the multidomain spectral elliptic solver SPELLS [93]. The flexibility of the multidomain spectral methods allows the use of a numerical grid adapted to the geometry of the system. We showed that this allows us to build high-accuracy initial data while keeping the number of grid points relatively low.

Using the extended conformal thin sandwich formalism and fixing the initial state of the system through quasiequilibrium conditions, we obtained initial data whose precision is limited only by the small deviations from an exact equilibrium. As an example, we showed convergence tests for a sequence of

equal-mass, irrotational BH-NS binaries, verifying the exponential convergence of our solver. Corotational and unequal-mass systems lead to similar results.

We also showed that with such accuracy we can resolve deviations from the point mass, circular orbit 3PN predictions, and observe the influence of tidal distortion and eccentricity.

Abandoning the assumption of conformal flatness, we generalized the method to construct binaries with a spinning black hole. Previously, initial data with a Kerr-Schild conformal metric was shown to be significantly inferior to conformally flat configurations [130]. Here, we showed that using a Kerr-Schild metric cut off at large distances from the BH allows reasonable precision to be reached— as in the case of BBH [69]. We verified that with such a conformal metric we could construct a binary whose BH has a spin $J_{\rm BH} = -0.5$ perpendicular to the orbital plane.

Finally, we adapted a method designed for BBH [88], and demonstrated our ability to significantly decrease the eccentricity of the binary initial data.

CHAPTER 3

EQUATION OF STATE EFFECTS IN BLACK HOLE-NEUTRON STAR MERGERS

This chapter was originally published in Classical and Quantum Gravity [26], and written in close collaboration with Matthew Duez. Francois Foucart was mainly responsible for the simulation and analysis of BHNS binaries with polytropic equations of state, as well as a large part of the code improvements described in Section 3.2.1. Simulations of BHNS binaries using the Shen equation of state, as well as the code modifications required for those simulations to be possible, were mainly the work of Matthew Duez.

3.1 Introduction

Black hole-neutron star (BHNS) inspirals and mergers are excellent gravitational wave sources. Also, a BHNS merger may leave a hot, massive accretion disk around the black hole (BH), a promising setup for producing a short-duration gamma-ray burst (GRB). However, reliable predictions regarding the waveform and post-merger state of any specific BHNS merger can only be obtained from fully relativistic numerical simulations.

The merger is strongly affected by the NS equation of state (EoS), i.e., the dependence of the fluid pressure on density, temperature, and composition. The EoS determines the radius $R_{\rm NS}$ of a NS of given mass $M_{\rm NS}$, and thus it also fixes the star's compaction $\mathcal{C} = M_{\rm NS}/R_{\rm NS}$. A larger star will be tidally disrupted by the BH's gravity at a larger distance. Also, because the EoS affects $dR_{\rm NS}/dM_{\rm NS}$, it can influence the character of the mass transfer from the star to the BH, with

mass transfer tending to be more stable for stiffer EoS. Differences in the stability of mass transfer could conceivably result in qualitative differences in the merger dynamics. The NS EoS at low densities is known, but at high densities it is not well constrained by theory, experiment, or observation. It must, therefore, be treated as another parameter in BHNS simulations. If the EoS significantly affects the waveform, then comparison of numerically generated waves with observations may someday provide information about the EoS.

Attempts have been made to estimate the effects of NS EoS in the context of Newtonian BHNS simulations. Newtonian simulations have considered polytropic [63, 64, 61, 62], Lattimer-Swesty [59, 52] and Shen [111, 112, 104] EoS. These simulations showed large qualitative differences for different EoS assumptions. For Lattimer-Swesty nuclear matter, the NS disrupts in one mass transfer event, and a large post-merger disk is created. For Shen nuclear matter, a NS core can survive multiple mass transfer events, and the postmerger disk is much smaller. There are indications that the differences are not quite so dramatic when general relativity (GR) is accounted for. The use of GR-mimicking potentials [84, 5] tends to eliminate episodic mass transfer [103, 105]. Simulations of large mass-ratio cases using the conformally flat approximation of GR also found mass transfer to be less stable (and, therefore, surviving cores to be less likely) than in Newtonian evolutions [36]. These conformally-flat-GR studies only considered fairly soft EoS, however.

Published BHNS simulations in full GR have thus-far restricted themselves to modeling NS as $\Gamma = 2$ polytropes [121, 122, 31, 119, 28, 33, 117]. These have investigated the effects of varying one important EoS-related variable, namely $R_{\rm NS}$ [31, 119, 117]. Varying $R_{\rm NS}$ between 12 and 15km for a fixed $M_{\rm BH}$ and $M_{\rm NS}$,

they find, unsurprisingly, that larger stars disrupt farther from the BH, leading to larger disks but weaker merger waveforms. These simulations could not address the importance of the stiffness of the EoS in affecting the mass transfer.

Another important question is whether BHNS mergers eject significant amounts of NS matter (perhaps including r-process elements [58, 127]) into the interstellar medium. Newtonian [52], pseudo-Newtonian [103, 105], and conformal-GR [36] simulations predict large ejecta masses, but this has not yet been seen in full GR. However, microphysics in the tidal tail could have important effects. As the density decreases, nucleons recombine into nuclei, heating the gas through the released binding energy. The resulting increase in thermal pressure can strongly affect the tail [104], perhaps helping to unbind material. Material may also be ejected in a neutrino-driven or magnetic field-driven disk wind, effects which are also not captured in current GR simulations.

In this paper, we study the imprint of the NS EoS on the merger dynamics and the resulting waveform and disk. Our investigation is based on simulations of BHNS mergers in full GR carried out with the Cornell-Caltech code SpEC. In a previous paper [28], we demonstrated this code's ability to evolve BHNS inspirals and mergers. Since then, we have made a number of improvements which reduce the constraint violation during merger by an order of magnitude. For this study, we fix the binary mass ratio to 3:1 and the initial BH spin to be $\left|\vec{S}_{\rm BH}\right|/{M_{\rm BH}}^2 = 0.5$ (aligned with the orbital angular momentum), and we vary the assumed EoS. We evolve $n = 1$ polytropes using a $\Gamma = 2$ Gamma-law and $n = 4/7$ polytropes using $\Gamma = 2.75$. We also perform simulations using the tabulated, nuclear-theory based Shen EoS [111, 112]. We vary the EoS and the compaction separately to isolate the effect of each.

All our mergers are qualitatively similar: we find no cases of episodic mass transfer, no instances of significant unbounded outflow, and no cases in which the disruption fails to produce a significant disk. There are, however, some quantitative EoS signatures in the waveform above 1kHz and in the disk. We confirm earlier findings regarding the effects of NS compaction. For a given compaction, stiffer EoS produce larger tidal tails. In every case, the post-merger disk has a mass of 0.05-0.1$M_\odot$ and an average temperature of order an MeV.

In Section 2, we describe important improvements to our code from [28]. In Section 3, we describe the models we evolve. In Section 4, we present the results of our evolutions. In Section 5, we summarize our findings and consider what remains to be done to accurately sample all of the interesting regions of BHNS parameter space.

3.2 Numerical methods

3.2.1 Code improvements

The main improvements to our code from [28] come from a better allocation of grid points when solving the fluid equations, modified gauge conditions and atmosphere prescriptions.

Our simulations use two grids [28]: a pseudospectral grid on which Einstein's equations are solved, and a finite difference (FD) for the relativistic fluid equations. For efficient evolutions, the FD grid should adapt to the configuration of the fluid. One approach is to use adaptive mesh refinement, as in some

FD-based GR codes [109, 3, 136]. We choose instead to modify the mapping between the two grids as soon as a significant flow of matter is approaching the boundary of the FD grid. A translation and rescaling of the coordinates allows the grid to move, grow and shrink so as to follow the fluid evolution. To increase the resolution in the neighborhood of the black hole, we use a map of the form

$$\begin{aligned} r' &= r \quad (r < R_0) \\ r' &= ar^3 + br^2 + cr + d \quad (R_0 < r < R_1) \\ r' &= \alpha r \quad (r > R_1), \end{aligned} \tag{3.1}$$

where r is the coordinate distance to the center of the hole, R_0 and R_1 are predetermined length scales, the parameters (a, b, c, d) are chosen so that the map is C^1, and α varies with the size of the FD grid. (Once the grid becomes large, we maintain a constant resolution in the region $r < R_0$ and vary α to fix the location of the outer boundaries.)

The gauge in the generalized harmonic formulation is set by specifying the functions $H_a = g^{bc}\Gamma_{abc}$. During the inspiral, we fix H_a in the moving frame, as in our earlier paper [28]. During the merger, we continue to hold H_a fixed in the moving frame in the region near the black hole, and we exponentially damp H_a to zero in the region far from the hole. We find that fixing H_a near the excision zone significantly reduces constraint violations.

As Faber *et al.* [35] have pointed out, the inversion from conservative to primitive hydrodynamic variables is only possible if $S \equiv g^{ij}S_iS_j < S_{\rm max} \equiv \tau(\tau + 2D)$. After each evolution step, we impose the condition $S \leq S_{\rm max}^{\rm code} = fS_{\rm max}$. We find $0.99 < f < 1$ is necessary to avoid causing large effects on the evolution of the tidal tail. Once the values are "fixed" in this way, primitive variables can

be reconstructed, but they may still be unreasonable in very low density "atmosphere" regions. Therefore, we next apply limits on the conformal 3-velocity u_i and the temperature T. We emphasize that these limits are only applied to low density regions, several orders of magnitude sparser than the star, the disk, or the tidal tail. We have checked that our evolutions are insensitive to variations in these atmosphere ceilings.

With our standard resolution, the normalized constraint violations peak at $\approx 1\%$ during mergers. Convergence tests on the $\Gamma = 2.75$ case indicate errors in our reported disk masses of $< 10\%$.

3.2.2 Use of tabulated $\rho/T/Y_e$-dependent EoS

For composition-dependent EoS, there is a new independent variable to be evolved: the electron fraction Y_e. Its evolution equation in conservative form is

$$\partial_t(DY_e) + \partial_i(DY_e v^i) = S_\nu \ , \tag{3.2}$$

where S_ν is the source term set by weak interactions and neutrino radiation, effects not modeled in our code. Here, we consider two limiting cases. First, we assume the weak interaction timescales are much longer than the merger timescale. Then we may set $S_\nu = 0$ and evolve a continuity equation for DY_e. As another limit, we assume that weak interactions act sufficiently quickly to instantaneously enforce β-equilibrium. Thus, for a given density ρ and T, Y_e is set to the value that makes $\mu_n = \mu_p + \mu_e$, where μ_x is the chemical potential of particle x. (We assume μ_ν is negligible.) This effectively removes Y_e as a dynamical variable. In neither case do we account for energy loss by neutrino

emission. Given that the cooling timescale of the disk will probably not be less than about 0.1 second (see, e.g. [66]), and our simulations last $\sim$10ms, ignoring neutrino cooling is reasonable.

We use a tabulated EoS with baryon component taken from Shen *et al* [111, 112] and with lepton and photon contributions added. (See [78] for details.) For low T ($\leq$ 10MeV), the NS EoS is fairly soft ($\Gamma \approx 4/3$) at low ρ ($\lesssim 10^{13}\mathrm{g\ cm^{-3}}$) and stiffer at high ρ ($\Gamma \approx 2.75$ in the Shen model). The Shen EoS predicts a TOV maximum gravitational mass of 2.2$M_\odot$.

3.3 Cases

In Table 4.1, we present the initial data for the cases we evolve. For this study, we do not consider the effects of the binary mass ratio $q = M_{\rm BH}/M_{\rm NS}$ and set $q = 3$ throughout. For each case, we set the NS baryonic mass to 1.55$M_\odot$. We wish to study cases that lead to massive disks, and so we include in each case an initial BH spin of $s \equiv \left|\vec{S}_{\rm BH}\right|/M_{\rm BH}^2 = 0.5$ orthogonal to the orbital plane. Finally, we neglect the NS spin altogether and focus solely on what is thought to be a good approximation for the most likely scenarios: irrotational stars [13, 56].

To study the effect of compaction, we ran two cases with $\Gamma = 2.75$, one with $\mathcal{C} = M_{\rm NS}/R_{\rm NS} = 0.146$ and one with $\mathcal{C} = 0.173$. These runs are labeled "Γ2.75c.15" and "Γ2.75c.17" in the tables and figures below. For our chosen rest mass, the NS gravitational mass is about $M_{NS} = 1.4M_\odot$, so the two compactions correspond to radii of 14.4km and 12.1km.

To separate the effects of the EoS from those of the compaction, we use three

equations of state with the same $R_{\rm NS}$ ($\mathcal{C} = 0.15$). This comparison has not been attempted in previously published full-GR numerical studies. We use two Γ-law EoS: $\Gamma = 2$ (run "Γ2") and $\Gamma = 2.75$. We also use the tabulated Shen EoS. As mentioned above, we evolve the initial data with Shen EoS in two ways: assuming instantaneous β-equilibrium (run "Shen-β") and assuming $S_\nu = 0$ (run "Shen-Adv").

All the initial configurations are generated using our multidomain spectral elliptic solver [92] to solve for quasi-equilibrium configurations of BHNS binaries in the extended conformal thin sandwich formalism [40]. We do not assume conformal flatness, but instead choose a conformal metric approaching Kerr in the neighborhood of the BH [71, 40]. For the polytropic runs, the initial temperature $T_{\rm init}$ is zero. For the Shen runs, $T_{\rm init} = 0.1$MeV, and the initial Y_e is set by assuming β-equilibrium. To ensure that the comparison is not affected by the initial eccentricity of the binary, we also apply the eccentricity removal technique devised by Pfeiffer et al. [91] until $e \sim 0.01$. (Without eccentricity removal, we would have $e = 0.01 - 0.06$.)

3.4 Results

3.4.1 Qualitative features of the mergers

For each configuration, the binary passes through 2 – 3 orbits of inspiral before reaching a coordinate separation of $d \approx$40km ($5M$), at which point matter starts flowing from the star to the BH. Most of the core of the star is then rapidly accreted onto the hole [within $t \sim$3ms ($100M$)] while a large tidal tail forms. For

Table 3.1: Initial data for all runs. $d_{\rm init}$ is the initial coordinate separation and $\rho^{\rm c}_{14}$ is the central density of the star in units of $10^{14}{\rm g\ cm^{-3}}$ assuming a star of baryonic mass $M_b^{\rm NS} = 1.55 M_\odot$. $e = \frac{B}{\omega d}$ is the eccentricity and B is obtained by fitting the evolution of the trajectory to $\dot{d} = A_0 + A_1 t + B\sin(\omega t + \phi)$

$Case$	EoS	$s_{\rm init}$	q	$\mathcal{C}_{\rm init}$	$\Omega_{\rm init} M$	$d_{\rm init}/M$	$\rho^{\rm c}_{14}$	e
$\Gamma 2$	$\Gamma = 2.00$	0.5	3	0.144	0.041	7.48	7.1	0.006
$\Gamma 2.75c.15$	$\Gamma = 2.75$	0.5	3	0.146	0.041	7.45	4.5	0.003
$\Gamma 2.75c.17$	$\Gamma = 2.75$	0.5	3	0.173	0.041	7.42	7.6	0.014
Shen$-\beta$	Shen	0.5	3	0.147	0.041	7.59	5.0	0.004
Shen $-$ Adv	Shen	0.5	3	0.147	0.041	7.59	5.0	0.004

every EoS, even the stiffest ($\Gamma = 2.75$), the star is disrupted in one extended mass transfer event. This confirms earlier indications that episodic mass transfer does not happen in GR for the realistic range of neutron star EoS. All tails but the one formed by the most compact star extend to distances $d \geq$400km. All of this material, however, remains bound to the system. This result is significant because our Shen-EoS runs do account for recombination effects that occur for $\rho < 10^{14}{\rm g\ cm^{-3}}$. It would seem that it is the inclusion of GR, and not inferior microphysics, that causes GR simulations to see no ejecta. (It is, however, possible that some very low-density material is ejected and that this is suppressed in our simulations by the atmosphere prescription.)

Material from the tail falling back towards the hole has enough angular momentum to avoid being immediately accreted: once the core of the star has fallen into the black hole, the accretion rate drops and a disk forms from the remains of the tail. This disk is at first neither axisymmetric nor time-independent: the density peaks strongly at the junction of the disk and the tidal tail, and the mat-

Table 3.2: The properties of the BH and accretion torus at time $t = t_{\rm merger} + 8.3$ms. $v_{\rm kick}$ is the BH kick velocity in km s^{-1}. $M_{\rm disk}$ is the baryonic mass outside of the black hole, r is the radial extent of the disk, $\rho^{\rm max}_{\rm disk,12}$ is the maximum density in units of 10^{12}g cm^{-3}, $\langle T \rangle_{\rm disk}$ is the density-weighted average temperature in MeV and $\Psi_4^{2,2}$ is the amplitude of gravitational waves in the (2,2) mode extracted at $r = 75M$. Note that the disk continues to evolve at late times as $r_{\rm disk}$ and $\langle T \rangle_{\rm disk}$ slowly increase.

$Case$	$M_{\rm BH}/M$	$s_{\rm final}$	$v_{\rm kick}$	$M_{\rm disk}/M_{\rm NS}$	$r_{\rm disk}/M$	$\rho^{\rm max}_{\rm disk,12}$	$\langle T \rangle_{\rm disk}$	$rM\Psi_4^{2,2}$
$\Gamma 2$	0.96	0.69	83	0.08	12	1	1.3	0.012
$\Gamma 2.75c.15$	0.94	0.69	45	0.13	12	1	0.6	0.010
$\Gamma 2.75c.17$	0.96	0.70	75	0.02	6	0.3	1.2	0.030
Shen $-\beta$	0.97	0.79	63	0.07	10	1	2.7	0.015
Shen $-$ Adv	0.97	0.80	61	0.07	11	1	2.5	0.016

ter keeps expanding away from the hole. As the accretion rate decreases, a gap opens between the disk and the black hole. At the end of our simulations, the outer disk is still quite nonaxisymmetric, and the tidal tail is settling back onto the disk. The inner disk has a density $\rho \sim 10^{11} - 10^{12}\,{\rm g\,cm^{-3}}$ and temperature $T \sim 0.1 - 10\,{\rm MeV}$. It is also relatively thick ($H_{\rm disk}/R_{\rm disk} \sim 0.1 - 0.3$).

3.4.2 Effects of composition, compaction, and stiffness

The effects of the EoS on the gravitational wave spectrum and on the post-merger disk mass are shown in figures 3.1 and 3.2. The leading contribution from the EoS is related to the compaction of the star. As Shibata *et al.* [119, 117] found for $\Gamma = 2$ stars, we observe that a higher compaction leads to stronger gravitational waves and a smaller disk. The more compact star reaches the ISCO

with minimal distortion and falls nearly entirely into the black hole, with only a small fraction of its mass sent out in a relatively short tidal tail extending to $d \sim$250km. The tail forms a small disk of mass $\approx 0.02 M_{NS}$. The cutoff frequency of the gravitational waves ($f \sim 2$kHz) is higher than for more extended stars ($f \sim 1$kHz for Γ2.75c.15).

By comparison, modifying the EoS while keeping the compaction constant seems to have more modest effects. For NS compaction of $\mathcal{C} = 0.15$, every EoS predicts a final disk mass $\sim 0.05 - 0.1 M_{\rm NS}$, i.e. $M_{\rm disk} \approx 0.1 M_{\odot}$. The density-weighted average temperature of the disk is 1-2MeV, although some regions in the disks reach $T \approx 20$MeV. Differences in the gravitational wave signal are more visible: the $\Gamma = 2.75$ star has a lower cutoff frequency and peak amplitude. But even then, the differences remain smaller than those due to the compactness of the star. The close similarity of the Shen and $\Gamma = 2$ waveforms is surprising. A partial explanation may lie in the fact that the Shen-EoS is actually very soft at the densities of the matter after the NS is disrupted. In these regimes, Shen is closer to $\Gamma = 2$ than to $\Gamma = 2.75$.

Another strong effect of the stiffness of the EoS is the different behaviors of the tidal tails, which can lead to important effects on the post-merger disk dynamics. For all EoS, our simulations end with $0.06 - 0.07 M_{\rm NS}$ of matter within 200km of the BH — either in the disk or in the process of joining it. The mass and size of the tidal tail, however, vary: for the $\Gamma = 2.75$ star, the tail mass is $0.06 M_{\rm NS}$ and more than 2% of the matter will eventually go as far as 2000km away from the BH before falling back on a timescale of 200ms (assuming geodesic motion). When the tail is maximally extended, our grid would be unable to adequately resolve the whole system. Therefore, we stop evolving when the tail is still

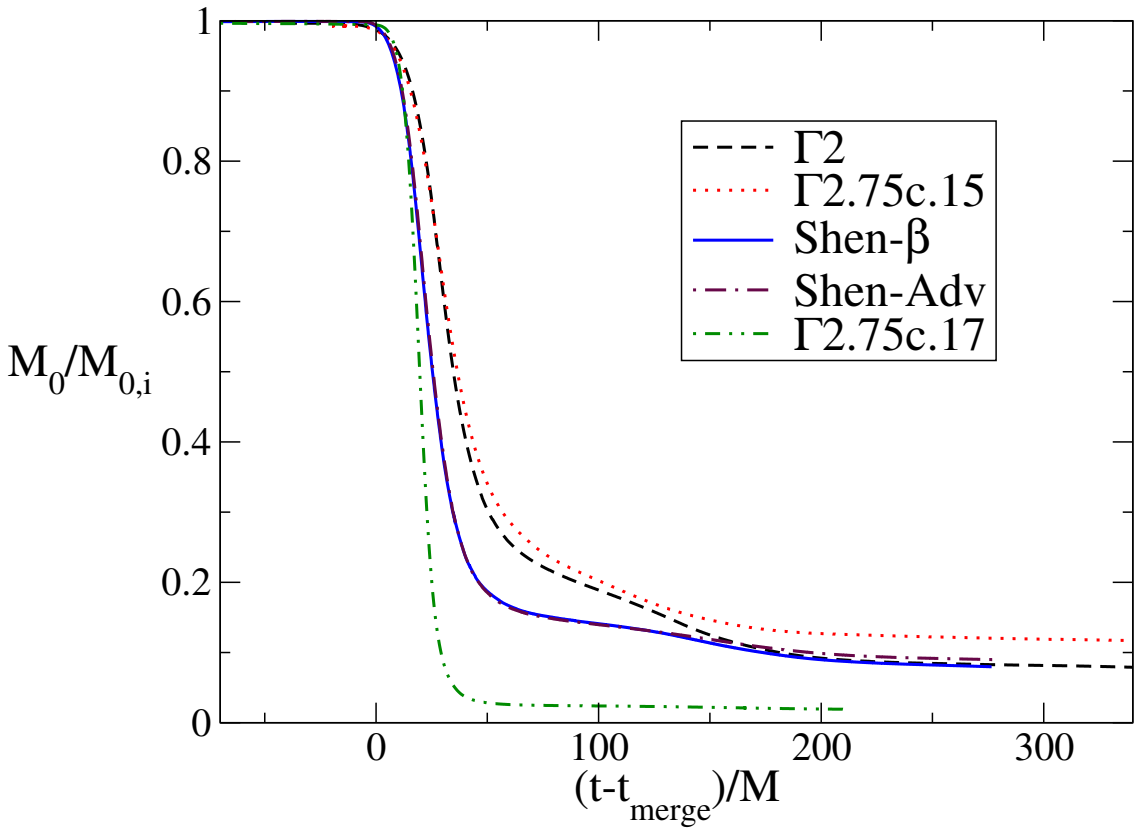

Figure 3.1: The effect of EoS on the disk mass. M_0 is the total baryonic mass outside the BH.

expanding. On the other hand, the $\Gamma = 2$ EoS leads to a much smaller tail, with a mass of $0.02M_{\rm NS}$. Only a negligible amount of matter reaches a distance of 500km, and most of the matter would fall back on the disk within 25ms of the disruption. For both polytropes, interactions between the disk and the tail are strong enough to keep the disk from settling to an axisymmetric state over the duration of our simulation. The Shen case also has a tail of mass $0.02M_{\rm NS}$, but it is thicker and falls back more rapidly onto the disk. The disk will settle more quickly, and is much closer to axisymmetry at the end of our simulation.

For both Shen-β and Shen-Adv runs, the density-weighted average of Y_e re-

mains close to $\langle Y_e \rangle = 0.09$ throughout the inspiral, so the inspiral is essentially identical for the two runs. The mergers are also similar, although the Shen-β waveform decays somewhat more rapidly. The composition of the disk, however, is radically different. For Shen-Adv, the final $\langle Y_e \rangle$ is about 0.09. (It decreases slightly, even though there are no Y_e source terms, because the more highly-leptonized central region of the NS is swallowed by the BH.) The baryon mass is about 86% free neutrons, 7% heavy nuclei, 5% free protons, and 2% alpha particles. The nuclei have an average $\langle A \rangle \approx 95$, $\langle Z \rangle \approx 30$. If β-equilibrium is enforced, $\langle Y_e \rangle$ increases to 0.2 as the NS matter decompresses. The baryon mass is about 65% free neutrons, 25% heavy nuclei ($\langle A \rangle \approx 75$, $\langle Z \rangle \approx 30$), 9% free protons, and 1% alpha particles. The disks produced by the Shen-β and Shen-Adv mergers have similar densities and temperatures: the density-weighted average temperature is about 2.5MeV for Shen-Adv and 2.7MeV for Shen-β, although in each case the maximum temperature reaches $\approx$ 12MeV, and the average is slowly increasing.

3.4.3 The final black hole and disk state

The final state of the black hole is given in Table 3.2. The final spin $s_{\rm final}$ is in the range 0.7-0.8, with the Shen runs having higher $s_{\rm final}$ because they merge somewhat more quickly and have less time to radiate angular momentum. The BH kick velocity is $\sim$10-100km s^{-1}

In figure 3.3, we plot the profiles of the density ρ, specific entropy s, and specific angular momentum $j = u_\phi/u_{\rm t}$ for run Shen-β at final time t =10ms after the merger. By 3ms after merger begins, a distinct torus forms around the

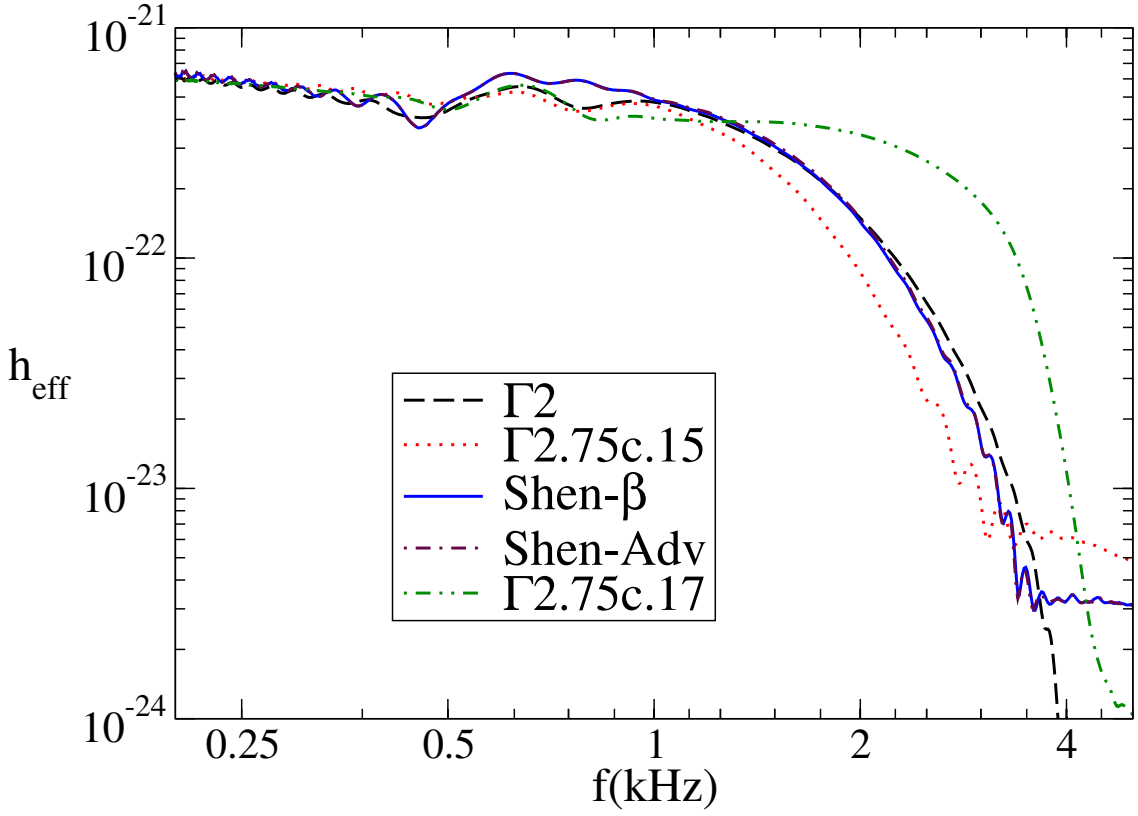

Figure 3.2: The effective amplitude, as defined in Eq. (41) of [117], for each run. The assumed distance from the source is 100Mpc.

BH. By 5ms after merger, matter begins to clear out in the region near the hole, and the accretion rate $\dot{M}_{\rm disk}$ drops to a low value ($\tau = M_{\rm disk}/\dot{M}_{\rm disk} \approx 24$ms). The torus has a maximum density of $\rho = 10^{12}$g cm^{-3} located at a coordinate radius of $r = r_c = 30$km from the BH. The width of the torus is ≈ 20km, and the height is ≈ 10km. At this time, the disk itself has not yet stabilized. The gas more than 20km from the BH has nearly constant s and j, while the gas nearer the hole has somewhat higher s and much lower j. Subsequent motions in the fluid lead to modest but positive radial gradients for s and j in most of the high-density region, the exception being the small but negative entropy gradient that persists around $r \approx 30$km. In the still-settling, lower-density outer regions, s and j drop

significantly. The angular velocity Ω decreases with r everywhere: $\Omega \sim r^{-1.2}$ in the high-density region. The assumption of β-equilibrium is probably not good in the outer regions of the disk, which are optically thin to neutrino emission. The profiles of ρ and j are quite similar for the Shen-Adv disk, so these variables appear to depend weakly on Y_e.

The longer-term evolution of the disk depends on physical processes not included in these simulations. Since $d\Omega/dr < 0$, our disks are subject to the magnetorotational instability (MRI) [9]. Turbulence induced by this instability might have the effect of an α-viscosity of magnitude $\alpha \sim 0.01 - 0.1$ [114]. This will heat the disk, redistribute angular momentum, and drive accretion. The disk's only significant cooling mechanism is neutrino emission [96, 21]. 3D Newtonian simulations predict that a neutrino-cooled disk with $\alpha \sim 0.1$ and $M_{\rm disk}$ similar to ours will accrete on a timescale of $\sim$0.1 second and release energy in neutrinos at a rate $L_\nu \sim 10^{53}$erg s^{-1}, possibly making such a merger remnant a viable GRB candidate [110].

3.5 Conclusions

We have investigated the influence of the equation of state on BHNS binaries. We find that the NS compaction has a strong influence on the disk mass and the cutoff frequency of the gravitational waveform. The effects of EoS stiffness for a fixed compaction are weaker. The overall behavior of the merger was found to be independent of EoS stiffness—we never find episodic mass transfer or unbound ejecta. The stiffness of the EoS in the lower-density outer layers of the NS does affect the merger dynamics, with stiffer EoS leading to larger and

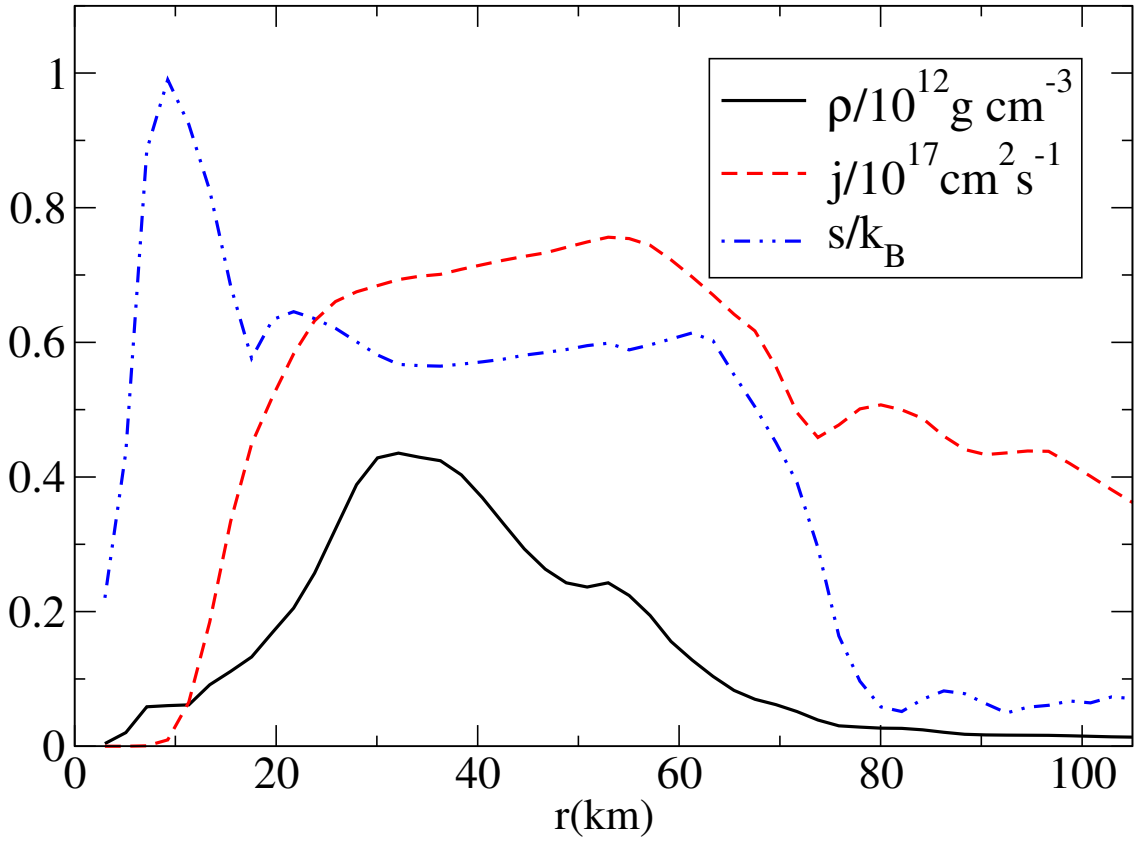

Figure 3.3: The density ρ, specific angular momentum j, and specific entropy s of the Shen-β disk as a function of cylindrical radius r, shown 10ms ($370M$) after the merger. Each point is a ρ-weighted average over the angular and vertical directions.

longer-lived tidal tails, and this effect manifests itself in the merger waveform. We find that the evolution of Y_e weakly influences the waveform and the final disk mass.

Our simulations suffer from two classes of limitations. First, we have considered only a very small sample of the interesting BHNS parameter space. It is possible that the effects of EoS stiffness are more pronounced at different binary mass ratios or different BH spins. Also, we have considered only three EoS. A

more systematic approach would be to use a single EoS with adjustable parameters (e.g. [101, 59]). An adequate EoS for this purpose would have to cover the range of likely NS stiffness and radius while capturing all of the important physical EoS features, including (for the post-merger evolution) its complicated temperature and composition dependence. Other important areas for improvement involve our treatment of the NS microphysics. To evolve the final disks realistically, the effects of neutrino radiation on the temperature and composition of the matter must be included. The evolution of the disk is also strongly affected by the presence of magnetic fields, and in particular by the MRI. Simulations that include radiation and magnetohydrodynamics are needed to assess the ability of these disks to produce GRBs.

CHAPTER 4

EFFECTS OF THE ORIENTATION OF THE BLACK HOLE SPIN

This chapter was originally published in Phys.Rev.D. [39]. It was written in close collaboration with Matthew Duez, who was mostly responsible for the simulation and analysis of the highly spinning binary (case s.9i0), as well as the convergence tests describe in Section 4.3. The code improvements described in Section 4.2 were developed jointly by Matthew Duez and Francois Foucart.

4.1 Introduction

Black hole-neutron star (BHNS) binary mergers present a remarkable opportunity to study strongly-curved spacetime and supernuclear-density matter in the most extreme, dynamical conditions. BHNS binaries in compact orbits emit strong gravitational waves, and they are expected to be one of the main sources for Advanced LIGO and VIRGO [67, 30]. Current estimates for the event rates of binary mergers coming from population synthesis models predict that Advanced LIGO will see about 10 BHNS/yr, although uncertainties in the models allow for a large range of potential event rates, ~ 0.2 – 300 BHNS/yr [106]. These gravitational waves contain, in principle, a wealth of information on their source, such as the mass and spin of the black hole (BH) and the mass and radius of the neutron star (NS). Inferred properties of the NS could be used to constrain the NS equation of state. Information in the waves can only be extracted, however, by comparison with accurate numerically-generated predictions that provide the expected waveform for each possible BHNS system.

Mergers of BHNS binaries have also been proposed as potential progeni-

tors of short-hard gamma-ray bursts (SGRB) [83]. The origin of SGRBs is not yet known, although it is certain that the engines are compact and located at cosmological distances, and there is evidence (such as their presence in nonstar forming regions) to support a mechanism different from that associated with long-soft GRBs, namely stellar core collapse. For BHNS mergers, the generation of a SGRB is possible only if the remnant black hole is surrounded by a massive, hot, thick accretion disk. Also, to obtain relativistic jets and a beamed outflow, a region mostly devoid of any matter is necessary (see e.g. [60] and references therein). Only numerical simulations in full general relativity with realistic microphysics can determine if these conditions are likely to be obtained.

Whether a disk forms or not will depend on the premerger characteristics of the binary, especially the BH mass, the NS radius, and the BH spin. Current estimates from population synthesis models suggest that most systems are likely to be formed with a black hole of $\sim 10M_{\odot}$. Relativistic simulations to date have considered cases of relatively low mass black holes ($\sim 2-7M_{\odot}$) [121, 122, 119, 117, 31, 28, 33, 26], for which the NS is expected to disrupt outside the innermost stable circular orbit (ISCO), making disk formation more likely. These simulations have found cases of massive disk formation, with $M_{\rm BH} \sim 3-4M_{\odot}$ resulting in the largest disks [33]. The NS radius is the parameter related to the equation of state that has the largest effect on the waveform and post-merger disk [26], with larger radii resulting in larger disks [119, 26].

The spin of the black hole can have a strong influence on the merger. The ISCO is smaller for prograde orbits around a spinning BH than for orbits around a nonspinning hole. Because disk formation is expected to be more likely if NS tidal disruption occurs outside the ISCO than if it occurs inside, BH spin can

facilitate disk formation. With high BH spin, it is even plausible that BHNS binaries with the most likely mass ratios ($\sim$7:1) give rise to substantial disks [38]. The magnitude of the BH spin is largely unconstrained by population synthesis models, as it comes mostly from the spin acquired during formation of the black hole in a core-collapse event [12]. The effect of aligned and antialigned spins was investigated in full general relativity for the 3:1 mass-ratio case by Etienne *et al.* [33]. They found that a large aligned spin (and correspondingly small ISCO) leads to a much more massive post-merger disk. For example, for $a_{\rm BH}/M_{\rm BH} = 0.75$ and $M_{\rm BH} \sim 4M_\odot$, a disk of $M_{\rm disk} \sim 0.2M_\odot$ can be obtained. For BHNS binaries with massive black holes ($M_{\rm BH} \sim 10M_\odot$), forming a disk may in fact only be possible if the hole is spinning.

There is no reason to expect the black hole spin to be aligned with the orbital angular momentum. Population synthesis models predict a relatively wide distribution of orientations, with about half of the binaries having a misalignment between the BH spin and the orbital angular momentum of less than 45° when the initial BH spin is $a_{\rm BH}/M_{\rm BH} = 0.5$ [12]. Misalignment can reduce or reverse the BH spin effects described above. This can be understood by considering prograde orbits of test particles with small radial velocity, which become unstable farther away from the BH for inclined orbits than for equatorial orbits of the same angular momentum. Misalignment will also produce qualitatively new effects, including the precession of the premerger orbital plane and BH spin. The influence of misalignment has been studied for 10:1 mass-ratio binaries in the approximation that the spacetime is assumed to be Kerr. Rantsiou *et al.* [99] showed that, in this approximation, disks can be formed only at relatively low inclinations and only for near extremal black holes. Ultimately, though, simulations in full general relativity are needed to accurately model such systems.

In this paper, we report on fully relativistic studies of misaligned BHNS binaries. We limit ourselves to small mass systems ($M_{\rm BH} \sim 4.2 M_\odot$) and a simplified equation of state, but we consider a significant range of black hole spin magnitudes and orientations. We confirm the results of Etienne *et al* [33] regarding the effects of an aligned BH spin. For misaligned spins, we find that the misalignment angle can have a strong effect on the post-merger disk mass, but only for angles greater than around 40°. Although the disk mass varies greatly with BH spin, most other disk properties are very similar, including the accretion timescale, the location of the maximum density, the average temperature, and the entropy and angular momentum profiles. The disks are all thick, each with a height H to radius r ratio $H/r \approx 0.2$, nearly independent of r. Crucially, they all have a baryon-clear region above and below the BH. The disks are misaligned with the final BH spin by $\leq 15^\circ$. They do precess about the BH spin axis, but without reaching a fixed precession rate. Indeed, the steady-state precession timescale is expected to be significantly longer than the accretion timescale.

This paper is organized as follows. In Sec. 4.2, we discuss the method used to construct the very general BHNS initial data we use. We also discuss in detail the improvements to our evolution code that have increased the accuracy by an order of magnitude over the results presented in Duez *et al.* [28]. We then present our run diagnostics in Sec. 4.3. The different cases to be evolved are described in Sec. 4.4. We then present the results of the simulations in Secs. 4.5 and 4.6. Finally, we draw conclusions in Sec. 4.7.

4.2 Numerical methods

4.2.1 Initial data

For numerical evolutions of Einstein's equations, we decompose the spacetime under study into a foliation of spacelike hypersurfaces parametrized by the coordinate t. Einstein's equations can be written in the form of hyperbolic evolution equations plus a set of constraints that have to be satisfied on each $t = \text{constant}$ slice. Our initial data at $t = 0$ must be chosen such that it satisfies these constraints. We construct initial data using the Extended Conformal Thin Sandwich formalism (XCTS) [138, 87]. If we write the spacetime metric as

$$\begin{aligned} ds^2 &= g_{\mu\nu} dx^\mu dx^\nu \\ &= -\alpha^2 dt^2 + \psi^4 \tilde{\gamma}_{ij} (dx^i + \beta^i dt)(dx^j + \beta^j dt), \end{aligned} \tag{4.1}$$

the initial data to be determined include the lapse α, the shift vector β^i, the conformal factor ψ, the conformal 3-metric $\tilde{\gamma}_{ij}$ and the extrinsic curvature $K_{\mu\nu} = -\frac{1}{2}\mathcal{L}_n g_{\mu\nu}$ (where $\mathcal{L}_n$ is the Lie derivative along the normal $\boldsymbol{n}$ to the $t = 0$ slice). The constraints can be expressed as a set of 5 coupled elliptic equations for the lapse, shift, and conformal factor [87]. The physical properties of the system are then determined by the choice of the remaining free parameters: the trace of the extrinsic curvature $K = g_{\mu\nu} K^{\mu\nu}$, the conformal metric $\tilde{\gamma}_{ij}$, their time derivatives $\partial_t K$ and $\partial_t \tilde{\gamma}_{ij}$, and the matter stress-energy tensor $T^{\text{matter}}_{\mu\nu}$.

The system of elliptic equations is solved using the spectral elliptic solver SPELLS developed by the Cornell-Caltech collaboration [92], and initially used to construct initial data for binary black hole systems by Pfeiffer *et al.* [90, 87]. A detailed presentation of the methods used for the construction of BHNS initial

data was given in Foucart *et al.* [40]. Here, we limit ourselves to a brief summary plus a description of the changes made to accommodate the possibility of arbitrary spin orientation.

As the system is expected to be initially in a quasiequilibrium state, with the binary in a low-eccentricity circular orbit of slowly decreasing radius, we work in a frame comoving with the binary and set the time derivatives to zero: $\partial_t K = 0$ and $\partial_t \tilde{\gamma}_{ij} = 0$. As for $\tilde{\gamma}_{ij}$ and K, we make a choice inspired by the results of Lovelace *et al.* [71] for binary black hole systems. Close to the BH, the metric matches its Kerr-Schild values for a BH of the desired mass and spin, while away from the BH, the conformal metric is flat and $K = 0$. The transition between these two regions is done by using the following prescription:

$$\tilde{\gamma}_{ij} = \delta_{ij} + [\gamma_{ij}^{KS}(a_{\rm BH}, \mathbf{v}_{\rm BH}) - \delta_{ij}] e^{-\lambda (r_{\rm BH}/w)^4}, \tag{4.2}$$

$$K = K^{KS}(a_{\rm BH}, \mathbf{v}_{\rm BH}) e^{-\lambda (r_{\rm BH}/w)^4}, \tag{4.3}$$

$$\lambda = \frac{r_{\rm BH} - r_{\rm AH}}{r_{\rm NS}/q - r_{\rm BH}}, \tag{4.4}$$

$$\mathbf{v}_{\rm BH} = \mathbf{\Omega}^{\rm rot} \times \mathbf{c}_{\rm BH}, \tag{4.5}$$

where the KS subscript refers to the Kerr-Schild values, $r_{\rm BH}$ ($r_{\rm NS}$) is the coordinate distance to the center of the BH (NS), $r_{\rm AH}$ the coordinate radius of the BH apparent horizon, $a_{\rm BH}/M_{\rm BH}$ is the dimensionless spin of the BH, $q \sim M_{\rm NS}/M_{\rm BH}$ a constant of the order of the mass ratio, $\mathbf{c}_{\rm BH}$ the coordinate location of the BH center with respect to the center of mass of the system, and w is some freely specifiable width, chosen so that the metric is nearly flat at the location of the NS. The parameter λ, which is designed to impose a flat background at the location of the NS, is set to ∞ for $r_{\rm NS} < q r_{\rm BH}$.

Boundary conditions are imposed at infinity and on the apparent horizon of the BH (since the inside of the BH is excised from our computational domain).

The boundary conditions at infinity are chosen so that the metric is asymptotically flat, while the inner boundary conditions follow the prescriptions of Cook and Pfeiffer [23], which make the inner boundary an apparent horizon in quasiequilibrium. There is some freedom in these boundary conditions: on the apparent horizon, the conformal lapse is not fixed (we set it to the value of an isolated Kerr BH), and the shift is determined only up to a rotation term $\beta'^i = \beta^i + \epsilon^{ijk}\Omega^{\rm BH}_j x_k$. The value of $\mathbf{\Omega}^{\rm BH}$ determines the spin of the BH, but the exact relation between $\mathbf{\Omega}^{\rm BH}$ and the spin is unknown *a priori*; to get the desired BH spin, we have to solve iteratively for $\mathbf{\Omega}^{\rm BH}$. On the outer boundary, the shift can be written as

$$\boldsymbol{\beta} = \mathbf{\Omega}^{\rm rot} \times \mathbf{r} + \dot{a}_0 \mathbf{r} + \boldsymbol{v}_{\rm boost} \tag{4.6}$$

where $\mathbf{\Omega}^{\rm rot}$ allows for a global rotation of the coordinates, $\dot{a}_0$ for a radial infall with velocity $\mathbf{v} = \dot{a}_0 \mathbf{r}$, and $\boldsymbol{v}_{\rm boost}$ for a boost. As an initial guess for the orbit of the binary, we can set the radial velocity at $t = 0$ to 0 ($\dot{a}_0 = 0$). This assumption, as well as the quasiequilibirum formalism, clearly neglects the evolution of the orbit over time through the radial infall of the binary and the precession of the orbital plane. Both effects are, however, acting over relatively long timescales: over its first orbit, even the binary with the most inclined spin considered here (s.5i80 in the later sections) goes through less than 10% of a full precession period of the BH spin while the coordinate separation between the compact objects is reduced by about 20%. One known effect of the quasi-circular approximation is that the binary will have a nonzero eccentricity. The eccentricity can be decreased by modifying the initial values of $\dot{a}_0$ and $\mathbf{\Omega}^{\rm rot}$ [91] (see also [40] for an application of that method to BHNS binaries) as long as the initial eccentricity and orbital phase can be accurately measured. Here, we only apply this technique when the spin of the BH is aligned with the orbital angular momentum of

the binary. For precessing binaries, significantly reducing the eccentricity would require a larger initial separation for which the effects of eccentricity, precession and radial infall can be properly disantangled.

In the presence of matter, additional choices are required. We assume that the fluid is in hydrostatic equilibrium in the comoving frame, and require that its 3-velocity is irrotational. The first condition gives an algebraic relation between the enthalpy h of the fluid, its 3-velocity v_i, and the metric $g_{\mu\nu}$, while the second leads to another elliptic equation determining the velocity field. These equations are coupled to the constraints: the whole system can only be solved through an iterative method. For a BH with a spin aligned with the total angular momentum of the system, that method is described in Foucart *et al.* [40]: we solve for the metric using SPELLS, then determine the new value of the enthalpy h, as well as the orbital angular velocity $\mathbf{\Omega}^{\rm rot}$ (chosen so that the binary is in quasicircular orbit), the position of the BH in the equatorial plane (so that the total linear momentum $P_{\rm ADM}$ vanishes), and the free parameter $\Omega^z_{\rm BH}$ (to drive the spin of the BH to its desired value). Finally, we solve for the velocity field through the elliptic equation imposing an irrotational configuration, and go back to the first step.

In order to construct initial data for BHs with a spin that is not aligned with the orbital angular momentum of the binary, a few changes are necessary. First, we do not assume that $\mathbf{\Omega}^{\rm BH}$ is aligned with the orbital angular momentum. Instead, all 3 components of $\mathbf{\Omega}^{\rm BH}$ are solved for. We also abandon the assumption of equatorial symmetry, and control the position of the BH along the z-axis of the orbital angular momentum by requiring that the NS is initially moving in the xy-plane, with its center in the $z = 0$ plane (the z coordinate of the location

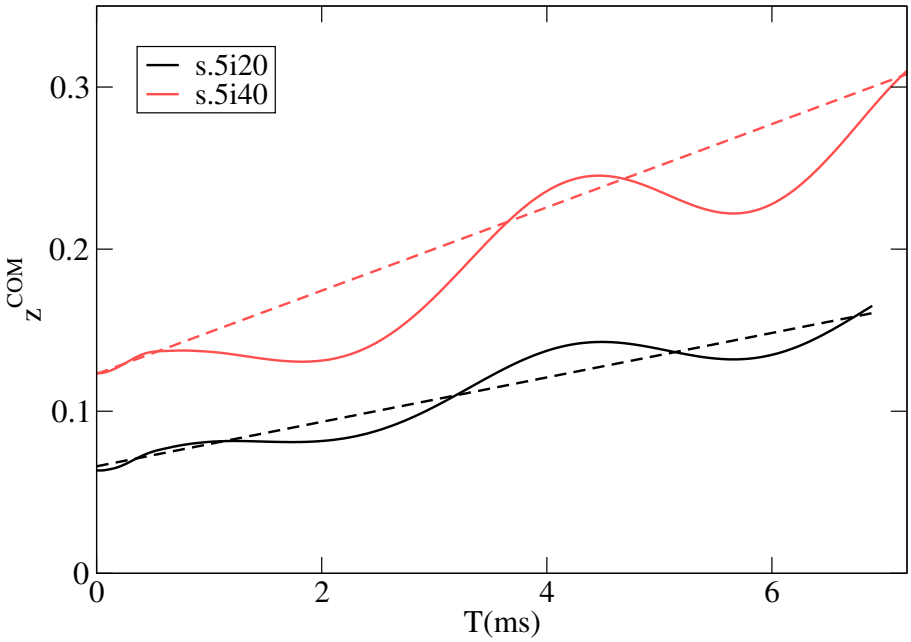

Figure 4.1: Evolution of the position of the center of mass along the z-axis during inspiral (solid line), compared to the motion expected from the boost $\boldsymbol{v}^z_\infty$ given in the initial data (dotted line).

of the BH is chosen so that the condition $\hat{e}_z.\nabla h = 0$ is satisfied at the center of the NS). Finally, to guarantee that $P^z_{\rm ADM} = 0$ we impart a boost to the whole system through the boundary condition at infinity: $\boldsymbol{v}^z_{\rm boost} = v^z_\infty$. The center of mass is then expected to have a global motion during inspiral corresponding to that boost, and we check in Fig. 4.1 that this is indeed the case. By adding these conditions to the iterative procedure used to generate BHNS initial data, we are able to obtain high-precision initial configurations for arbitrary values of the orientation of the BH spin.

4.2.2 Evolution

The simulations presented here use the SpEC code developed by the Cornell-Caltech-CITA Collaboration [2]. To evolve BHNS systems, the two-grid method described in Duez *et al.* [28] is used. Einstein's equations are evolved on a pseudospectral grid, using the first-order generalized harmonic formulation [68], while the hydrodynamical equations are solved on a separate finite difference grid called the "fluid grid". The hydrodynamic equations are written in conservative form

$$\partial_t \mathbf{U} + \nabla \mathbf{F}(\mathbf{U}) = \mathbf{S}(\mathbf{U}). \tag{4.7}$$

To compute the flux $\mathbf{F}$ on the faces of each finite difference cell, we use the third-order shock capturing PPM reconstruction method [22]. More details on the numerical methods used can be found in Duez *et al.* [28]. However, since the publication of [28], several important improvements have been made to the code, which are described in the following subsections.

Dynamic regridding

To accurately evolve a BHNS binary while determining its gravitational wave emission, simulations have to resolve events occurring at very different scales. When the neutron star is disrupted and a disk forms, we expect shocks in the disk, and steep density and temperature gradients close to the BH. But the disruption of the star also leads to the creation of a long tidal tail which can initially contain up to $5-10\%$ of the initial mass of the star and expand hundreds of kilometers away from the center of the BH [26]. Clearly, both the sharp, small-scale features around the black hole and the large-scale tidal tail should be properly

resolved if we want to follow the formation of an accretion disk. Furthermore, to extract gravitational waves accurately, the evolution of the gravitational fields should extend to the wave zone, in regions where no matter at all is present.

Because we use different grids to evolve the metric and the fluid variables, the spectral grid on which we solve the generalized harmonic equations can be extended into the wave zone while the fluid grid used for the relativistic hydrodynamical equations only covers the region where matter is present. Our earlier simulations [28] were limited to nonspinning black holes. In that case, most of the matter was rapidly accreted onto the hole and the tidal tails and accretion disks were small enough that manually expanding the fluid grid at a few chosen timesteps allowed us to resolve the evolution of the fluid at a reasonable computational cost. For spinning black holes, this is no longer the case: cost-efficient evolutions require a grid with points concentrated in the high-density regions close to the BH, and coarser resolution in the tail. Furthermore, as the evolution of the fluid is highly dynamical, interrupting the simulation whenever the finite difference grid is no longer adapted to the fluid configuration becomes impractical. One solution would be to use an adaptive mesh refinement scheme, similar to the codes used by Yamamoto et al. [136] and Etienne et al. [33]. In our code, we choose instead to use a map between the fluid grid and the pseudospectral grid that concentrates grid points in the region close to the black hole and automatically follows the evolution of the fluid.

To do this, we measure the outflow of matter across surfaces close to but inside of the fluid grid boundaries. As soon as the outflow across one of these surfaces crosses a given threshold (chosen so that the amount of matter leaving the grid over the whole simulation is negligible compared to the final mass of

the accretion disk), the grid expands. The opposite is done on fixed surfaces farther away from the grid boundaries to force the grid to contract whenever the fluid is moving away from a boundary. The map itself is the combination of:

(i) A translation of the center of the grid, to follow the general motion of the fluid

(ii) A linear scaling of each coordinate axis, to adapt to its expansions and contractions

(iii) A radial map smoothly transitioning from a high resolution region close to the black hole to a lower resolution region far away from it. The exact form of the map is

$$r' = \begin{cases} r, & r < r_A \\ f(r) - f(r_A) + r_A, & r_A < r < r_B \\ \lambda(r - r_B) + f(r_B) - f(r_A) + r_A, & r > r_B \end{cases} \tag{4.8}$$

$$f(r) = r(ar^3 + br^2 + cr + d), \tag{4.9}$$

where the coefficients (a, b, c, d) are chosen so that the map is C^2 at r_A and r_B and λ is chosen so that the grid is of the desired size. The radii r_A and r_B are fixed for the whole evolution and will determine respectively the minimum resolution in the neighborhood of the black hole and the characteristic lengthscale of the transition between the high and low resolution regions.

Excision

We find that our hydrodynamics code is more stable near the excision zone if we switch from PPM to the more diffusive MC reconstruction [134] in the vicinity

of the excision zone. Therefore, we replace the face values determined by PPM reconstruction, ${u_{R,L}}^{PPM}$ with a weighted average:

$$u_{R,L} = f{u_{R,L}}^{MC} + (1-f){u_{R,L}}^{PPM} , \tag{4.10}$$

where $f = 1$ for $r < r_1 \sim 2r_{\rm ex}$ and $f = e^{-[(r-r_1)/r_1]^2}$ for $r > r_1$.

The MC face-value computation must be altered when its regular stencil would extend into the excised region, and doing this properly turns out to be important for stability. Consider a one-dimensional problem with grid points $x_n = n\Delta x$. Then the face-value reconstruction of the function u_i from the left $u_{L,i-1/2} = u_{i-1/2-\epsilon}$ and from the right $u_{R,i-1/2} = u_{i-1/2+\epsilon}$ must be adjusted as follows.

(i) If x_i is in the excision zone, but x_{i-1} is outside, set $u_{L,i+1/2} = u_{i-1}$ and $u_{R,i+1/2} = u_{i-1}$

(ii) If x_i is in the excision zone, but x_{i+1} is outside, set $u_{L,i-1/2} = u_{i+1}$ and $u_{R,i-1/2} = u_{i+1}$

(iii) If x_i is outside the excision zone, but x_{i-1} is inside, set $u_{L,i-1/2} = u_{R,i-1/2}$

(iv) If x_i is outside the excision zone, but x_{i+1} is inside, set $u_{R,i+1/2} = u_{L,i+1/2}$

We also observed that the stability of our code close to the excision surface was strongly affected by the details of the interpolation method chosen for the communication from finite difference to spectral grid in that region. Previously, the interpolation stencil was shifted away from the excision boundary until the entire stencil was out of the excision zone. This could lead to unstable evolutions or large interpolation errors if the excision region happened to be located close to the boundary between two subdomains of the finite difference grid, and acceptable stencils could only be found far from the point we were interpolating to — or could not be found at all (to limit MPI communications, the stencil has

to be entirely contained in one subdomain). Currently, we limit the displacement of the stencil to a maximum of 3 grid point separations. If there is no good stencil within that distance, we decrease the order of the interpolation, and keep doing so until an acceptable stencil is found.

Another interpolation method would be to forbid any displacement of the stencil, and immediately drop to lower order as soon as part of the stencil lies within the excision zone. Both algorithms are equally robust, but when tested on an actual BHNS merger the first appeared to perform better at maintaining a smooth solution and low constraint violations on the excision surface. Accordingly, we chose it as our standard interpolation method and used it for all simulations presented in this paper.

Coordinate evolution

In the generalized harmonic formulation, the evolution of the inertial coordinates x_a is given by the inhomogeneous wave equation

$$\nabla^b \nabla_b x_a = H_a, \tag{4.11}$$

where ∇_b is the covariant derivative along x_b. The evolution of the function $H_a(x_b)$ can be freely specified, but its value on the initial slice $t = 0$ is determined by the initial data (the lapse and shift at $t = 0$ fix the initial evolution of the gauge). While the binary spirals in, we choose $\partial_t H_a(t, \tilde{x}_i) = 0$ in the coordinate frame $\tilde{x}_i$ comoving with the system. In our previous paper [28], we changed the gauge evolution during the merger phase by damping H_a exponentially in the comoving frame:

$$H_a(t, \tilde{x}_i) = e^{-(t-t_d)/\tau} H_a(t_d, \tilde{x}_i) \ , \tag{4.12}$$

where t_d is the disruption time—the time at which we begin damping— and τ is a damping timescale of order $10M$ (M being the total mass of the system). Further experimentation has shown that it is better not to change H_a near the excision zone. In our current simulations, we set

$$\frac{H_a(t,\tilde{x}_i)}{H_a(t_d,\tilde{x}_i)} = \left\{Q(\tilde{r}) + [1-Q(\tilde{r})]e^{-(t-t_d)/\tau}\right\} \quad (4.13)$$

$$Q(\tilde{r}) = e^{-(\tilde{r}/\tilde{r}_{\rm ex})^2+1} \quad (4.14)$$

during the merger phase, where $\tilde{r}$ is the distance to the center of the black hole in the comoving frame, and $\tilde{r}_{\rm ex}$ is the excision radius.

Evolutions with fixed metric

During the merger of a BHNS binary, both the spacetime metric and the fluid configuration are highly dynamical. Einstein's equations have to be solved together with the conservative hydrodynamics equations, and the evolution of that coupled system is computationally intensive. However, a few milliseconds after merger, the BH remnant settles into a quasistationary state as it accretes slowly from the surrounding accretion disk. Then, the evolution of the metric does not have a strong influence on the behavior of the system. In numerical simulations, we can thus extract some information on the long-term behavior of the final black hole-accretion disk system by neglecting the evolution of the metric and only evolving the fluid (c.f. [125]). Using this approximation, our code runs about 4 times faster.

To test the limitations of this method, we evolve the coupled system $\sim 1\mathrm{ms}$ past the time at which we begin the approximate, fluid-only evolution. We look for differences in the accretion rate or the characteristics of the disk (tempera-

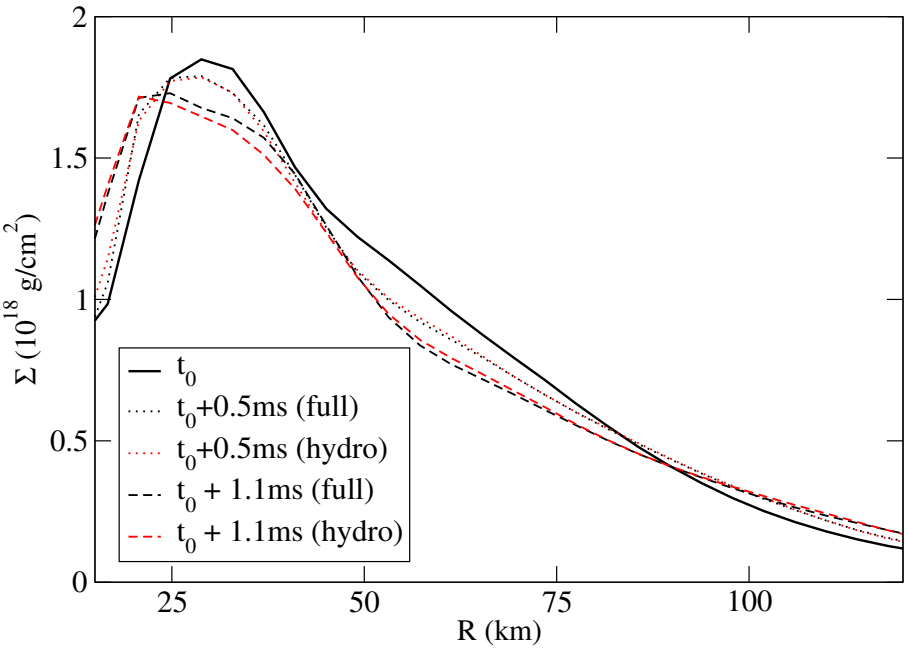

Figure 4.2: Average surface density of the fluid at a given distance from the center of mass of the system, for the simulation s.5i20 described in Sec. 4.4. The surface density is plotted at time $t_0 = t_{\rm merger} + 10.3{\rm ms}$, when we begin to evolve the system using the fixed-metric approximation, as well as 0.5ms and 1.1ms later. We see that the profile is very similar for both evolution methods, even though the disk itself is not in a stationary configuration.

ture, density, inclination) between the two methods used. As long as we wait for the properties of the black hole to settle down before switching to the approximate evolution scheme, the two methods show extremely good agreement — except for the highest spin configuration, which leads to a massive disk that cannot be evolved accurately by fixing the background metric. In Fig. 4.2 we show the evolution of the density profile of a disk using both the full GR evolution and the fixed-metric approximation. The evolution of the accretion disk is mostly unaffected by the change of evolution scheme.

4.3 Diagnostics

An indispensable test of numerical accuracy is convergence with grid resolution. We have evolved most of the cases discussed below at three resolutions. We call these Res1, Res2, and Res3; they correspond to 100^3, 120^3, and 140^3 grid-points, respectively, on the fluid grid and to 69^3, 82^3, and 95^3 collocation points on the pseudospectral grid.

The black hole is described by its irreducible mass $M_{\rm irr}$, its spin $\mathbf{S}_{\rm BH}$, and its Christodoulou mass $M_{\rm BH} = \sqrt{M_{\rm irr}^2 + {S_{\rm BH}}^2/(4M_{\rm irr}^2)}$. The spin $\mathbf{S}_{\rm BH}$ is computed using the approximate Killing vector method [71].

To monitor the nuclear matter, we first measure the baryonic mass $M_{\rm b}$ on the grid as a function of time. Initially, this will be the baryonic mass of the neutron star. After the tidal destruction of the star, it will be the sum of the accretion disk and the tidal tail masses. At late times (more than 10ms after merger), it will be the baryonic mass of the disk. The accretion timescale $\tau_{\rm disk}$ is $M_{\rm b}/(dM_{\rm b}/dt)$.

We also analyze the heating in the disk. This is done through both an entropy and a temperature variable. When evolving with microphysical equations of state, the temperature and entropy are provided directly. For this study, we use a Γ-law equation of state, so we need a way to estimate the entropy and temperature. The entropy measure s we define as $s = \log(\kappa/\kappa_i)$, where κ is the polytropic constant obtained from the relation between the pressure and the baryon density ($P = \kappa\rho_0^\Gamma$), and κ_i is its initial, cold value. To estimate the physical temperature, T, we assume that the thermal contribution to the specific internal energy $\epsilon_{\rm th} = \epsilon - \epsilon(T = 0)$ is given by a sum of ideal gas and blackbody

components:

$$\epsilon_{\rm th} = \frac{3kT}{2m_n} + f\frac{aT^4}{\rho}\ , \tag{4.15}$$

where m_n is the nucleon mass, and the factor f reflects the number of relativistic particles, and is itself a function of T. (See [119, 33], who also make this assumption.) For the most part, we will report density-averaged values of s and T. For example, the density-averaged entropy is

$$\langle s \rangle = \frac{\int \rho(\mathbf{r}) s(\mathbf{r}) dV}{\int \rho(\mathbf{r}) dV}. \tag{4.16}$$

To launch a GRB, a baryon-clean region above the disk is probably needed. This does not mean that a wider clean region is always better, since a thick disk can help collimate the outflowing jet — but we want to determine whether such a region exists or not. To estimate the baryon-poor opening above our disks, we define the opening angle $\theta_{\rm clean}$. This angle specifies the widest cone oriented along the BH spin in which the condition $\rho \leq \rho_{\rm cut}$ is everywhere satisfied: if $\theta_{\rm clean}(r, \phi)$ is the opening angle within which we have $\rho \leq \rho_{\rm cut}$ at radius r and azimuthal coordinate ϕ, then $\theta_{\rm clean} = \min_{r,\phi} [\theta_{\rm clean}(r, \phi)]$. In these simulations, the numerical method requires atmospheric corrections to be applied starting at $\rho = 6 \times 10^8 {\rm g/cm^3}$, so that it is impossible to reliably predict the behavior of matter below that threshold. Therefore, we set $\rho_{\rm cut} = 3 \times 10^9 {\rm g/cm^3}$.

For precessing binaries we also compute the tilt β and twist γ of the disk, as defined by Fragile & Anninos [41]. If x^μ are the inertial coordinates, $T^{\mu\nu}$ the stress-energy tensor, $\epsilon_{\mu\nu\sigma i}$ the Levi-Cevita tensor (with its last index limited to nonzero values), $\boldsymbol{J}_{\rm BH}$ the angular momentum of the BH and $\hat{e}_y$ an arbitrary unit vector orthogonal to $\boldsymbol{J}_{\rm BH}$, then β, γ and the disk angular momentum $\boldsymbol{J}_{\rm disk}$ are

given by

$$L^{\mu\nu} = \int \left(x^\mu T^{\nu 0} - x^\nu T^{\mu 0}\right) d^3x \tag{4.17}$$

$$S^\mu = \int T^{\mu 0} d^3x \tag{4.18}$$

$$J_{\mathrm{disk},i} = \frac{\epsilon_{\mu\nu\sigma i} L^{\mu\nu} S^\sigma}{2\sqrt{-S^\alpha S_\alpha}} \tag{4.19}$$

$$\beta(r) = \arccos\left[\frac{\boldsymbol{J}_{\mathrm{BH}}.\boldsymbol{J}_{\mathrm{disk(r)}}}{|\boldsymbol{J}_{\mathrm{BH}}||\boldsymbol{J}_{\mathrm{disk(r)}}|}\right] \tag{4.20}$$

$$\gamma(r) = \arccos\left[\frac{\boldsymbol{J}_{\mathrm{BH}} \times \boldsymbol{J}_{\mathrm{disk(r)}}}{|\boldsymbol{J}_{\mathrm{BH}} \times \boldsymbol{J}_{\mathrm{disk(r)}}|}.\hat{e}_y\right]. \tag{4.21}$$

These parameters determine the inclination and the precession of the disk with respect to the spin of the black hole: if $\mathbf{J}_{\mathrm{BH}} = J_{\mathrm{BH}}\hat{e}_z$, then the orbital angular momentum of the disk at radius r is written as

$$\mathbf{J}_{\mathrm{disk}}(r) = J_{\mathrm{disk}}(r)\left(\sin\beta\cos\gamma\hat{e}_x + \sin\beta\sin\gamma\hat{e}_y + \cos\beta\hat{e}_z\right). \tag{4.22}$$

Another useful property of the disk is its scale height, H. For a disk with exponentially decreasing density, H is defined by $\rho = \rho_c e^{-z/H}$. Here, however, the vertical profile of the disk is significantly more complex, and various definitions of H could be considered. We use the spread of the density distribution $\rho(\theta, \phi)$ on a sphere of constant radius r with its polar axis along $\mathbf{J}_{\mathrm{disk}}(r)$ and define

$$H(r) = r\tan^{-1}\left(\sqrt{\mu\frac{\int \rho(\mathbf{r})[\theta(\mathbf{r})]^2\, dS}{\int \rho(\mathbf{r})\, dS}}\right). \tag{4.23}$$

The parameter μ is somewhat arbitrary. For an exponential profile $\mu \sim 0.5$, while for a constant density profile ($\rho = \rho_0$ for $\theta < H/r$ and $\rho = 0$ otherwise) we have $\mu \sim 3$. The disks observed in our simulations are somewhat in between these two extremes. Accordingly, we make the approximate choice $\mu = 1$.

To measure the accuracy of our simulations, we monitor the ADM Hamiltonian and momentum constraints, and the generalized harmonic constraints

$\|\mathcal{C}\|$ [68]. At our middle resolution, $\|\mathcal{C}\|$ peaks below 1% for all cases and is less than 0.1% during most of the inspiral. We also monitor the ADM mass $M_{\rm ADM}$ and angular momentum $\mathbf{J}_{\rm ADM}$. An important check of our simulations is that the changes in these quantities match the flux of energy and angular momentum in the outgoing gravitational radiation, which we reconstruct from the Newman-Penrose scalar ψ_4 as in Ref. [16].

4.4 Cases

In order to assess the influence of the black hole spin on the disruption and merger of BHNS binaries, we study configurations for which all other physical parameters are held constant. The mass of the black hole is $M_{\rm BH} = 3M_{\rm NS}$, where $M_{\rm NS}$ is the ADM mass of an isolated neutron star with the same baryon mass as the star under consideration, and the initial coordinate separation is $d = 7.5M$, with $M = M_{\rm BH} + M_{\rm NS}$. For the nuclear equation of state, we use the polytrope

$$P = (\Gamma - 1)\rho\epsilon = \kappa\rho^{\Gamma} + \overline{T}\rho \tag{4.24}$$

where $\overline{T}$ is a fluid variable related to, but not equal to, the physical temperature. We set $\Gamma = 2$ and choose κ so that the compaction of the star is $C = M_{\rm NS}/R_{\rm NS} = 0.144$. For polytropic equations of state, the total mass of the system does not have to be fixed: results can easily be rescaled by M (see e.g. Sec. II-F of Foucart *et al.* [40]). However, whenever we choose to interpret our results in physical units (ms, km, $M_\odot$), we will assume that $M_{\rm NS} = 1.4M_\odot$ ($M = 5.6M_\odot$). For that choice, the neutron star has a radius $R_{\rm NS} = 14.6{\rm km}$, and the initial separation is $d = 63{\rm km}$.

The different initial configurations and black hole spins studied are summa-

rized in Table 4.1. We consider 3 different magnitudes of the dimensionless spin $a_{\rm BH}/M_{\rm BH} = (0, 0.5, 0.9)$, all aligned with the orbital angular momentum. Then, we vary the inclination angle $\phi_{\rm BH}$ between the spin of the black hole and the initial angular velocity of the system, $\mathbf{\Omega}^{\rm rot}$. Considering that most BHNS binary systems are expected to have $\phi_{\rm BH} \leq 90^\circ$ (Belczynski et al. [12]), with about half of the binaries at $\phi_{\rm BH} \leq 40^\circ$, we choose $\phi_{\rm BH} = (20^\circ, 40^\circ, 60^\circ, 80^\circ)$. The orientation of the component of the BH spin lying in the orbital plane could also have measurable consequences. For example, Campanelli *et al.* [19] showed that the superkick configuration found in binary black hole systems is sensitive to the direction of the misaligned component of the BH spin. For BHNS binaries, kicks are relatively small, and we are more interested in the characteristics of the final black hole-disk system. After looking at different orientations for $\phi_{\rm BH} = 80^\circ$, we find that the influence of the orientation of the misaligned component of the BH spin is negligible compared to the influence of $\phi_{\rm BH}$. For this first study of misaligned spins, we will thus limit ourselves to configurations for which the initial spin lies in the plane generated by the initial orbital angular momentum and the line connecting the two compact objects. As the different initial configurations do not use the same background metric, there is no guarantee that two binaries with the same initial coordinate separation can be directly compared. A better comparison between initial configurations is the orbital angular velocity of the system. In Table 4.1, we show that all configurations have initial angular velocity within 1% of each other. This is the level of error that we expect from the quasiequilibrium method for binaries at this separation.

Case	$a_{\rm BH}/M_{\rm BH}$	$\phi_{\rm BH}$	$\Omega_{\rm init}M$	$E_b/M_{\rm ADM}$	$J_{\rm ADM}/{M_{\rm ADM}}^2$	$t_{\rm merger}$
s0	0	-	4.16e-2	9.5e-3	0.66	7.5ms
s.5i0	0.5	0	4.11e-2	1.01e-2	0.91	11.4ms
s.9i0	0.9	0	4.13e-2	9.6e-3	1.13	15.0ms
s.5i20	0.5	20	4.09e-2	1.01e-2	0.90	10.5ms
s.5i40	0.5	40	4.10e-2	1.01e-2	0.87	9.9ms
s.5i60	0.5	60	4.11e-2	9.9e-3	0.82	9.0ms
s.5i80	0.5	80	4.13e-2	9.6e-3	0.76	7.7ms

Table 4.1: Description of the cases evolved. $a_{\rm BH}/M_{\rm BH}$ is the initial dimensionless spin of the BH, $\phi_{\rm BH}$ is its inclination with respect to the initial orbital angular momentum and E_b is the initial binding energy. $t_{\rm merger}$ is defined as the time by which half of the matter has been accreted by the BH. Differences in the initial angular velocity and binding energy are within the margin of error of the initial data: at this separation the eccentricity reduction method can require variations of $\Omega_{\rm init}$ of order 1%, and modifies the binding energy by a few percent.

4.5 The nonspinning case: a test of our accuracy

As an example, we consider the case s0, in which the BH is initially nonspinning. We evolve this case at each of our three resolutions. After a short (two orbits) inspiral, the neutron star is disrupted, and most of the matter is quickly swallowed by the black hole. The remainder expands into a tidal tail and then falls back to form an accretion disk.

Nearly identical systems have been studied both by Shibata *et al* [117] and by Etienne *et al* [33]. The former found an insignificant disk after merger, while the latter found 4% of the NS mass still outside the hole $300M$ ($\sim 8{\rm ms}$) after merger. Both groups found a final BH spin of $s = 0.56$. We find a disk mass of 3.7% at $300M$ after merger, smaller than in [33], but closer to this result than to that in [117]. Our final BH spin is 0.56, in agreement with both previous studies.

In Fig. 4.3, we show the evolution of M_b and $\langle s \rangle$ for the entire merger phase for the three resolutions. Reassuringly, the different resolutions give very similar results, with the two higher resolutions being closest together. The baryonic mass is initially constant before accretion starts. Then, as the NS is disrupted and the core of the star is swallowed, M_b drops rapidly. It next levels off while the remaining matter is in an accretion disk and an expanding tidal tail. When the tidal tail falls back onto the disk, there is a second phase of rapid accretion, after which the accretion rate settles down to a low value. At the end of the simulation, the accretion timescale is $\tau_{\rm disk} \sim 55{\rm ms}$, implying that the total lifetime of the disk would be around 75ms. At late times, the deviation in M_b between resolutions becomes somewhat larger, indicating that our errors have accumulated to about 0.1% of the initial mass. For the purposes of this paper, this is adequate, since the disk on these timescales is affected by magnetic and radiation processes not included in the simulations. However, future long-term disk simulations will require higher accuracy.

As for the entropy, at the beginning of the merger it only deviates from zero because of numerical heating during the inspiral. As expected, this numerical heating is significantly lower at higher resolutions. The post-merger heating is not numerical, but a physical consequence of shocks in the disk and the disk-tail interface. A confirmation that the heating is physical is that it is nearly the same for all resolutions, and its magnitude is much larger than the numerical heating. When the disk settles, there is no further shock heating, so the entropy levels off. This indicates that the heating due to numerical viscosity is small compared to shock heating. Unfortunately, this is not the same as saying that the numerical viscosity is irrelevant altogether. However, the closeness of $\tau_{\rm disk}$ at each resolution indicates that this viscosity is not the main driving force of the

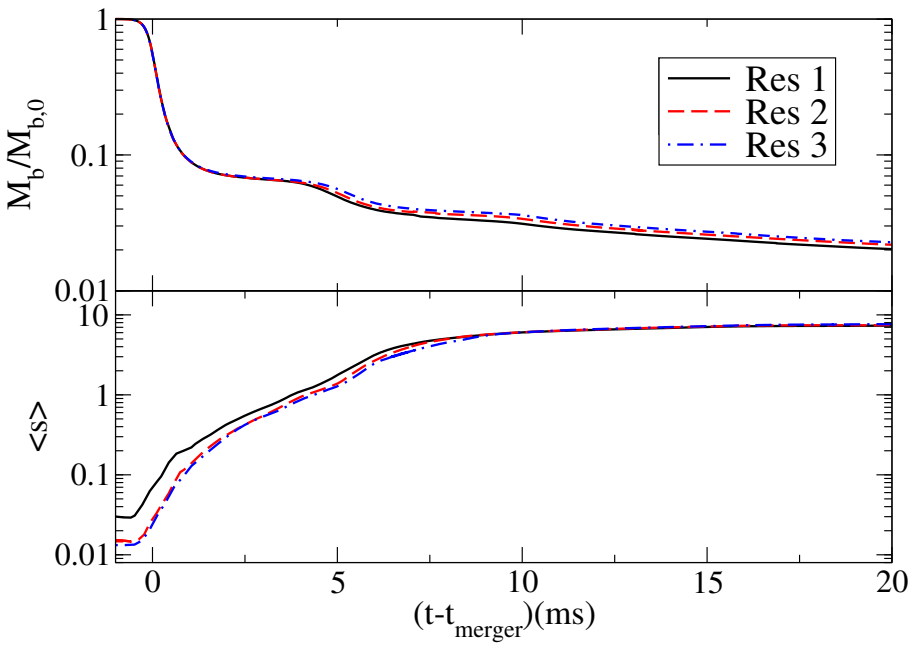

Figure 4.3: Baryonic mass M_b normalized by its initial value $M_{b,0}$ and average entropy $\langle s \rangle$ for three resolutions.

accretion. The average temperature $\langle T \rangle$ behaves in a way similar to the entropy. Starting from low values, it increases after the merger and stabilizes around 3MeV. All resolutions show the same $\langle T \rangle$ growth, and all level off at the same value. After leveling off, though, $\langle T \rangle$ displays 0.1MeV oscillations that do not converge well, another indication that our accuracy is sufficient for some but not all purposes.

In Fig. 4.4, we plot the ADM energy and orbital-axis angular momentum measured on a surface $75M$ from the center of mass of the system. Also plotted is the evolution of these quantities expected from the gravitational radiation through this surface. Overall, the agreement is quite good, although there is some deviation in $M_{\rm ADM}$ a while after the merger. This seems to be associated with an increase in constraint violations at the merger time. The relative constraint violations, as measured by $\|\mathcal{C}\|$, peak slightly below 1% at the middle

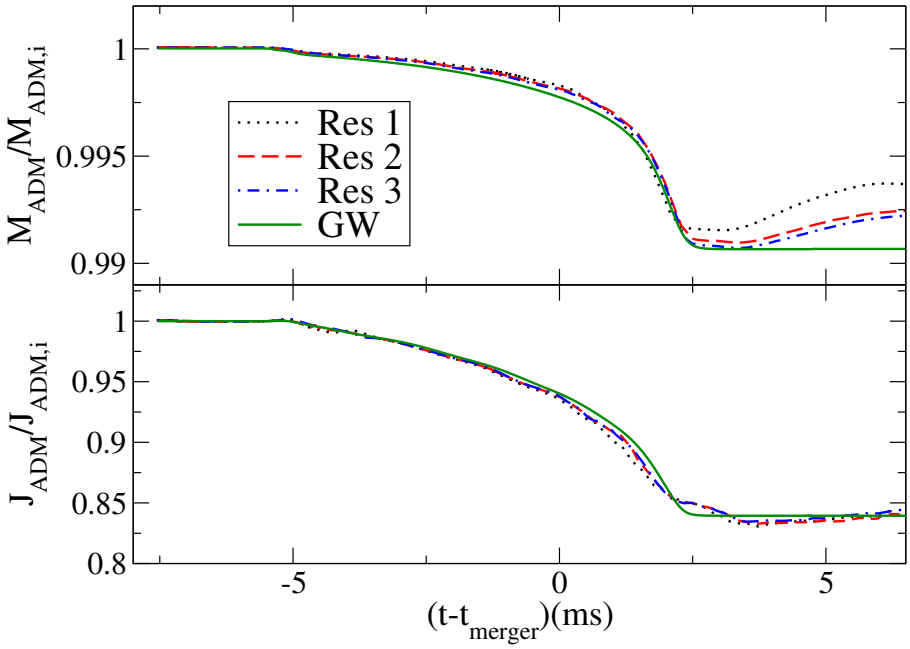

Figure 4.4: $M_{\rm ADM}$ and $J_{\rm ADM}$ (normalized to their initial values) compared to the changes expected from the gravitational radiation flux for three resolutions.

resolution. The corresponding values for the ADM constraints are 1 –2 %, before both constraints fall back to low values. The deviations in $M_{\rm ADM}$ happen around the time this constraint-violating pulse reaches the $r = 75M$ surface.

We have checked several other quantities, including the black hole mass and spin and the gravitational waveform. All of these show very good convergence.

4.6 Results

The general behavior of our simulations is typical of BHNS binaries for which the NS is disrupted outside the innermost stable circular orbit of the BH. From an initial separation of $60{\rm km}$, the compact objects go through 2-3 orbits of inspiral driven by the emission of gravitational waves. When the distance between

them has been reduced to about $30 - 40\mathrm{km}$, tidal forces cause the neutron star to disrupt. Most of the matter is rapidly accreted into the black hole, while the rest is divided between a long tidal tail, expanding about $200\mathrm{km}$ away from the black hole, and a developing accretion disk. The duration of the inspiral varies with the spin of the BH, with the component of the BH spin along the orbital angular momentum delaying the merger. The merger time t_{merger}, which we define as the time at which 50% of the matter has been accreted onto the BH, is listed for all cases in Table 4.1.

The resulting accretion disk is highly asymmetric, and evolves in time. When the disk first forms, around 5ms after merger, it creates a torus of matter with its peak surface density (baryon density integrated over the height of the disk) at $r(\Sigma_{\mathrm{max}}) \sim 30\mathrm{km}$ and a temperature $T \sim 1 - 2\mathrm{MeV}$. Then, as matter accretes from the tidal tail and shocks heat the fluid, the disk expands quickly. About $10 - 20\mathrm{ms}$ after merger, the disk starts to settle into a stable, slowly accreting state. To compare the different configurations studied here, we look at the properties of this late-time stable configuration, listed in Table 4.2. In Table 4.3, we give the characteristics of the final black hole, as well as the kick velocity, the energy content of the emitted gravitational waves, and the peak amplitude of a dominant (2,2) mode of the waves. [The (2,2) and (2,-2) are the strongest modes, with nearly equal amplitude. See Section 4.6.2 on the higher modes.]

4.6.1 Effects of spin magnitude

To test the effects of BH spin magnitude, we compare our results for s0, s.5i0, and s.9i0. A comparison of this type has already been performed by Etienne *et*

Case	$M_{\rm disk}/M_{\rm NS}$	$\langle T\rangle_{\rm disk}$	$\beta(\Sigma_{\rm max})$	$r(\Sigma_{\rm max})$	$\theta_{\rm clean}$	$\frac{H}{r}(\Sigma_{\rm max})$
s0	5.2%	3.0MeV	0°	50km	50°	0.20
s.5i0	15.5%	3.5MeV	0°	50km	35°	0.25
s.9i0	38.9%	5.6 MeV	0°	20km	8°	0.18
s.5i20	14.5%	3.6MeV	2°	50km	40°	0.20
s.5i40	11.5%	3.8 MeV	4°	50km	30°	0.22
s.5i60	8.0%	3.7MeV	7°	50km	40°	0.20
s.5i80	6.1%	3.6MeV	8°	50km	50°	0.25

Table 4.2: Properties of the accretion tori at late time. The mass of the disk $M_{\rm disk}$ (baryon mass outside the excision region), which decreases continuously due to accretion onto the BH, is measured at $t_{\rm merger}+5{\rm ms}$. Even at late times, all quantities still show oscillations of $\sim 10\%$.

Case	$M_{\rm BH}/M$	$a_{\rm BH}/M_{\rm BH}$	$v_{\rm kick}({\rm km/s})$	$E_{\rm GW}/M$	$rM\Psi_4^{2,2}$
s0	0.97	0.56	53	0.98%	0.020
s.5i0	0.94	0.77	60	0.92%	0.012
s.9i0	0.89	0.93	52	0.95%	0.009
s.5i20	0.95	0.76	60	0.89%	0.012
s.5i40	0.96	0.74	61	0.91%	0.013
s.5i60	0.96	0.71	54	0.95%	0.014
s.5i80	0.97	0.66	67	0.95%	0.017

Table 4.3: Properties of the post-merger black hole and gravitational waves.

al [33]. Our cases are different, though: unlike them, we do not consider an antialigned case, but we do push the BH spin to a slightly higher level in our run s.9i0.

Run s.9i0 presented special numerical challenges. In SPEC, the singularity and inner horizon of the BH have to be excised from the numerical grid while the apparent horizon must remain outside the excision surface. But for nearly extremal black holes the region between the inner horizon and the apparent horizon becomes very narrow. To perform excision in such cases, the excision boundary must nearly conform to the apparent horizon. We do this by intro-

ducing a coordinate map in the initial data so that the horizon is initially spherical on the pseudospectral grid. We then use our dual frame coordinate-control method [108] to fix the location of the horizon throughout the whole simulation. For lower spins this is not necessary, and we only begin to control the horizon location at the time of neutron star disruption. That modification excepted, case s.9i0 was simulated in exactly the same way as the other cases. The deviation between the results at resolutions Res2 and Res3 is somewhat larger than in the other cases (though still quite small). To be more exact, the relative deviation in the disk mass between Lev2 and Lev3 is about 9% ($\sim$3% of the NS mass) for s.9i0 while it was about 5% for s0, and the deviation in merger time is about 4% for s.9i0 but only 0.3% for s0. The difference indicates that high resolution is needed when studying such extreme cases.

We find that systems with higher $a_{\rm BH}/M_{\rm BH}$ spiral in more slowly: from the same initial separation, s0, s.5i0, and s.9i0 take roughly 2, 3, and 3.7 orbits, respectively, before NS disruption begins. This effect exists in the post-Newtonian treatment [54] and it has already been seen both in binary black hole (e.g. [18]) and BHNS [33] simulations. Because of the prolonged inspiral for the high-spin cases, more angular momentum is radiated: $0.11M^2$ for s0 vs $0.14M^2$ for s.9i0. Additionally, as the BH becomes nearly extremal, increasing the spin becomes more and more difficult. This is reflected in the final spin of the BH: while $a_{\rm BH}/M_{\rm BH}$ increases from 0 to 0.56 for s0, it only increases from 0.9 to 0.93 for s.9i0.

We also confirm that the post-merger accretion disk mass increases significantly as the magnitude of the aligned BH spin is increased, as shown in Fig. 4.5. This is in qualitative agreement with Etienne *et al*. About $400M$(11ms) after

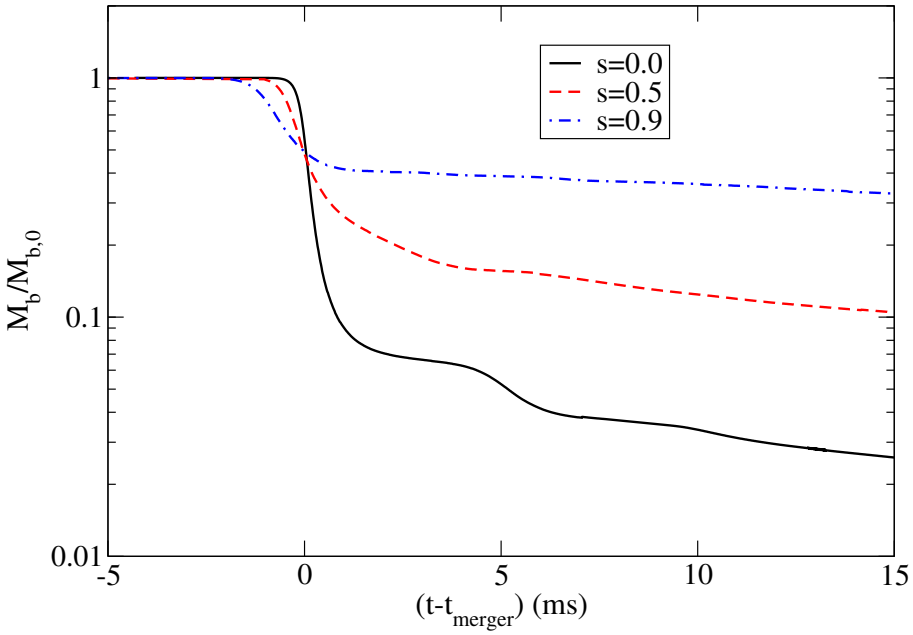

Figure 4.5: Evolution of the total baryonic density outside the hole for three different aligned BH spins.

merger they find $M_b/M_{b,i} \sim 20\%$ for an $a_{\rm BH}/M_{\rm BH} = 0.75$ system, while for our $a_{\rm BH}/M_{\rm BH} = 0.9$ system, we find $M_b/M_{b,i}$ ~35% at a similar time.

4.6.2 Effects of spin orientation

Most BHNS binaries are expected to have at least a moderate misalignment between the spin of the BH and the total angular momentum [12], and this should affect all stages of the binary evolution.

During inspiral, the orbital angular momentum and the BH spin precess around the total angular momentum of the system. The evolution of the coordinate components of the BH spin for the s.5i80 case is shown in Fig. 4.6. Over the two orbits of inspiral, the spin goes through about a quarter of a precession period. The qualitative evolution of the spin is well described by post-Newtonian

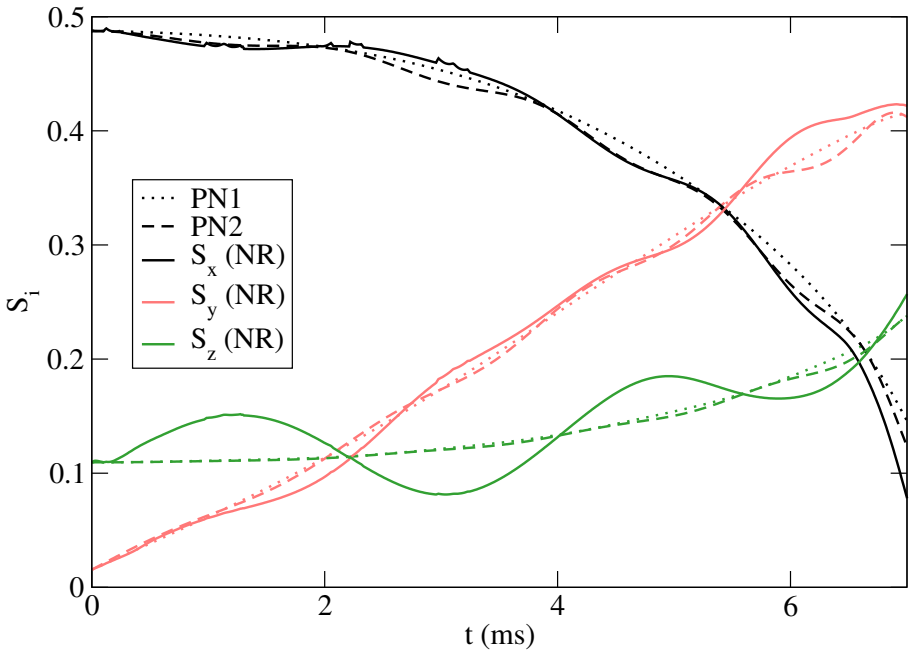

Figure 4.6: Comparison of the evolution of the Cartesian components of the spin for an initial inclination of $80°$ in our simulation (NR) and for the first- and second-order Post-Newtonian expansions (resp. 1PN and 2PN). The PN values are obtained by integrating the evolution equations for the spin given in [37], using the trajectory and current spin of the numerical simulation.

corrections (see e.g. [37]), even though our simulation uses a different gauge choice. As for aligned spin, the infall velocity varies between cases: the larger the component of the spin aligned with the angular momentum, the slower the inspiral. Not too surprisingly, we find a monotonic decrease of the merger time with increasing misalignment angle $\phi_{\rm BH}$, with $t_{\rm merger}(\phi_{\rm BH}, a_{\rm BH}) \to t_{\rm merger}(0,0)$ for $\phi_{\rm BH} \to 90°$.

The disruption of the star and formation of a disk, shown in Fig. 4.7, proceed somewhat differently from what is observed for nonprecessing binaries. As before, the disruption of the star is accompanied by the formation of a long tidal tail. But because of the inclination of the BH spin, the orbital plane of the

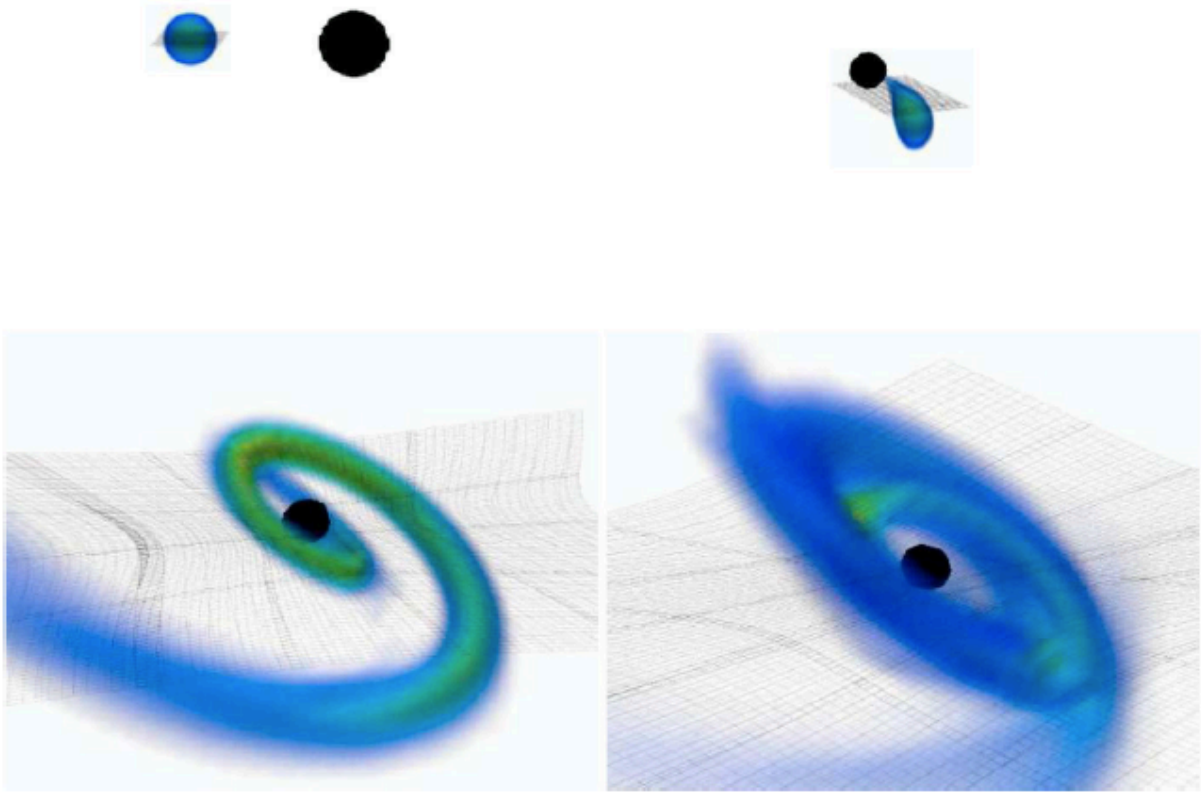

Figure 4.7: Evolution of an inclined binary (s.5i80). *Top left:* Beginning of the simulation, at a separation of 63km. *Top right:* After 7ms and two orbits of inspiral, the star disrupts and most of the matter rapidly accretes onto the black hole. *Bottom left:* After 11ms, the remaining matter ($\sim 8.5\%$ of the initial mass) is split between a developing disk and a tidal tail. Differential precession between the disk and the tail means that the disk and the matter falling back from the tail orbit in different planes. *Bottom right:* After 15.5ms, the disk contains about 4.5% of the initial mass of the star. It is still highly inhomogeneous, and slowly expanding. A movie of the whole simulation is available online [1]. In each image, the wired frame shows the "fluid" grid in the $z = 0$ plane (orbital plane at $t = 0$).

fluid continues to precess after disruption. Because the precession rate varies with the distance to the hole, the tail and the disk do not remain in the same plane. While for nonprecessing binaries matter from the tail falls back within the orbital plane of the disk, here matter is added to the disk at an angle varying in time. This significantly modifies the nature of the tail-disk interactions. At small inclination angles ($\phi \sim 20 - 40^\circ$), we have a direct collision between the developing disk and the tidal tail, while for larger inclinations the disk is initially formed of layers of high-density material at different angles with respect to the black hole spin.

The mass of the disk, plotted in Fig. 4.8, decreases as the inclination of the binary increases. The transition between low and high mass disks is continuous, but more rapid at large inclinations: for $\phi_{\rm BH} < 40^\circ$, $10 - 15\%$ of the initial mass of the star ($\sim 0.15 - 0.2 M_\odot$) remains either in the tail or in the disk 5ms after merger. This is roughly similar to the disk formed for $\phi_{\rm BH} = 0$. At higher inclinations, the size of the disk drops sharply, to about 5% of the initial mass of the star. We expect the disk mass to be even lower for antialigned spins ($\phi_{\rm BH} > 90^\circ$), though such configurations appear less likely to be found in astrophysical systems. These changes in the disk mass with the orientation of the BH spin show some similarities with the results of Rantsiou *et al.* [99], obtained in the small mass-ratio limit ($q = 1/10$) by using a static background metric. They found that for a disk to be formed, the condition $\phi_{\rm BH} < 60^\circ$ has to be satisfied. As our simulations use a mass ratio $q = 1/3$, which is more favorable to the formation of a disk, it is not too surprising that even high inclinations leave us with a significant disk; however, the influence of inclination remains important for $\phi_{\rm BH} > 40^\circ$. These factors are particularly useful when considering the potential of the final remnant to be a short gamma-ray burst progenitor. Since the influ-

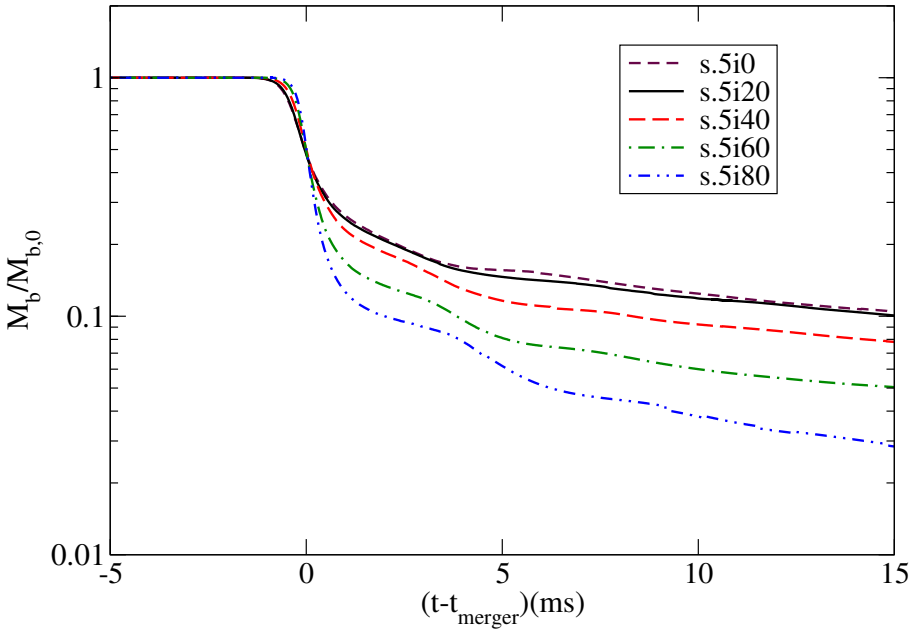

Figure 4.8: Evolution of the total baryonic mass outside the hole for different initial inclination of the BH spin.

ence of a misaligned BH spin is only felt for $\phi_{\rm BH} > 40°$, the majority of BHNS binaries can form disks about as massive as is predicted by simulations that do not take into account the inclination of the BH spin.

The gravitational wave signal is also significantly affected by the value of $\phi_{\rm BH}$. We expand the Newman-Penrose scalar Ψ_4 extracted at $R = 75M$ using the spin-weighted spherical harmonics ${}_{-2}Y_{lm}$ and choosing the polar axis along the initial orbital angular momentum of the binary. The peak amplitude of the dominant (2,2) mode of Ψ_4 will increase for large inclinations, as could be expected from the results obtained for aligned spins; here too, a large component of the spin along the orbital angular momentum works against large Ψ_4 amplitudes. Additionally, the contribution of subdominant modes can become significant at large inclinations. In Fig. 4.9, we show the ratio of the amplitude of the scalar $\Psi_{4(l,m)}$ to the amplitude of the (2,2) mode for various (l, m) modes

and for $\phi_{\rm BH} = 20^\circ, 60^\circ$. The modes most strongly affected by the precession of the binary are the (2,1) and (3,2) modes, the first reaching half the amplitude of the dominant mode around merger for the s.5i60 simulation. Analytical predictions for the effect of a precessing trajectory on the modal decomposition of the gravitational wave signal have been derived by Arun *et al.* [6]. We find qualitative agreement with their results if we assume that the compact objects follow the trajectories obtained from our numerical simulations. In particular, we note that for precessing binaries, the frequency of the (2,1) mode is closer to $2\Omega_{\rm rot}$ than to $\Omega_{\rm rot}$. The (2,1) and (2,2) modes have similar frequencies, so that the ratio of their amplitude computed using the scalar Ψ_4 is close to the result one would obtain by using the gravitational strain h instead. This will not be true for the (3,3) mode, which has a frequency $\Omega_{(3,3)} \sim 3\Omega_{\rm rot}$: since $\Psi_4 = \partial^2 h/\partial t^2$, we have $h_{(3,3)}/h_{(2,2)} \sim (4/9)\Psi_{4(3,3)}/\Psi_{4(2,2)}$.

In Fig. 4.10, we plot the gravitational strain h as observed from a distance of $100\,{\rm Mpc}$ for the simulations s.5i0 and s.5i80. The three waveforms correspond to observation points whose lines of sight are inclined by 0°, 30° and 60° with respect to the initial orbital angular momentum of the system. Over the short inspiral considered here, the effects of precession are relatively small. The main difference visible in these waveforms is the slower inspiral experienced by the binary with aligned spin. We can also note that in the misaligned configuration the star does not disrupt as strongly as in the aligned case, causing the cutoff of the wave emission to occur at a later time. As a consequence, the cutoff frequency of the wave is larger for misaligned spins than for aligned spins. This explains why the amplitude of the gravitational strain h is comparable for both configurations, while the misaligned case showed a significantly larger amplitude when the wave was measured using the scalar Ψ_4 (a similar effect occurs

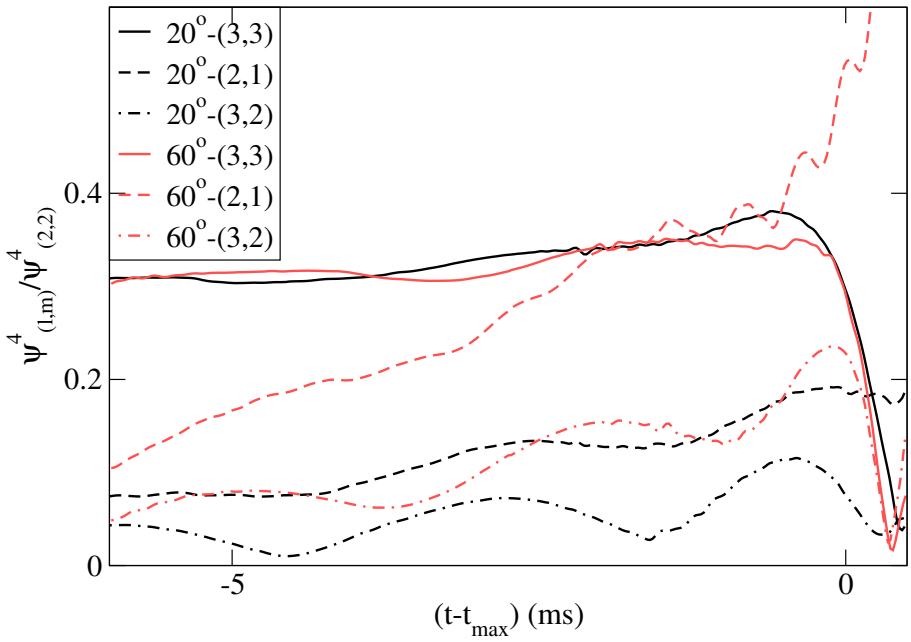

Figure 4.9: Amplitude of $\psi^4_{(l,m)}/\psi^4_{(2,2)}$ for the 3 modes (2,1), (3,3) and (3,2), shown for initial inclinations of the BH spin of 20° and 60°. The time $t_{\rm max}$ corresponds to the peak amplitude of the dominant (2,2) mode.

if both spins are aligned but of different magnitudes). Finally, the precession of the orbit causes the gravitational wave emission of the misaligned configuration to peak at a non-zero inclination with respect to the initial orbital angular momentum. Here, at the time of merger the wave measured at an inclination of 30° is slightly larger than at 0°. For these effects to be more visible, and in particular for a full precession period to be observable, longer simulations are required (~ 10 orbits).

4.6.3 Post-merger accretion disks

The evolution of the accretion disk over timescales comparable to its expected lifetime is likely to be significantly influenced by physical effects that are not

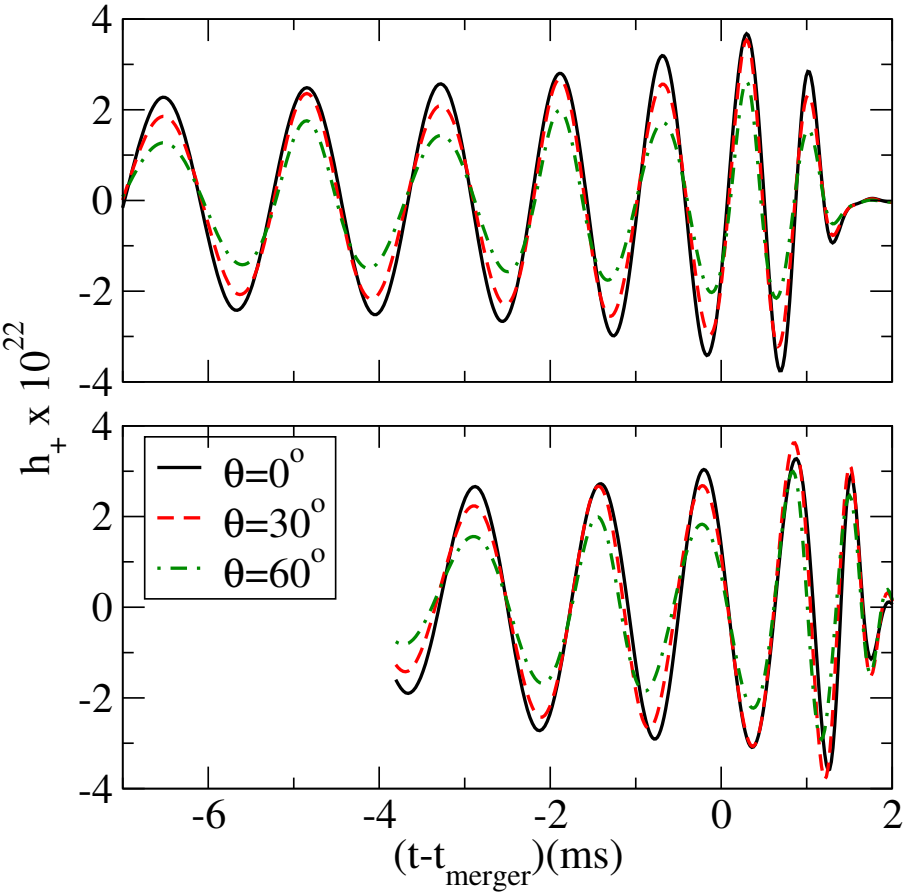

Figure 4.10: Real part of the gravitational strain h for the simulations s.5i0 (*top panel*) and s.5i80 (*lower panel*), viewed from different inclinations θ with respect to the initial orbital angular momentum. The wave is extracted at $r = 75M$ for a mass of the neutron star $M_{\rm NS} = 1.4M_\odot$, and assumed to travel as a linear perturbation up to the observation point located at $r = 100\,{\rm Mpc}$. Waves emitted at the time of merger will reach the radius $r = 75M$ at $(t - t_{\rm merger}) \sim 2{\rm ms}$. Over the 2 – 3 orbits simulated here, the effects of the orbital precession—and, in particular, the contribution on the second highest mode (2,1), shown in Fig. 4.9—remain small.

taken into account in our simulations, mostly the magnetic effects and the impact of neutrino cooling. We do not expect the results of our simulations to accurately represent the details of the late-time evolution of the disk, but we can nonetheless extract some information regarding the general characteristics of the final remnant. To obtain these approximate results, which are summarized in Table 4.2, we use the fixed-metric approximation described in Sec. 4.2.2, starting $5 - 10\mathrm{ms}$ after merger. At that time, the disk is still expanding, and will typically settle down to a more stable quasiequilibrium profile with a relatively low accretion rate over about $10\mathrm{ms}$.

The coordinate distance between the peak surface density of the disk (averaged over all points at a given coordinate radius) and the center of the BH shows no strong or monotonic dependence on the BH spin. After the initial expansion of the disk, variations in the details of the interactions between the tidal tail and the accretion disk can lead to different evolutions of the density profile. On average, the disks tend to expand slightly, while their density decreases because of continued accretion onto the black hole. However, neither the tidal tail nor the disk are homogeneous, so that the evolution of the density profile shows significant oscillations around that average behavior. The accretion rate is larger for the more massive disks, so that the expected lifetime of the disk is of the same order of magnitude for a nonspinning BH ($\tau \sim 75\mathrm{ms}$) as for the highly spinning BH ($\tau \sim 150\mathrm{ms}$).

The thermal evolution of the disk does not vary much between configurations. The temperature $\langle T \rangle_{\mathrm{disk}}$ rises rapidly during the formation of the disk, then stabilizes at about 3.5MeV in each case — although the average entropy $\langle s \rangle_{\mathrm{disk}}$ is about 10% lower for spinning black holes than for s0. For most config-

urations, the temperature then remains relatively stable for the rest of the evolution, with oscillations of order 10%. The highest spin configuration s.9, however, reaches significantly higher temperatures, with $T \sim 5MeV$. Fig. 4.11 shows the entropy and specific angular momentum profile of three of our disks at the end of the simulation. At the final time, each of the disks shows an inverted entropy gradient in the inner region between the black hole and the radius of maximum surface density. The entropy difference between the inner edge of the disk and the density maximum is about 10%. However, the disk is at least partially stabilized by the strong shear in the rotational velocity in these inner regions.

In Fig. 4.12, we show two snapshots of the disk profile for the s.5i60 simulation at, respectively, 20ms and 40ms after merger. As the disk keeps accreting, the surface density decreases but the profile is otherwise mostly constant. The small inverted entropy gradient and the strong positive specific angular momentum gradient of the inner disk are visible, while outside the radius of maximum density the entropy profile is mostly constant and the specific angular momentum increases more slowly until $r \approx 100 - 150$km. Beyond this radius, matter is still in the remnant tidal tail rather than the settled disk. The time evolution of these two quantities is extremely small, the only difference being a smoother profile at late times. The disk is relatively thick, with $H/r \sim 0.2$ at all radii within the disk, a value that remains constant from a few milliseconds after merger to the end of the simulation.

For inclined disks, we also measure the tilt β and twist γ of the disk, as defined by Eq. (4.22). For large inclinations (s.5i60 and s.5i80), the tilt angle between the disk angular momentum and the orientation of the BH spin varies slowly during the evolution of the disk, at least in the higher density regions.

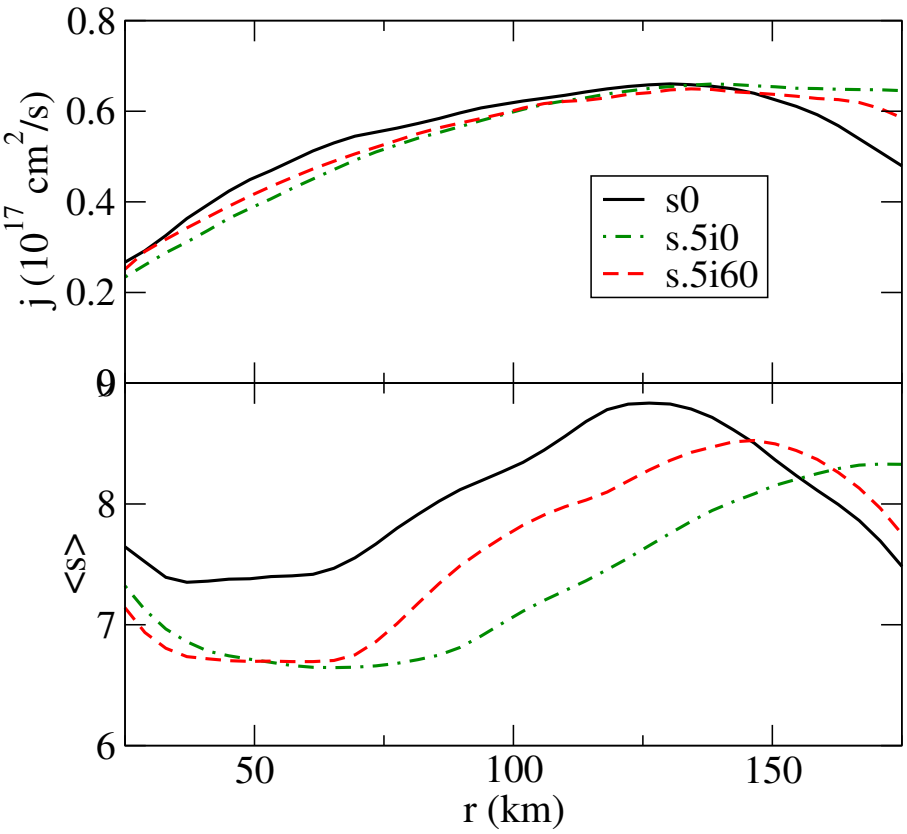

Figure 4.11: *Upper panel:* Specific angular momentum of the accretion disk at $t = 30\mathrm{ms}$ for runs s0, s.5i0 and s.5i60. Note that for the smaller spin s0, the disk does not extend farther than $r \approx 125\mathrm{km}$. *Lower panel:* For the same configurations, entropy of the disk averaged over all points at a given distance from the black hole center.

Fig. 4.13 shows the tilt and twist profiles 20, 30 and 40ms after merger for simulation s.5i60. In the inner part of the disk ($r < 50\mathrm{km}$), the tilt decreases from 15° to 7° over those 20ms. The precession of the disk is more significant: we observe a variation of the twist of about 100° over the same period. However, the precession rate is not constant at all radii and changes in time; the disk has not reached a state in which it precesses at a constant rate as one solid body. For smaller inclinations, relative variations in the tilt are larger. The inclination of the disk decreases at late-time to $\beta < 5^\circ$, and no global precession is observed.

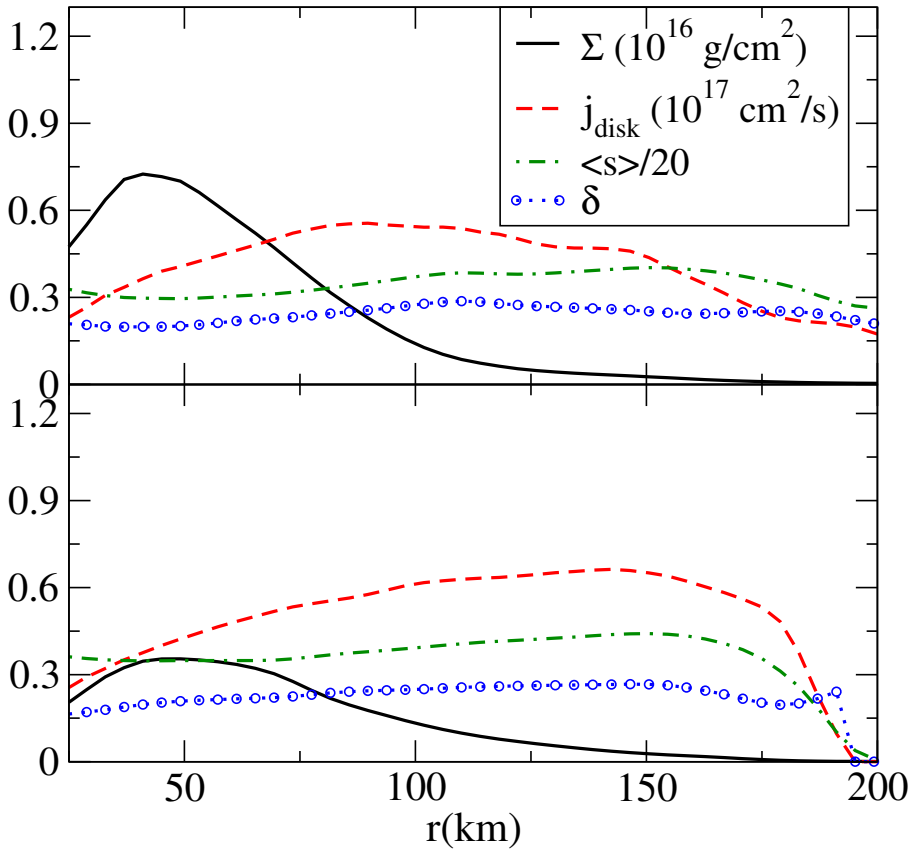

Figure 4.12: Profile of the disk forming in the simulation s.5i60 at $t = 20\text{ms}$ (upper panel) and $t = 40\text{ms}$ (lower panel).

An inclined disk showing some similarities with the results of our most inclined simulations (s.5i60 and s.5i80) was evolved in the presence of magnetic fields by Fragile *et al.* [43]. Even though the two simulations vary greatly in their initial conditions — Fragile *et al.* start their simulation from a torus of matter with peak density at $r = 25M$ ($\sim 200\text{km}$) — the thickness and inclination of the disks are equivalent and some results from [43] could apply to the late time behavior of our disks. In Fragile *et al.*, the inner disk is warped by the gravitomagnetic torque of the black hole, leading to larger tilts at lower radii. The same torque leads to a precession of the disk over a period of about 4s (for a black hole remnant of final mass $M_{\rm BH} = 5.6M_\odot$). This last effect is, however, acting over

timescales longer than the lifetime of the disk formed in BHNS mergers, so that it seems unlikely that our disk would have time to reach the steady precession described in [43]. The magneto-rotational instability (MRI), on the other hand, appears to develop over roughly one orbital timescale, or about $20\mathrm{ms}$ for the initial configuration chosen in [43] and a central black hole of mass $M_{\rm BH} = 5.6 M_\odot$. The rise of the MRI might be even faster for a disk more similar to the results of our simulations, as the peak of the density profile is significantly closer to the black hole in our disks than in [43], and the evolution timescale is thus shorter: the orbital period of circular orbits at $r = 50\mathrm{km}$ is about 5ms. The MRI should have a strong influence on the redistribution of angular momentum in the fluid, and therefore on the accretion rate. However, the accretion rate is also influenced by the presence of shocks in the disk (see e.g. Fragile and Blaes [42] for shocks in tilted disks similar to [43]). This means that interactions between the disk and the matter falling back in the tidal tail are also likely to play an important role in the determination of the lifetime of the disk. Thus, both the magnetic effects and realistic initial conditions are required to accurately predict the lifetime of the disks resulting from BHNS mergers.

4.7 Conclusions

Astrophysical BHNS binaries are expected to have BH spins that are not aligned with the orbital angular momentum of the system. We performed here the first fully general relativistic simulations of BHNS systems with precessing orbits. We find that for realistic inclinations of the BH spin with respect to the initial orbital angular momentum ($\phi_{\rm BH} = 0 - 80^\circ$), a mass ratio of 1:3, and a moderate black hole spin $a_{\rm BH}/M_{\rm BH} = 0.5$, the mass of the disk varies by about a factor of 2.

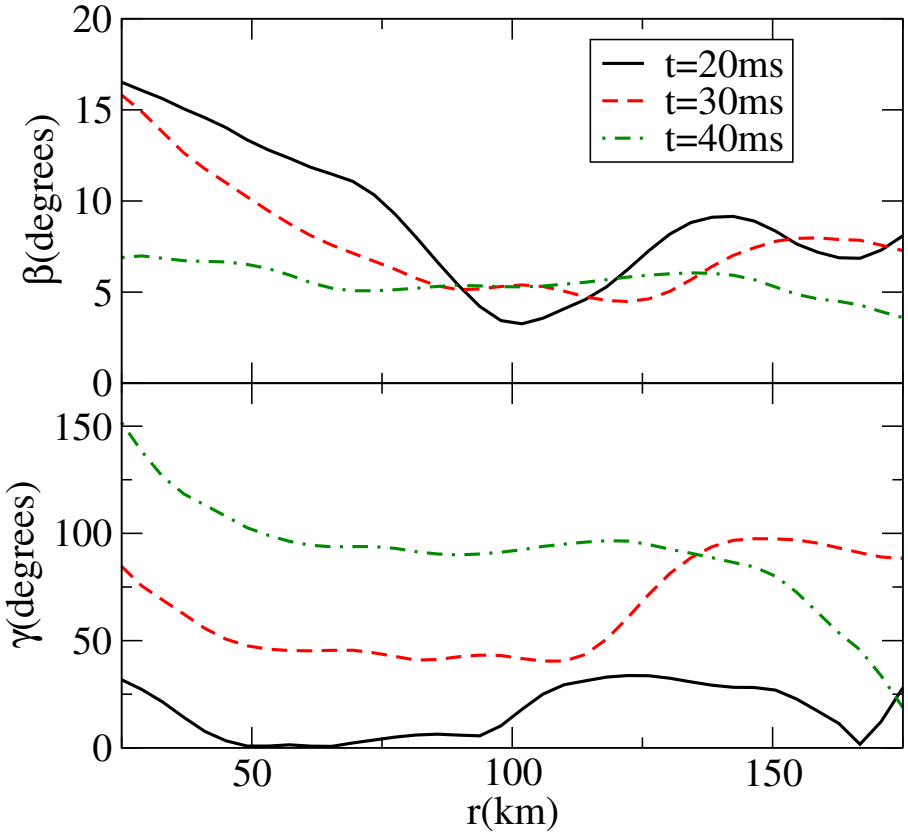

Figure 4.13: *Upper panel:* Tilt profile of the accretion disk formed in simulation s.5i60, as obtained from evolutions on a static background metric. The inclination of the disk decreases in time, with $\beta \approx 10 - 15^\circ$ at the time of disk formation, but $\beta \approx 5 - 7^\circ$ towards the end of the simulation. *Lower panel:* Twist profile for the same configuration. Over the 20ms of evolution, the disk goes through more than one fourth of a precession period.

More important, the inclination of the spin seems to have a significant impact on the final remnant only for $\phi_{\rm BH} > 40^\circ$. According to population synthesis models by Belczynski *et al.* [12], this means that, for binaries with initial spin of 0.5, half of the systems would have disks nearly as massive as if the BH spin was aligned with the orbital angular momentum of the system. This confirms the relevance of the aligned BHNS studies previously undertaken by ourselves and by other groups. At late times, the inclination of the disks formed in these precessing

systems remain relatively modest ($\beta < 15^\circ$). Most of the angular momentum of the system is in the orbital motion of the binary, which precesses around the total angular momentum of the system at a small misalignment angle ($\sim 5-20^\circ$ for $\phi_{\rm BH} = 20-80^\circ$). The black hole spin axis itself is inclined at a larger angle to the total angular momentum, but its misalignment decreases as the hole accretes matter from the disrupted neutron star. This suggests that more inclined disks could be observed for larger black hole spins or more extreme mass ratios. Here, our most inclined binaries have an average tilt $\beta \sim 10^\circ$. From the results of Fragile *et al.* [43], we would expect those disks to precess as one solid body around the black hole — but only over timescales far longer than the expected lifetime of our post-merger disks ($\tau_{\rm prec} \sim 4s >> \tau_{\rm acc} \sim 100{\rm ms}$).

For spins aligned with the orbital angular momentum, our study shows qualitative agreement with previous results by Etienne *et al.* [33]. As expected, large spins favor the formation of a massive disk. By studying a higher initial spin ($a_{\rm BH}/M_{\rm BH} = 0.9$), we also show that large disks of mass $M_{\rm disk} \approx 0.5 M_\odot$ can be obtained for $M_{\rm BH} = 4.2 M_\odot$.

All the cases studied here produce post-merger systems that are promising SGRB central engines. Despite large differences in the disk masses, the lifetime of the system seems mostly independent of the black hole spin; we find an accretion timescale $\tau_{\rm acc} \sim 75-150{\rm ms}$ for all cases. The disks have a peak surface density located about $50{\rm km}$ away from the hole, and extend about twice as far. They are always thick ($H/r \approx 0.2$), hot ($\langle T \rangle = 3-5$MeV), and accreting at a super-Eddington rate ($\dot{M} = 0.5-5 M_\odot/s$). All simulations also show the presence of a baryon-free region, at least at densities above the threshold at which atmospheric corrections begin to have an impact ($\sim 10^9 {\rm g/cm^3}$). This region cov-

ers a cone with an opening angle of $30 - 50^{\circ}$ around the axis of the black hole spin, except for the high-spin configuration for which the disk is significantly closer to the BH, and the opening angle varies within the range $5 - 10^{\circ}$. Such a region is required if relativistic jets are to be launched.

Accretion continues throughout the disk evolution, but the thermal and rotational profiles do seem to stabilize. The specific angular momentum of the disks increases with radius, so they are not subject to the Rayleigh instability. The angular velocity, however, decreases with radius, so these disks are subject to the magneto-rotational instability (MRI), an effect not included in our simulations.

The late-time behavior of the black hole-accretion disk system is critical if we want to understand the potential of BHNS mergers as progenitors for short gamma-ray bursts. Currently, the measurement of the properties of the disk and their evolution in time suffers from the limitations of our simulations. The general characteristics of the disk can be obtained, but a more detailed evolution would certainly require the inclusion of magnetic fields and neutrino radiation. These effects will be added to our evolutions in the near future.

APPENDIX A

ADDITIONAL COMMENTS ON THE INITIAL DATA PROBLEM FOR BHNS BINARIES

In Chapter 2, we described the algorithm developed for the solution of the initial data problem for BHNS binaries. The general procedure described in that chapter is still used in our initial data solver today, although some parts of the algorithm have been modified to handle new configurations (generic spin orientation and equations of state), as well as to improve the accuracy and the convergence properties of the solver.

The main set of modifications, allowing the generation of initial data for BHNS binaries in which the black hole spin and the orbital angular momentum are not aligned (thus breaking the equatorial symmetry of the system) is discussed in Section 4.2.1. In this appendix we discuss other recent modifications to the initial data solver, as well as issues specific to systems with parameters more challenging than those studied in Chapter 2: generic equations of state, high mass black holes and high black hole spins.

A.1 Automated choice of the numerical grid

The simulations described in the previous chapters were mostly aimed at the study of BHNS mergers: their evolution was only followed for 2-3 orbits before merger, and the phase accuracy of the gravitational waveforms was not a dominant concern: the more recent simulations (Chapter 4) had phase errors of about $0.1\mathrm{rad}$ over 1 orbit. To obtain longer simulations with low phase error, the accuracy of both the evolutions and the initial data has to be improved.

For the initial data, the main ingredient required to obtain higher-accuracy datasets is a method capable of automatically determining the required grid resolution. Indeed, having over-resolved or under-resolved subdomains can impede both the efficiency and the convergence properties of the elliptic solver. But the optimal distribution of grid points across the various subdomains used in the initial data solver will change for every new configuration studied. Manually optimizing the domain decomposition for every new case can be time-consuming.

To automatically determine how to increase the number of grid points in each subdomain when the resolution of the numerical grid is modified, we measure the power contained in the modes of the spectral expansion of the metric quantities for each basis function of each subdomain. For example, if the functions on a given subdomain are decomposed spectrally on the basis $(B_0^i[x], B_1^j[y], B_2^k[z])$ as

$$f(x,y,z) = \sum_{i,j,k} a_{i,j,k} B_0^i(x) B_1^j(y) B_2^k(z), \tag{A.1}$$

we can measure the power in the i^{th} mode of the decomposition in the basis B_0 by averaging the $a_{i,j,k}$ over all (j,k). Comparing the power in the lowest order modes with that in the highest order modes gives an estimate of the current truncation error, while the rate at which that power decreases gives an estimate of the number of modes which should be added to reach a target accuracy[1].

In practice, simply modifying the grid resolution according to the results of this spectral analysis leads to undesirable behavior: the elliptic solver con-

[1]The tools needed to use the spectral decomposition of a function to predict the resolution required to reach a given accuracy were developed by Bela Szilagyi for the numerical evolution of Einstein's equations. We use the same methods here, but with different prescriptions on how to modify the resolution as the objective of the grid modification in the initial data solver is to increase accuracy across the grid in a balanced manner, while in numerical evolutions the objective is to maintain a given accuracy at all times.

verges more easily when subdomains sharing a boundary have the same grid structure on that boundary. Indeed, at subdomain boundaries we have to match the solution of the elliptic equation in each neighboring subdomain, as well as its derivative along the normal to the boundary surface. If the grid structure on the boundary is the same for all subdomains, we can match local values of the solution directly, and avoid the need for interpolation on the surface. This is naturally more efficient, but also simplifies the structure of the global elliptic problem and helps the convergence of the elliptic solver. On a surface at the boundary of multiple subdomains, it is thus preferable to enforce the condition that the grids of all these subdomains match exactly on their shared surface (e.g. concentric spherical shells are forced to have the same angular resolution, coaxial cylinders have the same azimuthal and vertical resolutions,...).

To choose a new numerical grid automatically, we thus first determine what the resolution in each subdomain should be for the spectral expansion of the solution to reach the desired accuracy, then add the requirement that touching subdomains should have the same resolution on their shared boundaries — that of the subdomain which initially requested the finest grid. In Fig. A.1, the logarithm of the measured truncation error is plotted as a function of the number of points in each dimension $N^{1/3}$, where N is the total number of grid points. The automated choice of the numerical grid maintains mostly exponential convergence down to truncation errors of order 10^{-9}. For comparison, the initial data used in previous simulations had a truncation error of order $10^{-7.5}$ with $N^{1/3} \sim 65 - 70$ (and obtaining lower truncation errors was difficult without optimizing the distribution of grid points between the various subdomains by hand).

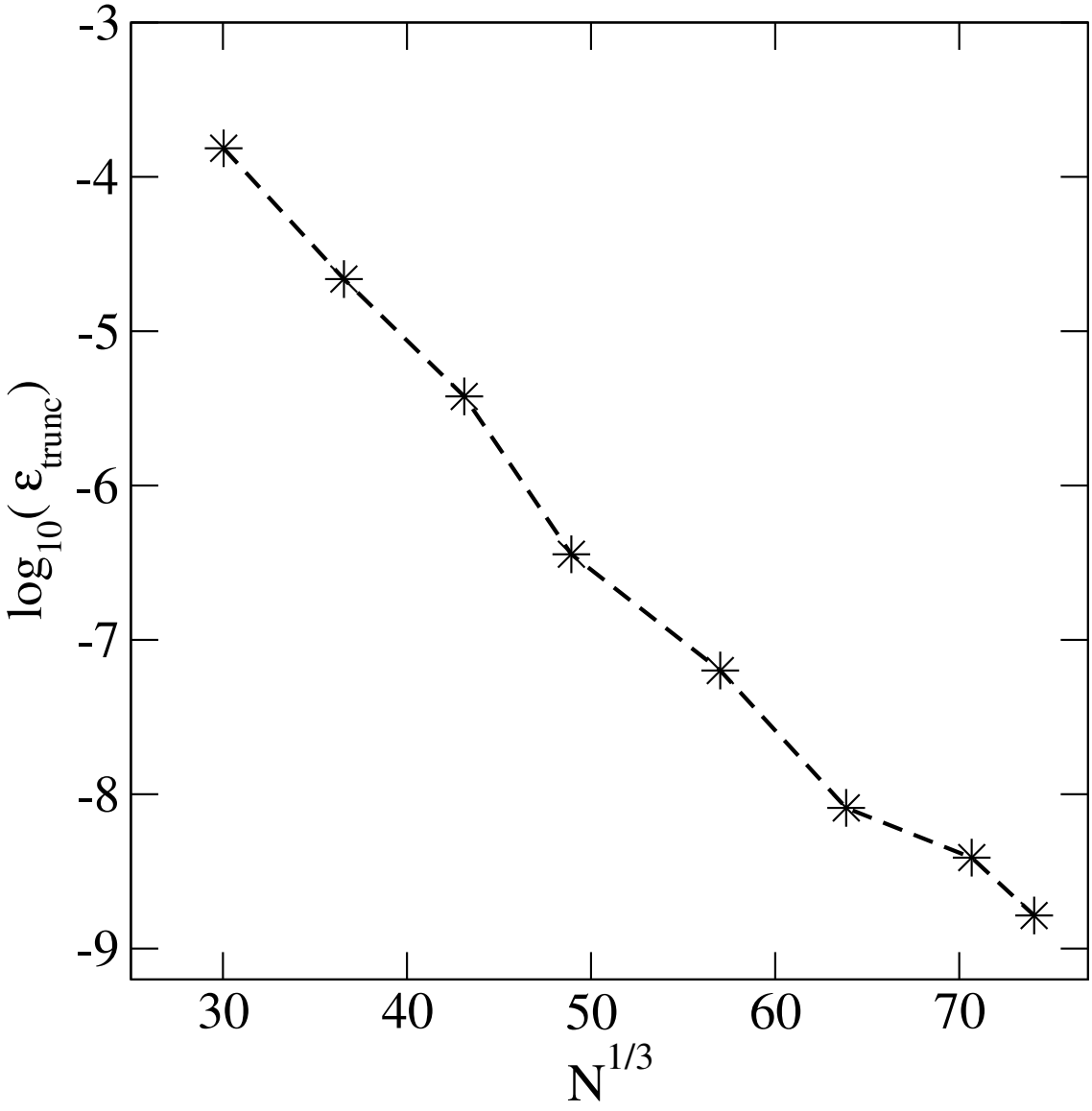

Figure A.1: Logarithm of the measured truncation error as a function of the average number of grid points in each dimension, $N^{1/3}$.

More importantly, the improved accuracy in the initial data significantly reduces the error in numerical evolutions. For a BHNS with $M_{\rm BH} = 10 M_\odot$ and $a_{\rm BH}/M_{\rm BH} = 0.7$, we find that evolutions over 7 orbits using initial data generated without using the automated choice of the numerical grid (truncation error $\sim 10^{-7.5}$) caused errors of order of $9{\rm ms}$ in the merger time (when comparing our low and medium resolutions). Additionally, there was no convergence of the solution at higher resolution. Evolving with the new method (truncation error $\sim 10^{-9}$) we observe convergence between the 3 resolutions used (see Fig. A.2), as well as reduced errors: the merger time, for example, differs by 1.6 ms between the low and medium resolutions, and by only 0.5 ms between the medium and high resolutions[2].

A.2 Convergence of the elliptic solver for high mass black holes

When the black hole mass is significantly higher than the neutron star mass, the accuracy of the elliptic solver in the neighborhood of the black hole can suffer from the fact that the residual R of the elliptic equations becomes dominated by the error around the neutron star: the residual corresponding to an error ϵ_V in a variable V varying over a length scale L is $R \propto \epsilon_V/L^2$ (as we use the second derivatives of the fields). Thus, around a compact object of mass M we have $R \propto \epsilon_V/M^2$. However, the resolution of the numerical grid in the initial data is determined by measuring the truncation error in V (see previous section), while

[2]Note that these errors were not visible in previous simulations as the "medium" resolution used here is equivalent to the "high" resolution from Chapters 3-4 and the length of the simulation has been increased from 2-3 orbits to 5-7 orbits. It is the increased accuracy requirements for these longer simulations that have made more accurate initial data necessary.

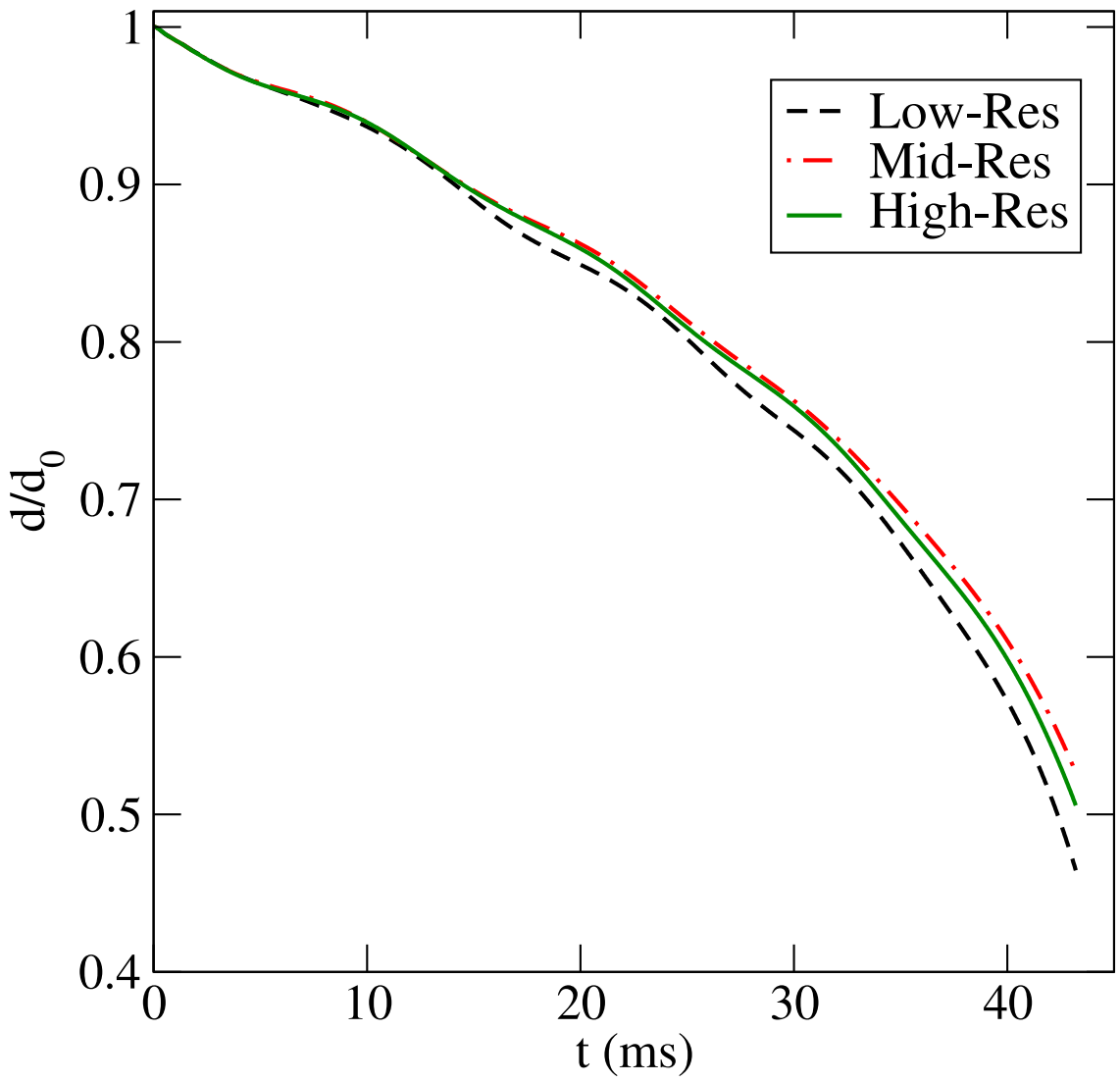

Figure A.2: Evolution of the coordinate separation of a BHNS at low, medium and high resolutions using initial data with truncation error $\sim 10^{-9}$.

the elliptic solver will solve the initial data problem up to a given accuracy in the residual of the elliptic equations. This can translate into an error in the variable V that is much larger around the black hole than around the neutron star — even though we have the numerical resolution required to get the same accuracy in the spectral expansion of V around both compact objects.

We found that the accuracy of the initial data, and the convergence properties of the resulting numerical evolutions, were significantly helped if the elliptic equations were multiplied by a smooth function f chosen so that $f = 1$ away from the neutron star and $f = \left(\frac{M_{\rm NS}}{M_{\rm BH}}\right)^2$ close to the center of the star. Solving the elliptic equations without this global multiplier remains possible, but significantly less accurate for a fixed numerical resolution. The initial data for the evolutions shown in Fig. A.2 used this scaling of the residual.

A.3 Stellar surface

A.3.1 Convergence of the spectral expansion

When using pseudo-spectral methods, the stellar surface is generally an issue: at the surface the density (and other functions describing the fluid) is only C^0 and metric quantities are C^2 — but spectral methods are exponentially convergent only for C^∞ functions. In Chapter 2, we showed that one way around this issue is to make sure that the surface is at a subdomain boundary, so that the discontinuity at the stellar surface does not affect the properties of the spectral expansion within the neighboring subdomains.

However, this work-around is only perfect if the equation of state near the surface is polytropic of index $\Gamma = 1 + 1/n$, with n a positive integer. This can be most easily seen in the case of an isolated neutron star in equilibrium. The density of the star is then a solution of the Tolman-Oppenheimer-Volkoff (TOV) equation, which close to the stellar radius R_s can be written

$$\frac{dP}{dR} \approx -\frac{M_{\rm NS}\rho_0}{R_s(R_s - 2M_{\rm NS})} \tag{A.2}$$

or, using $P = \kappa\rho_0^\Gamma$,

$$\rho_0 \approx C_0(R - R_s)^n \tag{A.3}$$

$$P \approx C_1(R - R_s)^{n+1}. \tag{A.4}$$

Thus, if n is not an integer and n_0 is the largest integer smaller than n, we can only guarantee that the fluid parameters are C^{n_0} at the stellar surface. When this is the case, the spectral expansion only shows polynomial convergence of order n_0. For realistic equations of state, this should not be a very significant issue: as n close to the surface is fairly large (≥ 3), we can still obtain accurate initial data at a reasonable cost[3]. The problem is more severe when using polytropic equations of state with $\Gamma > 2$: then, we cannot even guarantee first order convergence at the stellar surface. This is for example the case for the $\Gamma = 2.75$ configurations studied in Chapter 3. For the accuracy level of the simulations used in that study, the slow convergence of the initial data was not an issue — but for simulations requiring higher accuracy initial data, it would be impractical to use equations of state with $\Gamma > 2$ in the low-density region without making significant modifications to the initial data solver.

[3]However, nuclear-theory based equations of state have other issues: they have sharp features at finite density, and are usually given in tabulated form — two properties that create discontinuities in the derivatives of the fluid parameters within the star.

A.3.2 Solving for the velocity potential

Another issue related to the behavior of the matter density close to the stellar surface is its effect on the properties of the elliptic equation describing the velocity potential Ψ (eq.[2.29]). We already touched on this issue in Sec. 2.3.2: as ρ_0 goes to 0, the coefficient of the second order term in the elliptic equation vanishes, and the equation for Ψ is only first order at the stellar boundary. The elliptic solver converges very slowly for equations in which the second-order term becomes negligible. An improvement to the preconditioning methods used in the elliptic solver was proposed in Sec. 2.3.2, and allowed us to avoid this issue for BHNS binaries using $\Gamma = 2$ equations of state.

However, the problem is more severe when the low-density region behaves as a polytrope with $n > 1$ ($\Gamma < 2$): then, all terms in equation 2.29 vanish at the stellar surface. For such equations of state, it is preferable to multiply equation 2.29 by $\rho_0^{-1+1/n} = \rho_0^{\Gamma-2}$. Then, the second-order terms in equation 2.29 are proportional to $(R - R_s)$ in the neighborhood of R_s, while the first-order terms are asymptotically constant in the same region.

A.4 Preconditioning of elliptic equations

The convergence of the elliptic solver is strongly dependent on the quality of the preconditioning of the elliptic equations. Indeed, let us consider the elliptic equation

$$L[f] = \left[D_2^{ij}\partial_{ij}^2 + D_1^i\partial_i + D_0\right] f = C, \tag{A.5}$$

where the coefficients C and D are functions of the spatial coordinates[4]. The number of iterations required for the elliptic solver to converge is proportional to

$$\kappa = \frac{\lambda_{\max}}{\lambda_{\min}} \tag{A.6}$$

(ot its square root for more efficient iterative methods such as GMRES), where $\lambda_{\max}$ and $\lambda_{\min}$ are the largest and smallest eigenvalues of L. We thus want to maintain $\kappa \sim 1$. This is done by multiplying the equations by an approximation of the inverse operator L^{-1} [93].

For most BHNS configurations, we use the same prescriptions as Pfeiffer et al. [93] for the preconditioning of the elliptic solver. The differential operator L is approximated using a second order accurate finite difference stencil, and the mixed-derivatives terms D^2_{ij} (with $i \neq j$) are neglected. In d dimensions, the finite-difference operator $L_{\rm FD}$ is then a sparse matrix with only $(2d+1)$ non-zero coefficients on each line. The preconditioning matrix is then an approximation of the inverse operator $L^{-1}_{\rm FD}$.

For compact stars or high mass black holes, this preconditioning is not always sufficient. We observe that better results can be obtained by taking into account the mixed-derivatives terms. These terms can be written to second order as

$$\frac{\partial^2 f(x_1, y_1)}{\partial x \partial y} = \frac{f(x_2, y_2) + f(x_0, y_0) - f(x_2, y_0) - f(x_0, y_2)}{\Delta x_{21}\Delta y_{21} + \Delta x_{21}\Delta y_{10} + \Delta x_{10}\Delta y_{21} + \Delta x_{10}\Delta y_{10}} \tag{A.7}$$

where $\Delta x_{ij} = x_i - x_j$. Clearly, the cost of introducing those new terms is not negligible: it adds $2d(d-1)$ non-zero coefficients to each line of $L_{\rm FD}$, increasing the difficulty of the inversion process. Whether to introduce them or not

[4]The coordinates here refer to the topological coordinates of the domain, i.e. the coordinates on which we perform the spectral expansion. The effects of the map between the topological coordinates and the 'physical' coordinates are taken into account in the computation of the coefficients D_1 and D_2

is thus a trade-off between the potential gain in the number of steps required for the elliptic solver to converge (if $L_{\rm FD}^{-1}L$ is closer to the identity when the mixed-derivatives terms are introduced) and the increased cost of each step as the structure of $L_{\rm FD}$ becomes more complex.

A.5 Angular velocity for quasi-circular orbits

The determination of the angular velocity Ω of a binary in quasi-circular orbit is obtained from the solution of equation 2.48. If the conformal metric is flat and we neglect the dependance of the right-hand side on Ω, this can easily be reduced to a second-order polynomial equation:

$$b^i \left(\partial_i(\phi^4 r_{\rm NS}^2) - 2\phi^4 r_{\rm NS}^2 \partial_i(\ln\gamma)\right)\Omega^2 + 2\left(b^i(\partial_i(\boldsymbol{r}_{\rm NS}\times\boldsymbol{\beta})^z - 2(\boldsymbol{r}_{\rm NS}\times\boldsymbol{\beta})^z\partial_i(\ln\gamma))\right)\Omega$$
$$-b^i\left(\partial_i(\alpha^2-\gamma_{ij}\beta^2) - (\alpha^2-\gamma_{ij}\beta^2)\partial_i(\ln\gamma)\right) = 0 \qquad \text{(A.8)}$$

where β is the shift in inertial coordinates, $\boldsymbol{r}_{\rm NS}$ is the location of the neutron star center and γ is computed for the previous value of Ω. All metric quantities are computed at the neutron star center, and we assumed that Ω points along the z-axis while $z_{\rm NS} = 0$. The solution to this equation can thus be obtained simply by interpolating the coefficients of the above polynomial at $\boldsymbol{r}_{\rm NS}$, and solving for its largest root (the largest and smallest root for Ω correspond to solutions for which $\Omega > 0$ and $\Omega < 0$, both of which always exist).

Because we solve for Ω from an approximate solution, we sometimes find that this polynomial equation has no real root. In that case, we obtain an approximate value for Ω by setting the discriminant of the second-order polynomial to 0. We also require $\Omega > \Omega_{\rm min}$ for some small positive value $\Omega_{\rm min}$.

APPENDIX B

PRIMITIVE VARIABLE INVERSION AND ATMOSPHERE TREATMENT FOR GENERAL RELATIVISTIC (MAGNETO)HYDRODYNAMICS

The evolution of the fluid variables in SpEC is done using a conservative scheme: the evolution variables $\boldsymbol{U}$ are chosen so that they satisfy an equation of the type

$$\partial_t \boldsymbol{U} + \nabla \cdot \boldsymbol{F}(\boldsymbol{U}) = \boldsymbol{S}(\boldsymbol{U}), \tag{B.1}$$

where the fluxes $\boldsymbol{F}$ and source terms $\boldsymbol{S}$ do not depend on the derivatives of $\boldsymbol{U}$. However, the equation of state and stress-energy tensor of the fluid are given as a function of the primitive variables $\boldsymbol{P}$: ρ_0 (baryon density), T (temperature), Y_e (electron fraction), u_i (spatial components of the 4-velocity) and B^i (spatial components of the magnetic 4-vector).

In SpEC, the conservative variables are defined as

$$\rho_* = \alpha\sqrt{g}\rho_0 u^0 \tag{B.2}$$

$$\tau = \alpha^2\sqrt{g}T^{00} - \rho_* \tag{B.3}$$

$$S_k = \alpha\sqrt{g}T^0_k. \tag{B.4}$$

Note that Y_e, when evolved, is both a primitive and conservative variable. Using the definition of the stress-energy tensor $T^{\mu\nu}$

$$T^{\mu\nu} = (h\rho_0 + b^2)u^\mu u^\nu + \left(p + \frac{b^2}{2}\right) g^{\mu\nu} - b^\mu b^\nu \tag{B.5}$$

$$b^\mu = \frac{1}{W}(B^\mu + u^\mu u_\nu B^\nu), \tag{B.6}$$

and the identity

$$b^2 = \frac{1}{W^2}\left(B^2 + (B^i u_i)^2\right) \tag{B.7}$$

we get the explicit expressions

$$\rho_* = \sqrt{g} W \rho_0 \tag{B.8}$$

$$\tau = \sqrt{g}\left(h\rho_0 W^2 + B^2\left(1 - \frac{1}{2W^2}\right) - p - \frac{(B^i u_i)^2}{2W^2} - W\rho_0\right) \tag{B.9}$$

$$S_k = \sqrt{g}\left[\left(h\rho_0 W + \frac{B^2}{W}\right) u_k - \frac{B^i u_i}{W} g_{kl} B^l\right] \tag{B.10}$$

where $W = \sqrt{(1 + g^{ij} u_i u_j)} = \alpha u^0$, g is the determinant of the spatial metric, h is the enthalpy, and p is the pressure. h and p are assumed to be known functions of ρ_0, Y_e and T, given by the choice of equation of state.

B.1 Primitive variable inversion

B.1.1 B=0 case

If there is no magnetic field, the conservative variables are given by

$$\rho_* = \sqrt{g} W \rho_0 \tag{B.11}$$

$$\tau = \sqrt{g}\rho_0 W(h[\rho_0, T, Y_e]W - 1) - \sqrt{g}p[\rho_0, T, Y_e] \tag{B.12}$$

$$S_k = \sqrt{g} h \rho_0 W u_k. \tag{B.13}$$

In general, to invert these equations and find $\boldsymbol{P}(\boldsymbol{U})$ we have to use a multi-dimensional root-finder to solve for W and T, using the identity $\rho_0 = \rho_*/(\sqrt{g}W)$ whenever knowledge of the baryon density is required. The equations used are

$$W^2 - 1 - \left(\frac{S}{\rho_* h(W,T)}\right)^2 = 0 \tag{B.14}$$

$$hW - 1 - \frac{\sqrt{g}p(W,T)}{\rho_*} - \frac{\tau}{\rho_*} = 0 \tag{B.15}$$

where $S^2 = g^{ij} S_i S_j$. Once W and T have been found, it is trivial to compute ρ_0 and u_k.

For the two-dimensional root finding giving us W and T, we use a multi-dimensional Broyden method. When given a good initial guess, this algorithm is efficient and reliable — and, for most of the evolution, we can use the values of W and T at the previous timestep as a reasonable approximation for their current value. However, in the low density region numerical errors in the evolution can cause large relative variations in the measured T and ρ_0. In such cases, the two dimensional root finder can fail to converge. If the 2D Broyden solver does not converge after a predetermined number of iterations, we use a less efficient but more robust method: equation B.14 is taken as the definition of $T(W)$, and we solve equation B.15 as a one-dimensional root-finding problem in W, using the known bounds $1 \leq W \leq \sqrt{1 + (S/h_{\min}\rho_*)^2}$ (where $h_{\min}$ is the minimum value of the enthalpy, ~ 1). If the conservative variables can be inverted, this method is guaranteed to converge. However, every evaluation of B.15 requires solving for $T(W)$, which is itself a one-dimensional root-finding problem — hence the loss of efficiency compared to the 2-dimensional Broyden method. One exception to this prescription is when the enthalpy $h(W, T)$ is known analytically and the temperature $T(h, W)$ can be obtained by a simple algebraic computation. Then, the 1D root finding can be as efficient or more efficient than the 2D method. This simplification is available for the polytropic equations of state used in Chapters 3-4.

B.1.2 Inversion in the presence of a magnetic field

In the presence of a magnetic field, the inversion procedure is more complex. Following the prescriptions of Noble et al. [77], we define the auxiliary variables

$$D = \frac{\rho_*}{\sqrt{g}} \tag{B.16}$$

$$Q_i = \frac{S_i}{\sqrt{g}} \tag{B.17}$$

$$Q^0 = -\frac{\rho_* + \tau}{\sqrt{g}} \tag{B.18}$$

$$Q^2 = g^{ij} Q_i Q_j \tag{B.19}$$

$$H = h(\rho_0, T)\rho_0 W^2, \tag{B.20}$$

so that the relations between primitive and conservative variables can be written as

$$Q^2 W^2 = (W^2 - 1)(B^2 + H)^2 - W^2 \frac{(Q_i B^i)^2 (B^2 + 2H)}{H^2} \tag{B.21}$$

$$Q^0 W^2 = -\frac{B^2}{2}(2W^2 - 1) + W^2 \frac{(Q_i B^i)^2}{2H^2} - W^2 H + W^2 P(\rho_0, T). \tag{B.22}$$

We solve these equations for (T, W^2) using a Newton-Raphson solver, with the constraint $1 < W^2$. These equations are more challenging for the root-finding algorithm, especially in cases where the magnetic and/or kinetic energy of the fluid is large compared to its rest mass energy. When the 2D root-finder for (T, W^2) fails, we can either switch to a slower but more robust 2D inversion in the variables (H, W^2) (similar to the 2D method of Noble et al. [77]), or to a simple 1D bracketing algorithm solving for H (W is then considered as a known function of H).Better root-finding techniques, as well as a 2D solver faster than the Newton-Raphson method, would however be desirable in the magnetic case.

B.2 Atmosphere treatment

The methods used for the evolution of relativistic fluids often assume that $\rho > 0$. In order to avoid numerical problems in regions where no fluid is present, we have to impose $\rho \geq \rho_{\rm floor}$ everywhere: an artificial atmosphere composed of a low-density ($\rho \sim \rho_{\rm floor}$) fluid is added outside the star. However, numerical errors in the evolution of the conservative variables in the low-density region can easily lead to values of $\boldsymbol{U}$ for which the inversion problem has no solution. We thus need appropriate prescriptions to

- Choose the primitive variables in the low-density region so that the influence of that region on the evolution of the high-density fluid is negligible
- Modify the conservative variables to physically acceptable values when the inversion problem has no solution.

B.2.1 Fixing the conservative variables

Let us consider a point for which τ, $\rho_\star$, the orientation of the vectors $\mathbf{B}$, $\mathbf{S}$ and $\mathbf{u}$ and the metric variables are known. We would like to know what are the maximum values of B and S that allow us to recover the variables W^2 and T. This will occur when all the energy of the fluid is either magnetic or kinetic, with $h = 1$ and $P = 0$. Under those conditions, and defining the scaled variables

$$\tilde{B}^i = B^i \frac{g^{1/4}}{\sqrt{\rho_\star}} \tag{B.23}$$

$$\tilde{\tau} = \frac{\tau}{\rho_\star} \tag{B.24}$$

$$\tilde{S}_i = \frac{S_i}{\rho_\star}, \tag{B.25}$$

we can find a unique solution for $\tilde{S}^2$ and W. First, we note that

$$\tilde{B}^i \tilde{S}_i = \tilde{B}^i u_i. \tag{B.26}$$

Substituting this relation into the definition of τ and S_i, and defining the fixed parameter

$$\mu = \frac{\tilde{B}^i \tilde{S}_i}{\sqrt{\tilde{B}^2 \tilde{S}^2}} \tag{B.27}$$

we get

$$\tilde{\tau} = (W-1) + \tilde{B}^2 - \frac{\tilde{B}^2}{2W^2}(1 + \tilde{S}^2\mu^2) \tag{B.28}$$

$$\tilde{S}_i = (1 + \frac{\tilde{B}^2}{W})u_i - B_i \frac{\sqrt{\tilde{B}^2\tilde{S}^2}\mu}{W}. \tag{B.29}$$

We can then express $\tilde{S}^2$ as a function of W^2:

$$\tilde{S}^2 = (1 + \frac{\tilde{B}^2}{W})^2(W^2-1) + \frac{\tilde{B}^4\tilde{S}^2\mu^2}{W^2} - 2\frac{\tilde{B}^2\tilde{S}^2\mu^2}{W}(1 + \frac{\tilde{B}^2}{W}) \tag{B.30}$$

$$= \frac{(W + \tilde{B}^2)^2(W^2-1)}{W^2 + 2\tilde{B}^2\mu^2 W + \tilde{B}^4\mu^2}. \tag{B.31}$$

Substituting into the expression for $\tilde{\tau}$, we get a fifth order polynomial equation for W:

$$f(W) = W^3 + (\tilde{B}^2 - \tilde{\tau} - 1)W^2 - \frac{\tilde{B}^2}{2}\left(1 + \mu^2 \frac{(W + \tilde{B}^2)^2(W^2-1)}{W^2 + 2\tilde{B}^2\mu^2 W + \tilde{B}^4\mu^2}\right) = 0. \tag{B.32}$$

As

$$f(W) = \frac{W^2 g(W)}{W^2 + 2\tilde{B}^2\mu^2 W + \tilde{B}^4\mu^2}, \tag{B.33}$$

$$g(W) = (W + \tilde{B}^2 - \tilde{\tau} - 1)(W^2 + 2\tilde{B}^2\mu^2 W + \tilde{B}^4\mu^2) - \frac{\tilde{B}^2}{2} - \frac{\tilde{B}^2\mu^2}{2}(W^2 + 2W\tilde{B}^2 + \tilde{B}^4 - 1) \tag{B.34}$$

the only solutions satisfying the physical constraint $W \geq 1$ are roots of $g(W)$. Simplifying our expression for $g(W)$, we get

$$\begin{aligned} g(W) &= \left(W^3 + (\tilde{B}^2 - \tilde{\tau} - 1)W^2 - \frac{\tilde{B}^2}{2}\right) + \\ &\quad \tilde{B}^2\mu^2\left[(2W + \tilde{B}^2)(W + \tilde{B}^2 - \tilde{\tau} - 1) - \frac{W^2 + 2W\tilde{B}^2 + \tilde{B}^4 - 1}{2}\right] \end{aligned} \tag{B.35}$$

$$g'(W) = (W + \tilde{B}^2\mu^2)\left(W + \frac{2}{3}(\tilde{B}^2 - \tilde{\tau} - 1)\right). \tag{B.36}$$

Considering that:

- $g(1) < 0$ if and only if $\tilde{B}^2 < 2\tilde{\tau}$,
- $g(\infty) > 0$,
- $W > 1$ and $\tilde{B}^2 > 2\tilde{\tau}$ ensure that $g'(W) > 0$,

we find that the equations $f(W) = 0$ has a real solution $W > 1$ if and only if the condition

$$\tilde{B}^2 < 2\tilde{\tau} \tag{B.37}$$

is satisfied. The limiting case $W = 1$, $\tilde{B}^2 = 2\tau$, $\tilde{S}^2 = 0$ is obviously a solution corresponding to the case in which all of the energy is magnetic. We can thus fix our primitive variables by imposing

$$\tilde{S}_i \leq \alpha\sqrt{\frac{\tilde{S}^2_{\max}}{(\tilde{S}^0)^2}}\tilde{S}^0_i \tag{B.38}$$

$$\tilde{B}^2 \leq \beta(2\tilde{\tau}) \tag{B.39}$$

where $\tilde{S}^2_{\max}$ is the solution to equations (B.31)- (B.32), $\tilde{S}^0$ is the value of $\tilde{S}$ before it is "fixed", and α and β are arbitrary parameters such that $\alpha, \beta < 1$.

In some cases, there is no need to solve for the roots of Eq. (B.32). Indeed, for $W > 0$, $S^2_{\max}$ given by Eq. (B.31) is monotonically increasing with W. Thus, a

lower bound on W gives a lower bound on $S^2_{\max}$. As we always have

$$\max\left(1, 1+\tilde{\tau}-\tilde{B}^2\right) \leq W \leq 1+\tilde{\tau} \tag{B.40}$$

(the 5th order polynomial (B.32) is negative for $W = 1+\tilde{\tau}-\tilde{B}^2$, positive for $W = 1+\tilde{\tau}$ if $\tilde{\tau} \geq 0$, and negative for $W = 1$ as long as $\tilde{B}^2 \leq 2\tilde{\tau}$), an easy first check on $\tilde{S}^2$ is that if

$$\tilde{S}^2 \leq \alpha \tilde{S}^2_{\max}|_{W=1+\tilde{\tau}-\tilde{B}^2} \tag{B.41}$$

$$\tilde{B}^2 \leq \tilde{\tau} \tag{B.42}$$

then the conservative variables are invertible. Otherwise, the bounds on W can still be used as lower and upper bounds for the root finding algorithm.

Non-magnetic case

When $B = 0$, the equations derived in the previous section can be simplified to

$$\tilde{S}^2_{\max} = \tilde{\tau}(\tilde{\tau}+2) \tag{B.43}$$

and the only condition for the conservative variables to be invertible is $\tilde{S}^2 < \tilde{S}^2_{\max}$. We will thus 'fix' non-invertible points by requiring

$$\tilde{S}_i \leq \alpha \sqrt{\frac{\tilde{S}^2_{\max}}{(\tilde{S}^0)^2}} \tilde{S}^0_i \tag{B.44}$$

where $\tilde{S}^0$ the value of $\tilde{S}$ before it is "fixed" and $\alpha < 1$.

B.2.2 Additional approximations in the low-density region

Large errors in the numerical evolution of the atmosphere can have significant undesirable effects: the atmosphere can be artificially heated or accelerated, and

the thermal and kinetic energy thus created can affect the high-density regions of interest. To avoid these effects, we effectively forbid any change of temperature or velocity in the low density region: we choose a threshold density $\rho_{\rm atm} > \rho_{\rm floor}$, and require that for $\rho < \rho_{\rm atm}$ we have $T = 0$ and $u_i = 0$.

Additionally, in order to avoid a sharp transition from the 'exact' evolution to the atmosphere prescription, we add a smoothing region for $\rho_{\rm atm} < \rho < 10\rho_{\rm atm}$ where we require $T \leq \kappa T_{\rm max}$ and $u^2 \leq \kappa u^2_{\rm max}$, with $\kappa = (\rho - \rho_{\rm atm})/(9\rho_{\rm atm})$. $T_{\rm max}$ and $u^2_{\rm max}$ are values larger than the temperatures and velocities encountered in the high-density region of the simulation.

Similar conditions could be imposed on the magnetic fields if it proves to be necessary in future magnetohydrodynamics simulations.

APPENDIX C

REGRIDDING IN SPEC: AUTOMATED DETERMINATION OF THE GRID FOR THE EVOLUTION OF FLUIDS IN BHNS MERGERS

The main advantage of the two-grid method used in the SpEC code for the evolution of BHNS binaries is to limit the cost of the fluid evolution: the finite difference (FD) grid on which we solve the equations of hydrodynamics can be confined to regions in which a significant amount of matter is present. However, the distribution of matter across the grid varies in time. Thus, if we want to take full advantage of the two-grid decomposition, we should let its size and location change in time. This could be done continuously, but such an algorithm would come with its own computational cost: the main cost in the interpolation of source terms between the spectral and FD grids is to set up the interpolation routines for given sets of grid points. As this step has to be taken every time the map between the coordinates of the spectral grid and those of the FD grid is modified, and interpolation represents a significant share of the computational cost of our simulations ($20-60\%$, depending on resolution and the size of the FD grid), continuous changes in the coordinate maps are not desirable.

Keeping the map between grids fixed for long periods of time (long enough that manually modifying the location of the FD grid would be feasible) is usually not optimal either: the grid then has to cover all regions in which matter will be present at some point in the simulation. In the presence of a long tidal tail rotating around the black hole, that region can be much larger than the original size of the star, or even the orbital separation of the binary ($\sim$ the required length scale of the grid at the time of tidal disruption).

Additionally, even when an extended grid is required, we would like to

maintain higher resolution in the region surrounding the black hole (where an accretion disc forms and we have large gradients in the fluid variables and shocks) than around the tidal tail.

To optimize the size of the FD grid without incurring too large an increase in the interpolation costs, we thus developed an algorithm automating the process of:

- Determining whether the current FD grid is still adapted to the matter distribution,
- Choosing a new FD grid when necessary, so that it is adapted to the current matter distribution and will remain adapted for a significant number of time steps,
- Interpolating all fluid variables onto the new grid and continuing the numerical evolution without interruption,
- Maintain high resolution around the black hole even while covering an extended tidal tail.

An overview of this algorithm was given in Sec. 4.2.2. Here, we offer more details on the choices made when using automated regridding.

C.1 Choosing the conditions for grid changes

The size of the finite difference grid is typically chosen so that only a negligible amount of matter escapes from the grid boundaries. The easiest condition to impose, shown in Fig. C.1, is to require that all points above a certain baryon

density $\rho_0^{\min}$ are farther than a distance $d_{\min}$ from each grid boundary, while all boundaries have at least one such point at a distance closer than $d_{\max} > d_{\min}$. The minimum distance $d_{\min}$ should be far enough from the boundary for the evolution to avoid being influenced by boundary conditions, while the choice of the size of the "buffer zone" $d_{\max} - d_{\min}$ is a trade-off between regridding more often (small buffer zone) and wasting more grid points in low-density regions (large buffer zone).

The advantages of the density-contour method are its simplicity and independence from the choice of atmosphere parameters (as long as $\rho_0 >> \rho_{\rm atm}$). It is well suited to the determination of the finite difference grid before tidal disruption, and even in the early stages of tidal tail formation. However, it performs poorly when the tidal tail expands and the grid becomes large. Indeed, the rate at which matter escapes from the numerical grid is $\sim \rho_0 v S_{\rm gr}$ where $S_{\rm gr}$ is the area of the grid boundary. As $S_{\rm gr}$ can vary by many orders of magnitude after tidal disruption, fixing the grid through contours of ρ_0 is no longer appropriate.

Using $\rho_* = u^0 \sqrt{g} \rho_0$ is safer, as long as it is measured in the grid frame (the $\sqrt{g}$ factor then takes into account the stretching of the grid). But even then, the contour method suffers from an important drawback: it does not measure the area over which matter escapes from the grid. At late times, we only have significant outflows in small portions of the boundary, the parts reached by the tidal tail (see Fig. C.1). Measuring only ρ_* without taking into account the surface area over which matter escapes from the grid leads us to be overcautious in the determination of the grid size, which comes at the cost of a larger grid spacing in the regions where most of the matter is present.

A safer method is to measure the flux of matter across boxes at distances $d_{\min}$

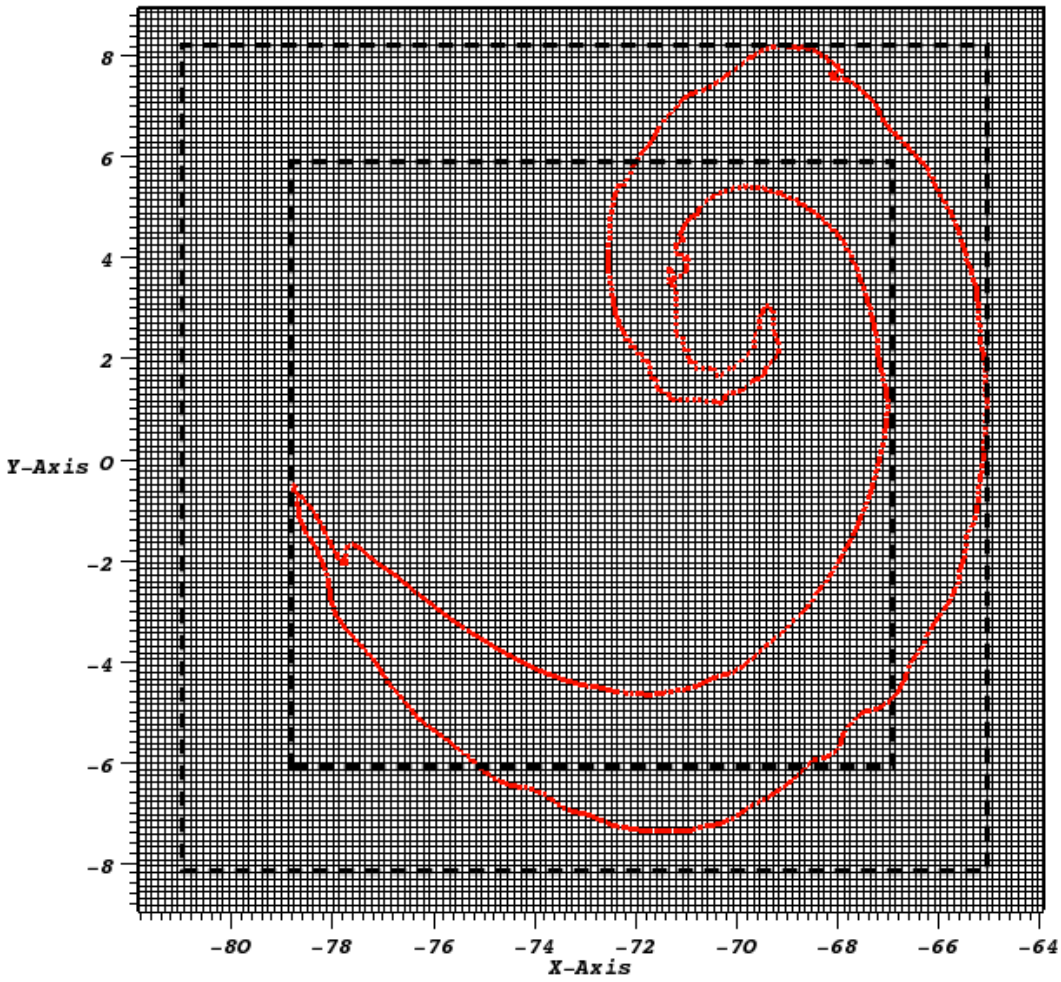

Figure C.1: Regridding from density contours: when the chosen contour of ρ_0 (in red) no longer resides at a distance between $d_{\min}$ and $d_{\max}$ of a given boundary (dashed boxes), a regrid is required. Here, we would request an expansion of the grid towards the right and the top (as the chosen contour is getting closer than $d_{\min}$ from those boundaries) and a reduction of the grid from the left (as no high-density region is within $d_{\max}$ of the left boundary). The bottom boundary would not be modified.

and $d_{\rm max}$ from the boundaries. Integrating $F_\rho = \rho_* \boldsymbol{v} \cdot d\boldsymbol{S}$ over such boxes gives us a direct measurement of the loss of matter that would occur if the grid boundary was placed there. If the flux at $d_{\rm min}$ is above the acceptable rate $\dot{M}_{\rm max} \approx \delta M / T_{\rm sim}$, where δM is the allowed mass loss and $T_{\rm sim}$ the length of the simulation, we expand the grid. If the flux at $d_{\rm max}$ becomes smaller than $\dot{M}_{\rm max}$, we contract it (at $d_{\rm max}$ the flux is measured by integrating $|F_\rho|$, as an incoming flux would be an equally valid indication of the presence of matter) . Outflow measurements, however, are slightly more difficult than direct density measurements — and, as discussed in the next section, they require a more careful consideration of the influence of the atmosphere.

C.1.1 Outflow measurement and atmosphere parameters

In Appendix B, we discussed how the low-density regions are treated when evolving the equations of hydrodynamics. The approximate treatment of the evolution equations in the atmosphere usually results in the formation of an extended region of density $\rho_0 \sim \rho_{\rm atm}$, which is at rest in the inertial frame. However, the fluxes used to determine whether the FD grid is adapted to the current matter distribution are measured close to the outer boundary of the FD grid, in a coordinate frame comoving with that grid. Typically, the FD grid is rotating with respect to the inertial frame at an angular velocity $\Omega_{\rm gr} \sim \Omega(r_{\rm ISCO})$, and expands hundreds of gravitational radii away from the black hole. The flux of atmospheric material across the outer boundary of the FD grid is thus $F_{\rm atm} \sim \rho_{\rm atm} \Omega_{\rm gr} R^3_{\rm bound}$, or a loss of the same order as the total mass of the atmosphere for each orbital period of the inner disc. As the evolution lasts many orbital periods $\Omega_{\rm gr}^{-1}$, this can have a significant effect on the measured outflow of

matter even if the contribution of the atmosphere to the evolution of the system, and to the total mass and angular momentum, is negligible.

To limit the influence of the atmosphere, we exclude from the flux measurements all points with $\rho_0 \lesssim \rho_{\rm atm}$. It is worth noting that, effectively, this means that for large FD grids there is nearly no difference between regrids based on outflow measurements and regrids based on density contours for $\rho_0 \sim \rho_{\rm atm}$: as soon as material at densities higher than $\rho_{\rm atm}$ reaches the outer boundary, its large relative velocity with respect to the FD grid guarantees that a regrid will be quickly requested. Outflow measurements will perform well during the early expansion of the tidal tail, but if the flux ever becomes dominated by atmospheric material, they are no better than the simpler density measurements.

For the simulations presented in Chapters 3-4, the atmospheric flux remained small enough for the outflow measurements to perform well for most of the simulation. However, the influence of the atmosphere is larger for high mass black holes. Two types of improvements have been investigated: automatically decreasing the angular velocity of the FD grid at late times (e.g. by matching the angular velocity of the tail instead of the angular velocity of the disc, or simply driving the angular velocity of the grid to 0), and making the density $\rho_{\rm atm}$ a function of the distance of the fluid element from the central black hole (if $\rho_{\rm atm} \sim 1/R^\alpha$ with $\alpha \geq 3$, the influence of the atmosphere decreases as the outer boundary expands). For the simulations with high mass black holes described in Appendix D, both changes were required to reliably evolve the remnant of BHNS mergers over long timescales.

C.2 Choice of the coordinate map

Once a prescription for when to expand and contract the FD grid has been chosen, we still have to determine how much to modify the grid when a change is requested, and how the cells of the FD grid are distributed in the coordinates of the spectral grid.

The expansion of the grid is typically done so that the old boundary lies about halfway between the new 'outer' and 'inner' boxes at which fluxes will be measured (dashed lines in Fig. C.1), while contractions of the grid do the inverse operation — placing the new boundary roughly halfway between the old boxes used for flux measurement. A simple map of the coordinates x_i of the FD grid can be used for these changes: the combination of a translation of the center of the grid with independent rescalings of each axis:

$$\tilde{x}^i - \tilde{c}^i = (x^i - c^i)a_i \tag{C.1}$$

where $\tilde{\boldsymbol{x}}$ are the mapped coordinates while $\boldsymbol{c}$ and $\tilde{\boldsymbol{c}}$ are the locations of the center of the FD grid in the coordinates of the FD and spectral grids.

For large tidal tails, this would however require $a_i \geq 100$. By that point, the grid spacing is still appropriate for the evolution of the tidal tail, but not for the evolution of the regions closer to the black hole. We thus choose a maximum value $a_{\max}$ of a_i, above which expansions of the grid will use the radial map described in Sec. 4.2.2:

$$r' = \begin{cases} r, & r < r_A \\ f(r) - f(r_A) + r_A, & r_A < r < r_B \\ \lambda(r - r_B) + f(r_B) - f(r_A) + r_A, & r > r_B \end{cases} \tag{C.2}$$

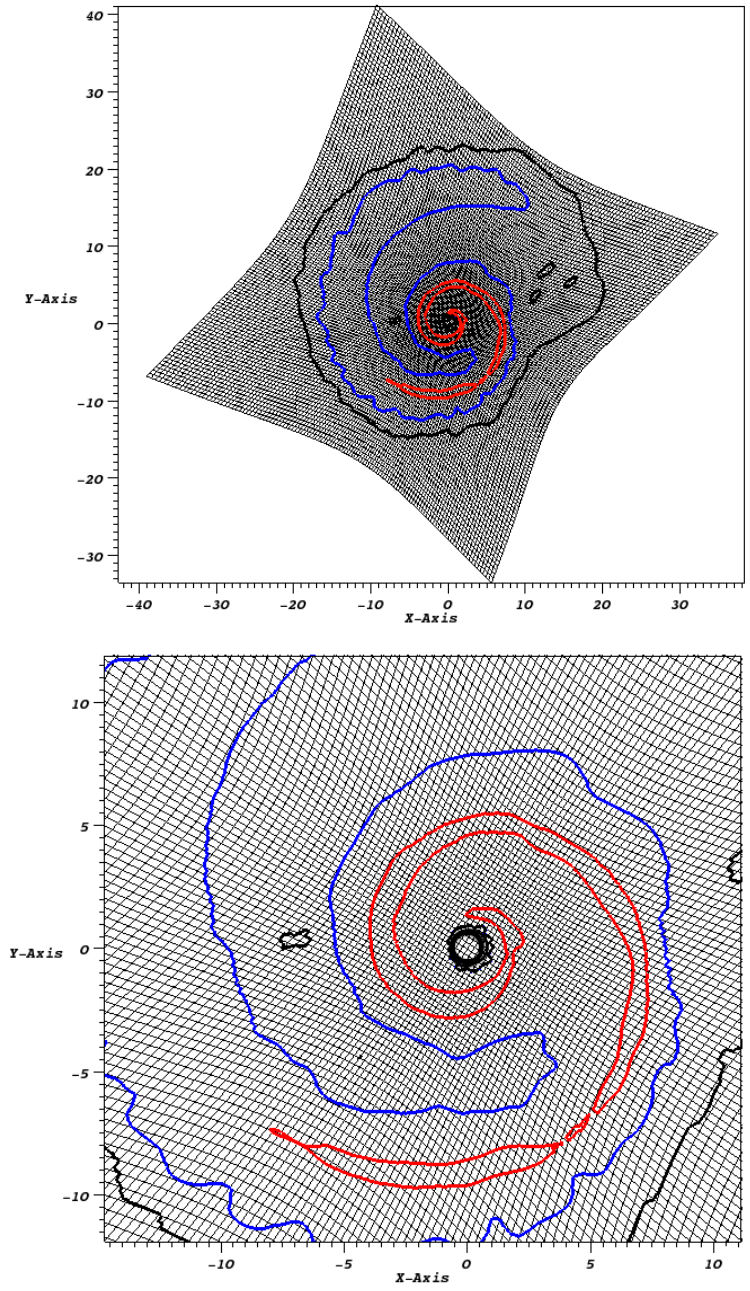

Figure C.2: Grid structure during the merger of a BHNS (1:7 mass ratio). The contours represent densities $\rho_0 \sim (10^{-4}, 10^{-6}, 10^{-8}) M_{\rm BH}^{-2}$. Densities below $\rho_{\rm atm} \sim 10^{-7} M_{\rm BH}^{-2}$ are considered part of the atmosphere. *Top:* Grid viewed from afar. *Bottom:* Zoom on the disc-forming region, where the non-uniform structure of the grid is more visible. Lengths are in units of $M_{\rm BH} \sim 15{\rm km}$.

$$f(r) = r(ar^3 + br^2 + cr + d). \tag{C.3}$$

The constants a, b, c, d are determined by imposing continuity of the first and second derivatives of the map at r_A and r_B. The 7 other unknowns λ, a_i and $c^i_{\rm map}$ (the point from which the radii r, r' are measured) are determined from the desired location of the 6 grid boundaries, as well as the condition $a_i = a_{\rm max}$ for the direction i in which the grid stretching is maximum. The resulting grid structure is shown in Fig. C.2 for the equatorial plane of a BHNS binary at the time when an accretion disc starts to form out of tidally disrupted material. The star-shaped structure of the grid at large distances is a consequence of the use of a radial map. In the equatorial plane, there is no particular reason to wish for points in the ”corners” of the grid to be farther from the black hole than other points of the boundary. But it is convenient to have the same feature in the vertical direction. As the thickness of the disc (and of the tidal tail) $H \propto r$, the grid should cover regions farther from the equatorial plane when away from the black hole.

C.3 Interpolation of the fluid variables

Whenever the map between the coordinates of the FD grid and those of the spectral grid is modified, we have to interpolate the evolution variables from the old FD grid to the new one. Thus, every grid change introduce an interpolation error in the simulation. Errors in this operation are notable because, as opposed to the evolution algorithm, grid-to-grid interpolation does not enforce conservation laws. Thus, every change in the grid is likely to introduce small corrections to the total mass and angular momentum of the system.

We have to verify that grid changes are not frequent enough to significantly affect these conserved quantities. In practice, the grid changes have to satisfy a condition similar to what was used to determine the magnitude of an 'acceptable' matter outflow at the boundary: $\epsilon_M^{\rm regrid} N_{\rm regrid} \lesssim \delta M$, where $\epsilon_M^{\rm regrid}$ is the error in the baryon mass introduced at each grid change, $N_{\rm regrid}$ is the number of grid changes over the whole simulation, and δM is the error in the mass deemed acceptable.

When interpolating the fluid variables on a new FD grid, there is some freedom in the choice of interpolation variables: we can interpolate the evolved variables (ρ_*, τ, S_i) or any choice of 5 independent physical variables, e.g. (ρ_0, h, u_i) or (ρ_0, T, v^i). This is similar to the freedom allowed when choosing the variables to interpolate from cell centers to cell faces when computing the fluxes used for the evolution of the fluid variables in conservative form. And, as for the fluxes, we observe that more accurate results are obtained when interpolating 'physical' variables rather than the evolved variables. We generally interpolate (ρ_0, T, u_i), with u_i measured in the inertial frame, and reconstruct the evolved variables from these physical variables together with the metric quantities interpolated from the spectral grid (when evolving the composition, we also interpolate Y_e).

The regridding technique described in this appendix has made it considerably easier to simulate BHNS mergers. But improvements to our methods — and in particular to the distribution of grid points once a non-uniform grid becomes desirable — still have the potential to increase the efficiency of BHNS simulations, as can be seen from the imperfections in the grid coverage of the matter distribution shown in Fig. C.2.

APPENDIX D

ADDITIONAL CONSIDERATIONS FOR SYSTEMS WITH $M_{\rm BH} \sim 7M_\odot$

Most numerical simulations of BHNS mergers have been limited to relatively low mass black holes ($M_{\rm BH} \sim 3-5M_\odot$), and the few results extending studies of the parameter space up to mass ratios of $1:5$ ($M_{\rm BH} \sim 7M_\odot$) have only considered non-spinning black holes [33, 117]. As population synthesis models indicate that higher mass black holes $M_{\rm BH} \sim 10M_\odot$ might be more common in BHNS binaries (see Introduction), simulations of BHNS binaries with more massive black holes would be desirable.

D.1 Numerical challenges

The simulation of BHNS binaries becomes more challenging for mass ratios $q = M_{\rm NS}/M_{\rm BH} \ll 1$. The first complication is the increased numerical cost of these simulations: the maximum time step for stable numerical evolutions is proportional to the smallest grid spacing (Courant–Friedrichs–Lewy condition), which scales as the mass of the smallest object in the binary. On the other hand, around the time of tidal disruption, the orbital evolution of the system occurs on timescales proportional to the total mass of the system. The number of time steps required to evolve the binary for a set number of orbits thus scales as $M_{\rm NS}/M_{\rm total} \sim 1/q$ (for $q \ll 1$): extreme mass ratios are more costly to simulate.

A more fundamental problem comes from the qualitative differences between BHNS mergers for low and high mass black holes. For low mass black holes (up to $M_{\rm BH} \sim 5-7M_\odot$), the star is tidally disrupted before it plunges into the black hole, even for non spinning black holes. Only in the unlikely case of

a BHNS binary for which the black hole spin is anti-aligned with the orbital angular momentum is a direct plunge of the star possible. But for high-mass black holes, only neutron stars orbiting a rapidly spinning black hole will disrupt.

Each qualitative behavior comes with its own numerical challenges. If early disruption occurs, we have to follow material ejected at large distances in the tidal tail. This requires us to expand the FD grid up to $R_{\rm gr} \sim 50 - 100 M_{\rm BH}$, with the accretion disk forming at a distance $5 - 10 M_{\rm BH}$ from the black hole. Accordingly, the density of the material in the disk and tidal tail will scale as $\rho_0^{\rm tail} \propto M_{\rm tail}/M_{\rm BH}^3$, while the central density of the star scales as $\rho_0^c \propto M_{\rm NS}^{-2}$. Numerical simulations thus have to resolve a range of densities of order $\rho_0^c/\rho_0^{\rm tail} \propto (M_{\rm BH}/M_{\rm NS})^3 (M_{\rm NS}/M_{\rm tail})$. The tidal disruption of the neutron star is thus more challenging to resolve for higher mass black holes (see Appendix C for a discussion of the problems related to the evolution of low-density matter on a large FD grid).

If on the other hand most of the star plunges directly into the black hole, the main challenges come from the variations in the timescales over which the black hole evolves, as well as the rapid motion of high-density material across the numerical grid. We expand on both issues in the following sections.

D.1.1 Control system

In the two-grid method, we have to excise from the spectral grid the region inside of the black hole, and control the shape and size of the excision surface so that it remains inside the apparent horizon of the BH and is not so distorted that some fields would require information from inside the excision

surface to be evolved (in which case an unknown boundary condition would have to be applied on the excision surface). This last condition can be more easily expressed in terms of the characteristic speeds of the evolution equations: as these equations are hyperbolic, we can rewrite them locally as a set of first order differential equations for the characteristic fields of the system, which can be integrated along characteristics curves. Information contained in a given characteristic field will propagate along the associated curve at a speed which can be computed locally. At a boundary, the system can be evolved if we have information on all incoming characteristic fields (characteristic fields for which information flows into the computational domain), but no boundary condition is necessary for outgoing fields. At the excision surface, we thus require that all characteristic fields have outgoing speeds with respect to the computational domain, i.e. the fields propagate towards the inside of the excision region.

Controlling the excision surface is naturally easier if accretion onto the black hole is slow compared to the evolution timescale of the hole before and after disruption (which scales as $M_{\rm BH}$), and if the angular dependance of the matter flow — and thus the distortion of the black hole due to that flow — is weak. The early accretion of mass $M_{\rm core}$ from the undisturbed core of the neutron star (or, lacking tidal disruption, of the entire neutron star) occurs over a time $t_{\rm mer} \sim R_{\rm NS} v_{\rm plunge}$, where the velocity of the stellar core during the plunge is $v_{\rm plunge} \sim 1$. For mass ratios $q \ll 1$, the change of evolution timescales will thus be sharper. The control system used for the simulations of BHNS with $M_{\rm BH} \sim 4M_\odot$ proved to be unable to handle such rapid changes.

In our simulations, the shape and size of the excision surface is determined by a time-dependent map between the inertial coordinates (r', θ, ϕ) and the coor-

dinates of the spectral grid (r, θ, ϕ) (where we use spherical coordinates centered on the BH in both cases). The map is of the form

$$r'(t, r, \theta, \phi) = r \left(1 + \sum_{lm} f(r) c_{lm}(t) Y^l_m(\theta, \phi) \right) \tag{D.1}$$

where the Y^l_m are spherical harmonics, $f(r)$ is a radial function of order 1 close to the BH and 0 away from it (in order for the map to only affect the region immediately surrounding the hole), and the c_{lm} are the coefficients that we control. Coefficients with $l \neq 0$ are chosen so that the apparent horizon remains circular in the grid coordinates, and concentric with the excision surface, while c_{00} allows global variations of the radius of the apparent horizon in grid coordinates.

The simulations described in Chapters 3-4 controlled c_{00} by fixing the radius of the apparent horizon. However, it is not clear a priori what the ideal location of the apparent horizon is. In fact, that ideal location varies from one binary to the next, and even changes in time for a given binary. When the apparent horizon changes slowly, as is the case for low mass black holes, this does not create any problem. But for rapid changes in the shape and size of the apparent horizon, it becomes difficult to evolve the binary through tidal disruption and merger when using that prescription — the parameters of the control system have to be tuned regularly during the evolution, and small differences in the choice of those parameters can be enough for the control system to be unstable. Instead, we use a control system in which c_{00} changes in time so that the characteristic speeds of the system remain outgoing at the excision surface. When the characteristics speeds are in no risk of becoming ingoing, other constraints are chosen for the evolution of c_{00} — aimed at enforcing the desired evolution of the location of the apparent horizon[1].

[1]This control system was developed by Mark Scheel for BH-BH mergers

Another critical improvement to the control system was allowing the timescales over which we vary the parameters c_{lm} to change in time[2]: we generally control the $c_{lm}(t)$ by modifying their third time derivative so that chosen control parameters (e.g. the deviations of the apparent horizon from spherical symmetry) are damped to zero over a given timescale. Previously, that timescale had to be chosen a priori, which made it very difficult to control the excision surface for systems with rapidly varying timescales. More recent simulations — including all the BHNS mergers with $q = 1/7$ discussed here — use a control system capable of evaluating the ideal timescale to damp the amplitude of the oscillations of the control parameters below a given threshold.

D.1.2 Spectral resolution

The rapid motion of the stellar core across the numerical grid causes a different kind of difficulty. High-density regions with sharp gradients require higher resolution in both the FD grid (to resolve the evolution of the fluid) and the spectral grid (as feedback from the material in the stellar core has a significant impact on the evolution of the metric). And as the stellar core remains more compact for more extreme mass ratios, this issue is particularly important when studying the plunge of a neutron star into a high mass black hole. Resolving the stellar core on the FD grid can be well handled through our standard method for modifying the map between the FD and spectral grids (See Appendix C). For the spectral grid, we can use high resolution in all the regions through which the stellar core will pass. This is however fairly costly — and, when considering the most challenging case of a neutron star which is not tidally disrupted, this

[2]The development of adaptive timescales for the control system are mostly the work of Dan Hemberger and Mark Scheel.

technique proved to be insufficient for numerical evolutions with the available computational resources. A more reasonable method is to adapt the spectral grid to the distribution of matter.

The SpEC code was recently modified to allow for adaptive changes to the resolution of the spectral grid[3]. In vacuum, these methods rely on the exponential convergence of the fields with respect to the number of basis functions used in the spectral expansion: an estimate of the current truncation error together with its convergence rate can be obtained as described in Sec. A.1 for the initial data. From these measurements, we can predict the number of basis functions required to reach a given accuracy — and accordingly increase or decrease the grid resolution on the fly. In the presence of matter, we do not expect exponential convergence. However, the measured power in the highest order modes is still an indicator of the truncation error. Using spectral AMR efficiently in the presence of matter is likely to require additional studies of the best ways to modify the spectral grid in response to measured changes in the truncation error. But even using vacuum prescriptions directly, it is possible to obtain significant improvements when merging BHNS binaries with $M_{\rm BH} \sim 10 M_\odot$. Indeed, spectral AMR allows us to limit the increase in resolution to regions in which the stellar core is currently present, instead of requiring high resolution in all regions through which high-density fluid might pass.

[3]These spectral adaptive mesh refinement (AMR) methods are mostly the work of Bela Szilagyi

D.2 Results

Using an improved control system and, in some cases, adaptive refinement of the spectral grid, we obtain the first numerical evolutions of BHNS binaries with $M_{\rm BH} \sim 10 M_\odot$. We consider black hole spins aligned with the total angular momentum of the system, and of magnitude $a_{\rm BH}/M_{\rm BH} = 0.5, 0.7, 0.9$. In Sec. D.2.1, we discuss the qualitative features of those BHNS mergers, while in Sec. D.2.2 we discuss the gravitational wave signal obtained.

D.2.1 Qualitative behavior: Disruption and merger

The qualitative behavior of BHNS binaries during merger is probably the most important difference between the configurations studied in Chapters 3-4 (for which $M_{\rm BH} \sim 4 M_\odot$), and those with $M_{\rm BH} \sim 10 M_\odot$. Indeed, for the latter we find that up to spins of $a_{\rm BH}/M_{\rm BH} \approx 0.5$ there is no significant amount of matter ejected through tidal forces before the neutron star plunges into the black hole. The disruption of the star for a BH spin $a_{\rm BH}/M_{\rm BH} = 0.5$ is shown on Fig. D.1, at a time at which about half of the fluid has already been accreted onto the black hole. Most of the remaining mass is well within the innermost stable circular orbit, and will be accreted within less than a millisecond: the neutron star plunges into the black hole from a separation $d \approx 4 M_{\rm BH} \approx 60 {\rm km}$, and we can see that nearly all of the matter is still well within that separation as the stellar core is accreted onto the black hole.

This behavior should be compared to the case $a_{\rm BH}/M_{\rm BH} = 0.7$, shown in Fig. D.2. There, about 10% of the mass forms a long tidal tail, and remains

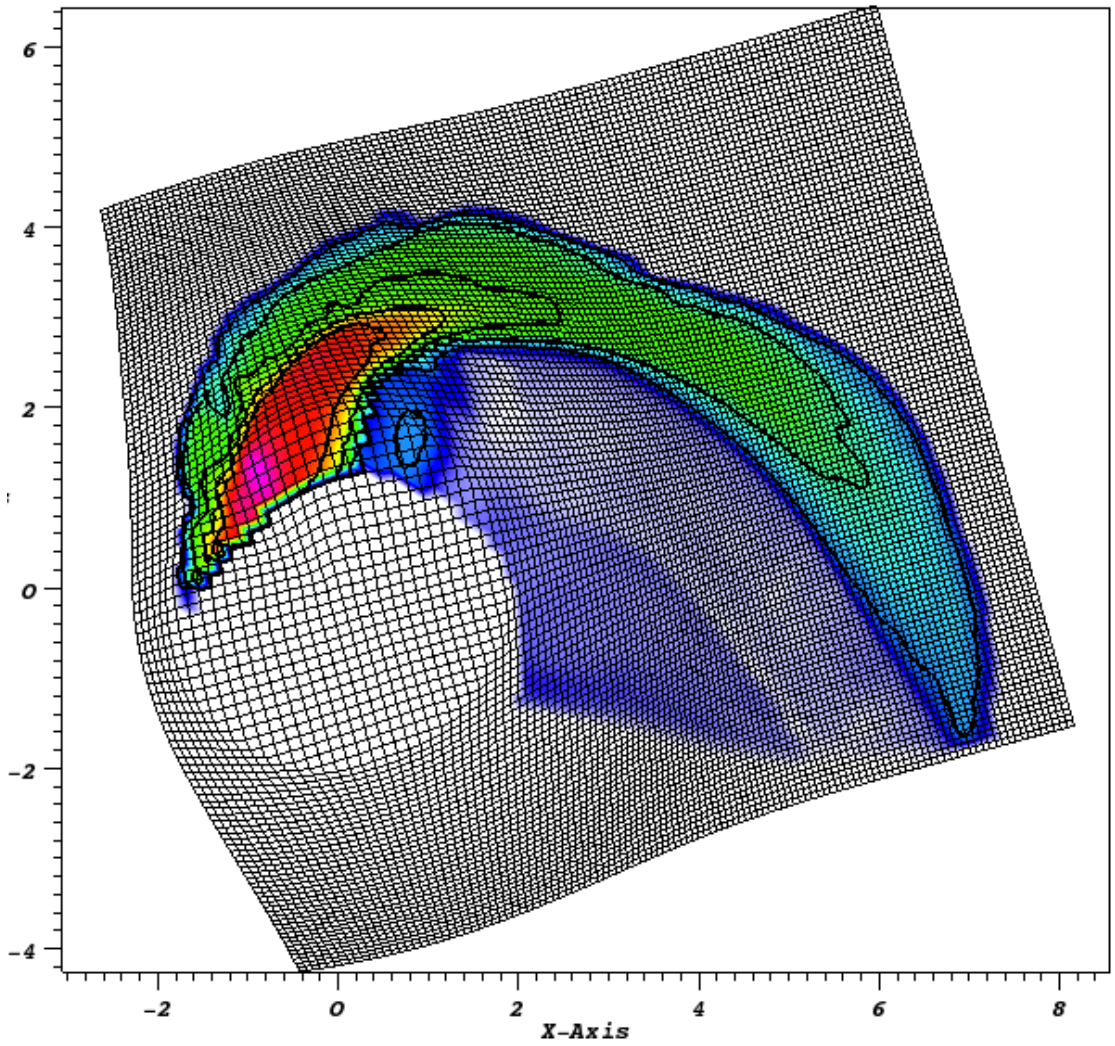

Figure D.1: Neutron star disruption for $q = 7$, $a_{\rm BH}/M_{\rm BH} = 0.5$, in the equatorial plane of the binary. Density contours are shown for $\rho_0 = 10^{-2,-3,-4,-5,-6} M_{\rm BH}^{-2}$. The axis are in units of the BH mass, with $M_{\rm BH} \approx 15{\rm km}$, and use the inertial coordinates — the distortion of the finite difference grid is due to the map used to keep the apparent horizon circular in the grid coordinates. Most of the available mass is immediately accreted onto the black hole, and we have nearly no tidal tail.

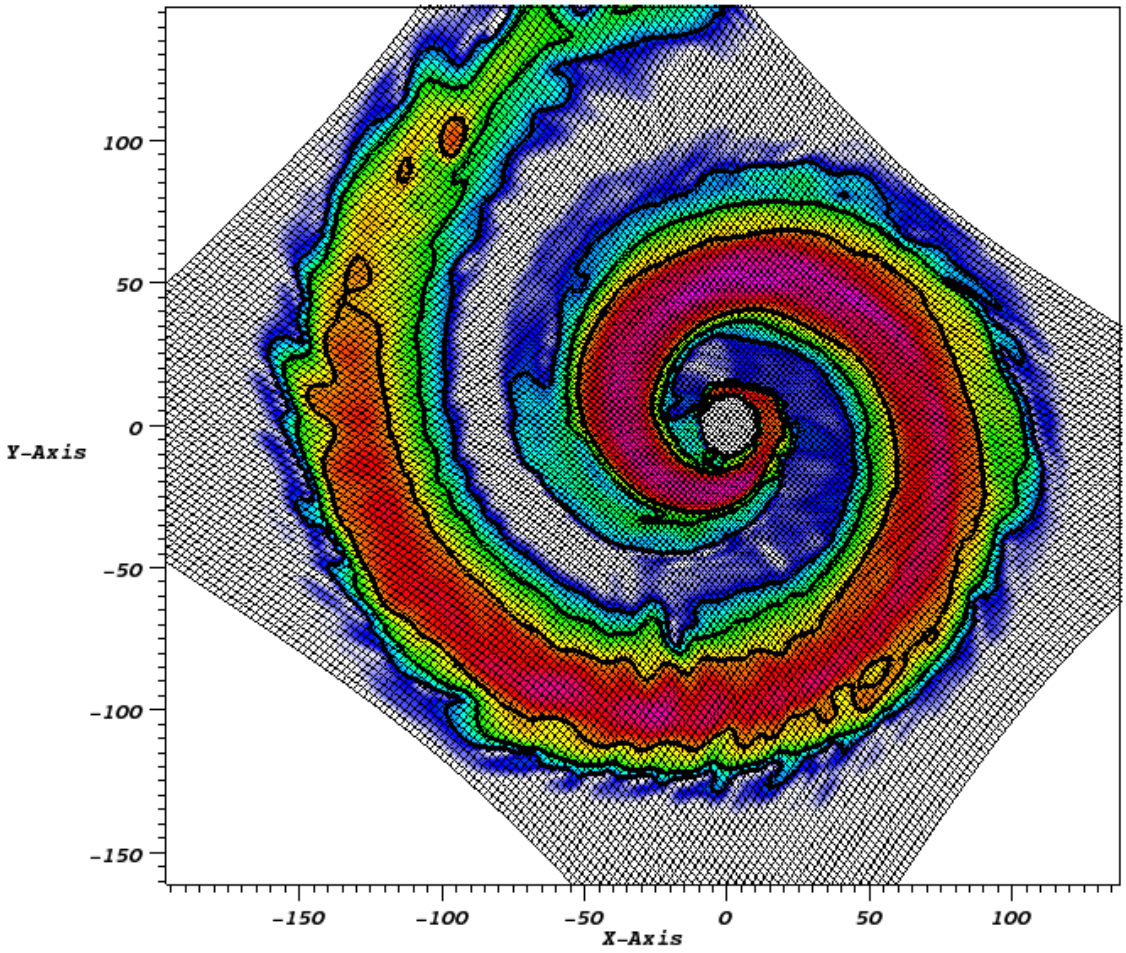

Figure D.2: Neutron star disruption for $q = 7$, $a_{\rm BH}/M_{\rm BH} = 0.7$. Density contours are shown for $\rho_0 = 10^{-5,-6,-7} M_{\rm BH}$. The axis are in solar mass units, with $M_\odot \approx 1.5{\rm km}$. About 10% of the initial matter is still outside of the black hole, in a tidal tail extending to $d \sim 200{\rm km}$.

available for late time accretion and disc formation. This is similar to what was observed for lower mass black holes. For higher spins, more mass is ejected: about 30% of the neutron star mass is in the accretion disc and tidal tail for $a_{\rm BH}/M_{\rm BH} = 0.9$.

Whether material is tidally disrupted or not is particularly important when

studying whether BHNS can power short gamma-ray bursts. Without a heavy, hot accretion disc, BHNS mergers cannot be SGRB progenitors. Thus, if most BHNS binaries have fairly heavy black holes ($M_{\rm BH} \sim 10 M_\odot$), only the systems in which the black hole is rapidly rotating can power bursts. As discussed in the introduction, accretion from the secondary star onto the black hole is probably insufficient to explain the large spins required here: large natal spins are required for enough matter to remain available after merger to lead to a SGRB.

D.2.2 Gravitational waves accuracy

The gravitational waveforms obtained from numerical simulations of compact binaries will be indispensable tools for the detection of gravitational waves by Advanced LIGO and VIRGO, as well as for the determination of the parameters of the systems observed by those detectors. To determine the extent to which numerically generated templates can help, we have to estimate the accuracy of the numerical waveforms, and in particular their phase accuracy. In Fig. D.3, we show the numerical waveform for the $a_{\rm BH}/M_{\rm BH} = 0.7$ configuration described above at 3 different resolutions, while Fig. D.4 shows the phase difference between the various resolutions.

The phase error in the waves remain below $0.1{\rm rad}$ for about 3 orbits, and is still of order $0.2{\rm rad}$ after ~ 4.5 orbits (~ 40 ms). This is a significant improvement compared to the simulations from Chapter 4, which had similar phase errors after $1-2$ orbits. This is due mostly to the use of higher resolution, as well as improvements to the initial data and the fact that errors are generally smaller when the binaries are more widely separated.

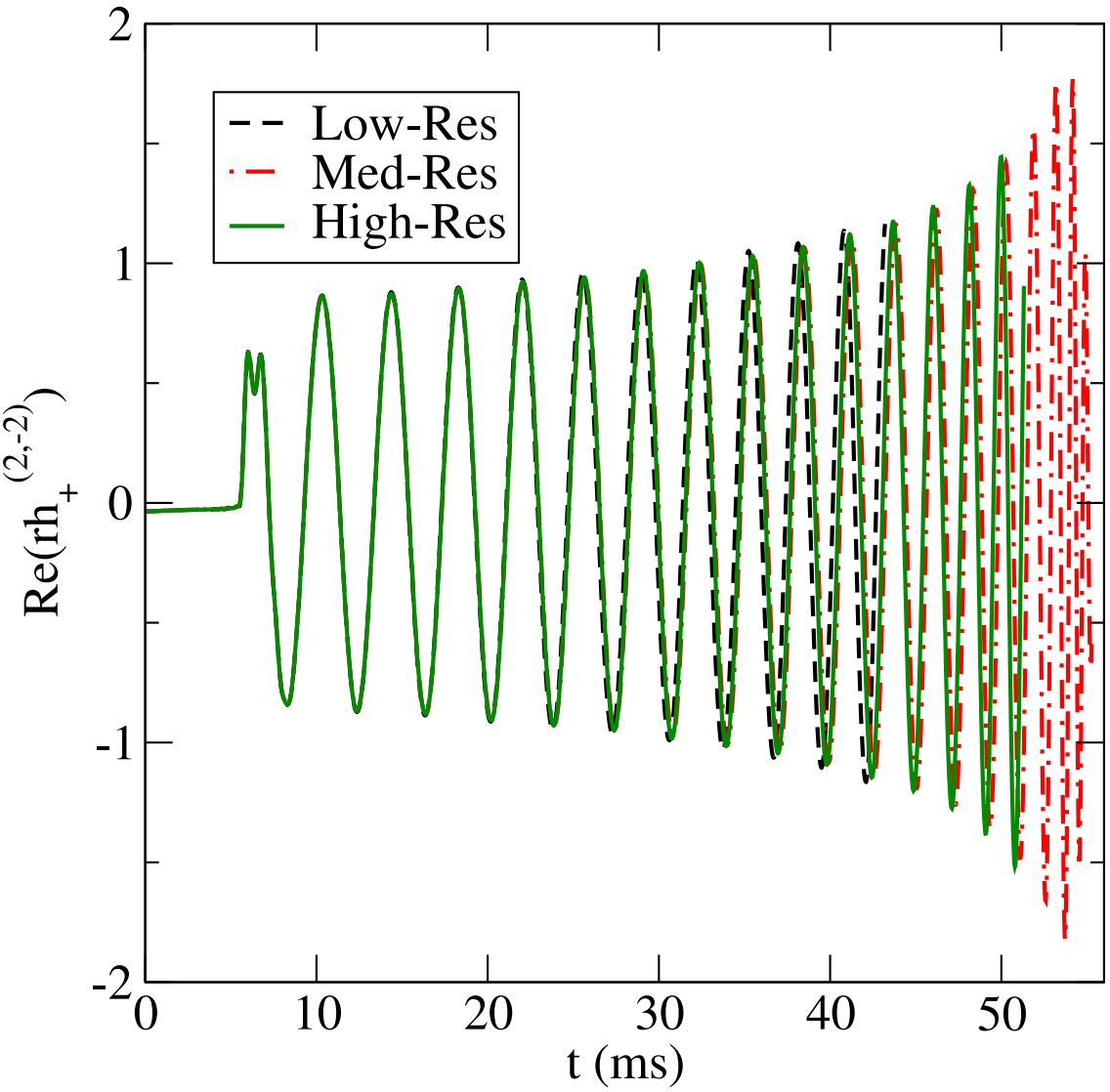

Figure D.3: Strain of the gravitational wave emitted in the $l = 2$, $m = -2$ mode by a BHNS binary with $q = 1:7$ and $a_{\rm BH} = 0.7 M_{\rm BH}$. We show the numerical waveform at three different resolutions.

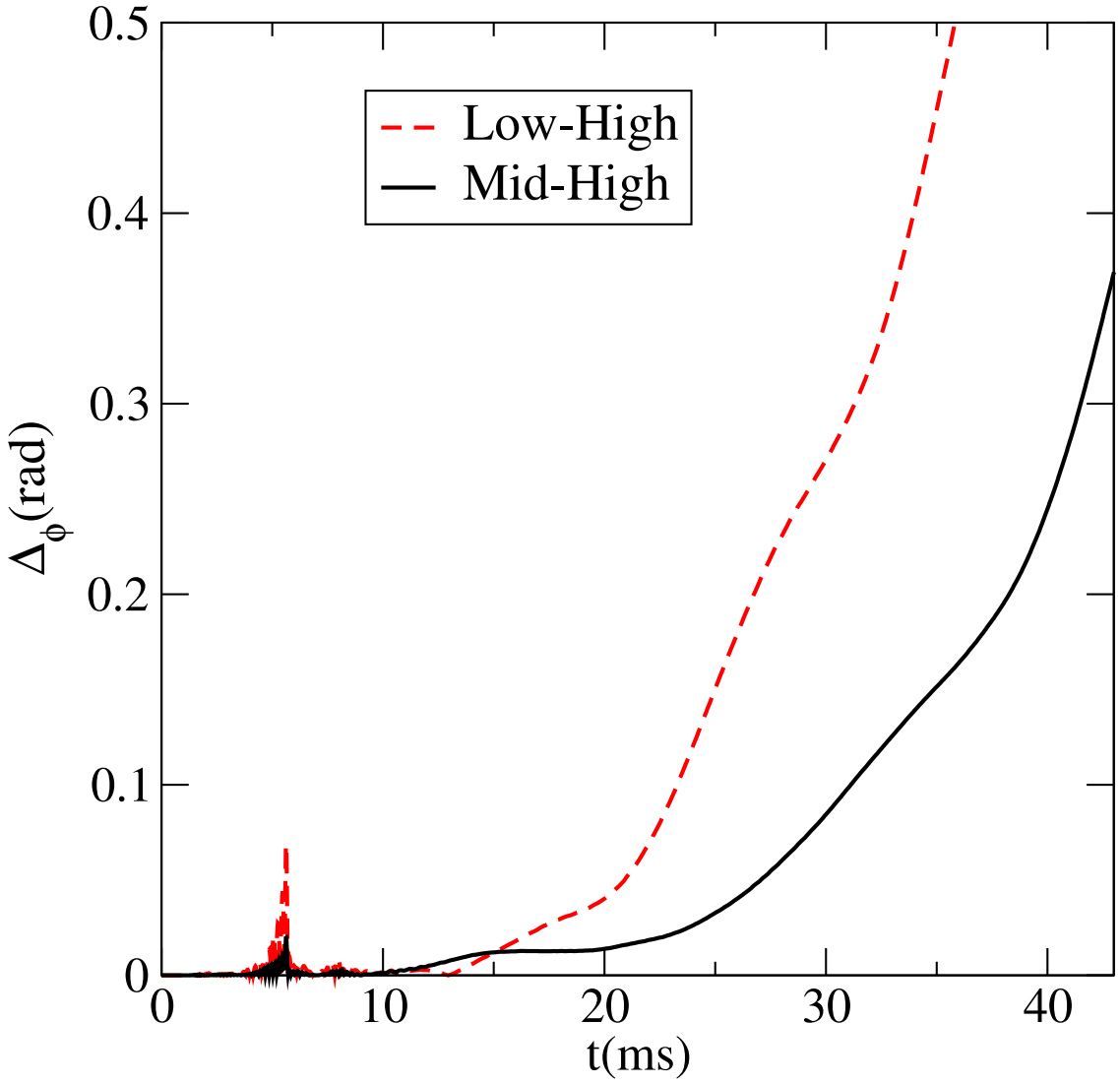

Figure D.4: Phase difference between the gravitational waves shown in Fig. D.3, for the first 10 cycles.

BIBLIOGRAPHY

[1] http://www.black-holes.org/explore2.html.

[2] http://www.black-holes.org/SpEC.html.

[3] Matthew Anderson, Eric Hirschmann, Steven L. Liebling, and David Neilsen. Relativistic MHD with Adaptive Mesh Refinement. *Class. Quant. Grav.*, 23:6503–6524, 2006.

[4] Matthew Anderson, Eric W. Hirschmann, Luis Lehner, Steven L. Liebling, Patrick M. Motl, David Neilsen, Carlos Palenzuela, and Joel E. Tohline. *Phys. Rev. D*, 77:024006, 2008.

[5] I. V. Artemova, G. Bjoernsson, and I. D. Novikov. Modified Newtonian Potentials for the Description of Relativistic Effects in Accretion Disks around Black Holes. *Astrophys. J.*, 461:565, April 1996.

[6] K. G. Arun, A. Buonanno, G. Faye, and E. Ochsner. Higher-order spin effects in the amplitude and phase of gravitational waveforms emitted by inspiraling compact binaries: Ready-to-use gravitational waveforms. *Phys. Rev. D*, 79(10):104023, May 2009.

[7] Luca Baiotti, Bruno Giacomazzo, and Luciano Rezzolla. Accurate evolutions of inspiralling neutron-star binaries: prompt and delayed collapse to black hole. arXiv:0804.0594v1.

[8] John G. Baker, Joan Centrella, Dae-Il Choi, Michael Koppitz, and James van Meter. Gravitational wave extraction from an inspiraling configuration of merging black holes. *Phys. Rev. Lett.*, 96:111102, 2006.

[9] S. A. Balbus and J. F. Hawley. Instability, turbulence, and enhanced transport in accretion disks. *Reviews of Modern Physics*, 70:1–53, January 1998.

[10] T. W. Baumgarte, G. B. Cook, M. A. Scheel, S. L. Shapiro, and S. A. Teukolsky. General relativistic models of binary neutron stars in quasiequilibrium. *Phys. Rev. D*, 57:7299–7311, 1998.

[11] Thomas W. Baumgarte and Stuart L. Shapiro. Numerical integration of einstein's field equations. *Phys. Rev. D*, 59(2):024007, Dec 1998.

[12] K. Belczynski, R. E. Taam, E. Rantsiou, and M. van der Sluys. Black Hole Spin Evolution: Implications for Short-Hard Gamma-Ray Bursts and Gravitational Wave Detection. *Astrophysj́*, 682:474–486, July 2008.

[13] L. Bildsten and C. Cutler. Tidal interactions of inspiraling compact binaries. *Astrophys. J.*, 400:175–180, November 1992.

[14] Luc Blanchet. Innermost circular orbit of binary black holes at the third post-newtonian approximation. *Phys. Rev. D*, 65:124009, 2002.

[15] M. Boyle. The uncertainty in hybrid gravitational waveforms: Optimizing initial orbital frequencies for binary black-hole simulations. *ArXiv e-prints*, March 2011.

[16] Michael Boyle, Duncan A. Brown, Lawrence E. Kidder, Abdul H. Mroue, Harald P. Pfeiffer, Mark A. Scheel, Gregory B. Cook, and Saul A. Teukolsky. High-accuracy comparison of numerical relativity simulations with post-newtonian expansions. *Phys. Rev. D*, 76:124038, 2007.

[17] M. Campanelli, C. O. Lousto, P. Marronetti, and Y. Zlochower. Accurate evolutions of orbiting black-hole binaries without excision. *Phys. Rev. Lett.*, 96:111101, 2006.

[18] M. Campanelli, C. O. Lousto, and Y. Zlochower. Spinning-black-hole binaries: The orbital hang-up. *Phys. Rev. D*, 74(4):041501–+, August 2006.

[19] M. Campanelli, C. O. Lousto, Y. Zlochower, and D. Merritt. Maximum Gravitational Recoil. *Physical Review Letters*, 98(23):231102–+, June 2007.

[20] Matthew Caudill, Gregory B. Cook, Jason D. Grigsby, and Harald P. Pfeiffer. Circular orbits and spin in black hole initial data. *Phys. Rev. D*, 74:064011, 2006.

[21] W.-X. Chen and A. M. Beloborodov. Neutrino-cooled Accretion Disks around Spinning Black Holes. *Astrophys. J.*, 657:383–399, March 2007.

[22] P. Colella and P. R. Woodward. The Piecewise Parabolic Method (PPM) for Gas-Dynamical Simulations. *Journal of Computational Physics*, 54:174–201, September 1984.

[23] Gregory B. Cook and Harald P. Pfeiffer. *Phys. Rev. D*, 70:104016, 2004.

[24] Gregory B. Cook and Harald P. Pfeiffer. Excision boundary conditions for black hole initial data. *Phys. Rev. D*, 70:104016, 2004.

[25] Gregory B. Cook and Bernard F. Whiting. Approximate killing vectors on s^2. *Phys. Rev. D*, 76:041501(R), 2007.

[26] M. D. Duez, F. Foucart, L. E. Kidder, C. D. Ott, and S. A. Teukolsky. Equation of state effects in black hole-neutron star mergers. *Classical and Quantum Gravity*, 27(11):114106–+, June 2010.

[27] M. D. Duez, P. Marronetti, S. L. Shapiro, and T. W. Baumgarte. *Phys. Rev. D*, 67:024004, 2003.

[28] Matthew D. Duez, Francois Foucart, Lawrence E. Kidder, Harald P. Pfeiffer, Mark A. Scheel, and Saul A. Teukolsky. Evolving black hole-neutron star binaries in general relativity using pseudospectral and finite difference methods. *Phys. Rev. D*, 78:104015, 2008.

[29] Matthew D. Duez, Lawrence E. Kidder, and Saul A. Teukolsky. Evolving relativistic fluid spacetimes using pseudospectral methods and finite differencing. arXiv:gr-qc/0702126v1, 2007.

[30] EGO-VIRGO web page. http://www.ego-gw.it.

[31] Zachariah B. Etienne et al. Fully General Relativistic Simulations of Black Hole- Neutron Star Mergers. *Phys. Rev.*, D77:084002, 2008.

[32] Zachariah B. Etienne, Joshua A. Faber, Yuk Tung Liu, Stuart L. Shapiro, Keisuke Taniguchi, and Thomas W. Baumgarte. Fully general relativistic simulations of black hole-neutron star mergers. *Phys. Rev. D*, 77:084002, 2008.

[33] Zachariah B. Etienne, Yuk Tung Liu, Stuart L. Shapiro, and Thomas W. Baumgarte. Relativistic Simulations of Black Hole-Neutron Star Mergers: Effects of black-hole spin. *Phys. Rev.*, D79:044024, 2009.

[34] J. A. Faber, T. W. Baumgarte, Z. B. Etienne, S. L. Shapiro, and K. Taniguchi. Relativistic hydrodynamics in the presence of puncture black holes. *Phys.Rev.D.*, 76(10):104021–+, November 2007.

[35] Joshua A. Faber, Thomas W. Baumgarte, Zachariah B. Etienne, Stuart L.

Shapiro, and Keisuke Taniguchi. Relativistic hydrodynamics in the presence of puncture black holes. *Phys. Rev.*, D76:104021, 2007.

[36] Joshua A. Faber, Thomas W. Baumgarte, Stuart L. Shapiro, Keisuke Taniguchi, and Frederic A. Rasio. The Dynamical Evolution of Black Hole-Neutron Star Binaries in General Relativity: Simulations of Tidal Disruption. *Phys. Rev.*, D73:024012, 2006.

[37] G. Faye, L. Blanchet, and A. Buonanno. Higher-order spin effects in the dynamics of compact binaries. I. Equations of motion. *Phys. Rev. D*, 74(10):104033–+, November 2006.

[38] V. Ferrari, L. Gualtieri, and F. Pannarale. Neutron star tidal disruption in mixed binaries: The imprint of the equation of state. *Phys. Rev. D*, 81:064026, March 2010.

[39] F. Foucart, M. D. Duez, L. E. Kidder, and S. A. Teukolsky. Black hole-neutron star mergers: Effects of the orientation of the black hole spin. *Phys.Rev.D.*, 83(2):024005–+, January 2011.

[40] Francois V. Foucart, Harald P. Pfeiffer, Lawrence E. Kidder, and Saul A. Teukolsky. *Phys. Rev.*, D77:124051, 2008.

[41] P. C. Fragile and P. Anninos. Hydrodynamic Simulations of Tilted Thick-Disk Accretion onto a Kerr Black Hole. *Astrophys. J.*, 623:347–361, April 2005.

[42] P. C. Fragile and O. M. Blaes. Epicyclic Motions and Standing Shocks in Numerically Simulated Tilted Black Hole Accretion Disks. *Astrophys. J.*, 687:757–766, November 2008.

[43] P. C. Fragile, C. C. Lindner, P. Anninos, and J. D. Salmonson. Application of the Cubed-Sphere Grid to Tilted Black Hole Accretion Disks. *Astrophys. J.*, 691:482–494, January 2009.

[44] B. Giacomazzo, L. Rezzolla, and L. Baiotti. Can magnetic fields be detected during the inspiral of binary neutron stars? pages L313+, September 2009.

[45] Eric Gourgoulhon, Philippe Grandclement, Keisuke Taniguchi, Jean-Alain Marck, and Silvano Bonazzola. Quasiequilibrium sequences of

synchronized and irrotational binary neutron stars in general relativity. i. method and tests. *Phys. Rev. D*, 63:064029, 2001.

[46] Philippe Grandclement. Accurate and realistic initial data for black hole-neutron star binaries. *Phys. Rev. D*, 74:124002, 2006.

[47] C. Gundlach, G. Calabrese, I. Hinder, and J. M. Martin-Garcia. Constraint damping in the z4 formulation and harmonic gauge. *Class. Quantum Grav.*, 22:3767–3774, 2005.

[48] K. Hebeler, J. M. Lattimer, C. J. Pethick, and A. Schwenk. Constraints on Neutron Star Radii Based on Chiral Effective Field Theory Interactions. *Physical Review Letters*, 105(16):161102–+, October 2010.

[49] J. W. T. Hessels, S. M. Ransom, I. H. Stairs, P. C. C. Freire, V. M. Kaspi, and F. Camilo. A Radio Pulsar Spinning at 716 Hz. *Science*, 311:1901–1904, March 2006.

[50] I. Horváth. A Third Class of Gamma-Ray Bursts? *Astrophys.J.*, 508:757–759, December 1998.

[51] R. A. Hulse and J. H. Taylor. Discovery of a pulsar in a binary system. *Astroph.J.*, 195:L51–L53, January 1975.

[52] H.-T. Janka, T. Eberl, M. Ruffert, and C. L. Fryer. Black Hole-Neutron Star Mergers as Central Engines of Gamma-Ray Bursts. *Astrophys. J. Lett.*, 527:L39–L42, December 1999.

[53] Ke-Jian Jin and Wai-Mo Suen. *Phys. Rev. Lett.*, 98:131101, 2007.

[54] L. E. Kidder. Coalescing binary systems of compact objects to 2.5 post-Newtonian order. V. Spin effects. *Phys. Rev. D*, 52:821–847, July 1995.

[55] R. W. Klebesadel, I. B. Strong, and R. A. Olson. Observations of Gamma-Ray Bursts of Cosmic Origin. *Astrophys.J.*, 182:L85+, June 1973.

[56] C. S. Kochanek. Coalescing binary neutron stars. *Astrophys. J.*, 398:234–247, October 1992.

[57] C. Kouveliotou, C. A. Meegan, G. J. Fishman, N. P. Bhat, M. S. Briggs, T. M. Koshut, W. S. Paciesas, and G. N. Pendleton. Identification of two classes of gamma-ray bursts. *Astroph.J.*, 413:L101–L104, August 1993.

[58] J. M. Lattimer and D. N. Schramm. Black-hole-neutron-star collisions. *Astrophys. J. Lett.*, 192:L145–L147, September 1974.

[59] James M. Lattimer and F. Douglas Swesty. A Generalized equation of state for hot, dense matter. *Nucl. Phys.*, A535:331–376, 1991.

[60] W. H. Lee and E. Ramirez-Ruiz. The progenitors of short gamma-ray bursts. *New Journal of Physics*, 9:17–+, January 2007.

[61] William H. Lee. Newtonian hydrodynamics of the coalescence of black holes with neutron stars III: Irrotational binaries with a stiff equation of state. *Mon. Not. Roy. Astron. Soc.*, 318:606, 2000.

[62] William H. Lee. Newtonian hydrodynamics of the coalescence of black holes with neutron stars IV: Irrotational binaries with a soft equation of state. *Mon. Not. Roy. Astron. Soc.*, 328:583, 2001.

[63] William H. Lee and Wlodzimierz Kluzniak. Newtonian Hydrodynamics of the Coalescence of Black Holes with Neutron Stars I: Tidally locked binaries with a stiff equation of state. *Astrophys. J.*, 526:178, 1999.

[64] William H. Lee and Wlodzimierz Kluzniak. Newtonian hydrodynamics of the coalescence of black holes with neutron stars II: Tidally locked binaries with a soft equation of state. *Mon. Not. Roy. Astron. Soc.*, 308:780, 1999.

[65] William H. Lee and Enrico Ramirez-Ruiz. The progenitors of short gamma-ray bursts. *New J. Phys.*, 9:17, 2007.

[66] William H. Lee, Enrico Ramirez-Ruiz, and Dany Page. Dynamical evolution of neutrino–cooled accretion disks: detailed microphysics, lepton-driven convection, and global energetics. *Astrophys. J.*, 632:421–437, 2005.

[67] LIGO web page. http://www.ligo.caltech.edu.

[68] Lee Lindblom, Mark A. Scheel, Lawrence E. Kidder, Robert Owen, and Oliver Rinne. *Class. Quant. Grav.*, 23:S447, 2006.

[69] Geoffrey Lovelace. PhD thesis, California Institute of Technology, 2007. http://resolver.caltech.edu/CaltechETD:etd-05232007-115433.

[70] Geoffrey Lovelace, Robert Owen, Harald P. Pfeiffer, and Tony Chu. Binary-black-hole initial data with nearly-extremal spins. arXiv:0805.4192.

[71] Geoffrey Lovelace, Robert Owen, Harald P. Pfeiffer, and Tony Chu. Binary-black-hole initial data with nearly-extremal spins. *Phys. Rev.*, D78:084017, 2008.

[72] I. MacDonald, S. Nissanke, and H. P. Pfeiffer. Suitability of post-Newtonian/numerical-relativity hybrid waveforms for gravitational wave detectors. *ArXiv e-prints*, February 2011.

[73] J. E. McClintock, R. Narayan, S. W. Davis, L. Gou, A. Kulkarni, J. A. Orosz, R. F. Penna, R. A. Remillard, and J. F. Steiner. Measuring the spins of accreting black holes. *Classical and Quantum Gravity*, 28(11):114009–+, June 2011.

[74] C. A. Meegan, G. J. Fishman, R. B. Wilson, J. M. Horack, M. N. Brock, W. S. Paciesas, G. N. Pendleton, and C. Kouveliotou. Spatial distribution of gamma-ray bursts observed by BATSE. *Nature*, 355:143–145, January 1992.

[75] M. A. Miller, P. Gressman, and Wai-Mo Suen. *Phys. Rev. D*, 69:064026, 2004.

[76] Thierry Mora and Clifford M. Will. A post-newtonian diagnostic of quasi-equilibrium binary configurations of compact objects. *Phys. Rev. D*, 71:129901(E), 2005.

[77] S. C. Noble, C. F. Gammie, J. C. McKinney, and L. Del Zanna. Primitive Variable Solvers for Conservative General Relativistic Magnetohydrodynamics. *Astroph.J.*, 641:626–637, April 2006.

[78] E. O'Connor and C. D. Ott. A New Open-Source Code for 1D Stellar Collapse A New Open-Source Code for Spherically-Symmetric Stellar Collapse to Neutron Stars and Black Holes. *Preprint*, pages astro–ph: 0912.2393, December 2009.

[79] E. O'Connor and C. D. Ott. Thermal Effects on Black Hole Formation in Failed Core-Collapse Supernovae. *ArXiv e-prints*, March 2011.

[80] C. D. Ott, C. Reisswig, E. Schnetter, E. O'Connor, U. Sperhake, F. Löffler,

P. Diener, E. Abdikamalov, I. Hawke, and A. Burrows. Dynamics and Gravitational Wave Signature of Collapsar Formation. *Physical Review Letters*, 106(16):161103–+, April 2011.

[81] Robert Owen. PhD thesis, California Institute of Technology, 2007. http://resolver.caltech.edu/CaltechETD:etd-05252007-143511.

[82] F. Özel, G. Baym, and T. Güver. Astrophysical measurement of the equation of state of neutron star matter. *Phys.Rev.D.*, 82(10):101301–+, November 2010.

[83] B. Paczynski. Cosmological gamma-ray bursts. *Acta Astronomica*, 41:257–267, 1991.

[84] B. Paczyński and P. J. Wiita. Thick accretion disks and supercritical luminosities. 88:23–31, August 1980.

[85] P. C. Peters. Gravitational radiation and the motion of two point masses. *Phys. Rev.*, 136(4B):B1224–B1232, Nov 1964.

[86] Harald P. Pfeiffer. PhD thesis, Cornell University, 2003. arXiv:gr-qc/0510016v1.

[87] Harald P. Pfeiffer. PhD thesis, Cornell University, 2003. arXiv:gr-qc/0510016v1.

[88] Harald P. Pfeiffer, Duncan A. Brown, Lawrence E. Kidder, Lee Lindblom, Geoffrey Lovelace, and Mark A. Scheel. Reducing orbital eccentricity in binary black hole simulations. *Class. Quantum Grav.*, 24:S59–S81, 2007.

[89] Harald P. Pfeiffer, Gregory B. Cook, and Saul A. Teukolsky. *Phys. Rev. D*, 66:024047, 2002.

[90] Harald P. Pfeiffer, Gregory B. Cook, and Saul A. Teukolsky. *Phys. Rev. D*, 66:024047, 2002.

[91] Harald P. Pfeiffer et al. *Class. Quantum Grav.*, 24:S59, 2007.

[92] Harald P. Pfeiffer, Lawrence E. Kidder, Mark A. Scheel, and Saul A. Teukolsky. A multidomain spectral method for solving elliptic equations. *Comput. Phys. Commun.*, 152:253–273, 2003.

[93] Harald P. Pfeiffer, Lawrence E. Kidder, Mark A. Scheel, and Saul A. Teukolsky. A multidomain spectral method for solving ellipticequations. *Comput. Phys. Commun.*, 152:253–273, 2003.

[94] Harald P. Pfeiffer and James W. York. Extrinsic curvature and the einstein constraints. *Phys. Rev. D*, 67:044022, 2003.

[95] Harald P. Pfeiffer and James W. York. Uniqueness and non-uniqueness in the einstein constraints. *Phys. Rev. Lett.*, 95:091101, 2005.

[96] R. Popham, S. E. Woosley, and C. Fryer. Hyperaccreting Black Holes and Gamma-Ray Bursts. *Astrophys. J.*, 518:356–374, June 1999.

[97] Frans Pretorius. Evolution of binary black hole spacetimes. *Phys. Rev. Lett.*, 95:121101, 2005.

[98] Frans Pretorius. Binary black hole coalescence. arXiv:0710.1338v1, 2008.

[99] E. Rantsiou, S. Kobayashi, P. Laguna, and F. A. Rasio. Mergers of Black Hole-Neutron Star Binaries. I. Methods and First Results. *Astrophys. J.*, 680:1326–1349, June 2008.

[100] J. S. Read, C. Markakis, M. Shibata, K. Uryū, J. D. E. Creighton, and J. L. Friedman. Measuring the neutron star equation of state with gravitational wave observations. *Phys.Rev.D.*, 79(12):124033–+, June 2009.

[101] Jocelyn S. Read et al. Measuring the neutron star equation of state with gravitational wave observations. *Phys. Rev.*, D79:124033, 2009.

[102] L. Rezzolla, B. Giacomazzo, L. Baiotti, J. Granot, C. Kouveliotou, and M. A. Aloy. The Missing Link: Merging Neutron Stars Naturally Produce Jet-like Structures and Can Power Short Gamma-ray Bursts. *Astrophys.J.*, 732:L6+, May 2011.

[103] S. Rosswog. Mergers of Neutron Star-Black Hole Binaries with Small Mass Ratios: Nucleosynthesis, Gamma-Ray Bursts, and Electromagnetic Transients. *Astrophys. J.*, 634:1202–1213, December 2005.

[104] Stephan Rosswog, R. Speith, and G. A. Wynn. Accretion dynamics in neutron star black hole binaries. *Mon. Not. Roy. Astron. Soc.*, 351:1121, 2004.

[105] M. Ruffert and H. Th. Janka. Polytropic neutron star - black hole merger simulations with a Paczynski-Wiita potential. *Preprint*, pages astro–ph: 0906.3998, 2009.

[106] LIGO Scientific Colaboration and VIRGO Scientific Colaboration. *Classical and Quantum Gravity*, 27(17):173001–+, September 2010.

[107] LORENE web page. http://www.lorene.obspm.fr.

[108] M. A. Scheel, H. P. Pfeiffer, L. Lindblom, L. E. Kidder, O. Rinne, and S. A. Teukolsky. Solving Einstein's equations with dual coordinate frames. *Phys. Rev. D*, 74(10):104006–+, November 2006.

[109] Erik Schnetter, Scott H. Hawley, and Ian Hawke. Evolutions in 3D numerical relativity using fixed mesh refinement. *Class. Quant. Grav.*, 21:1465–1488, 2004.

[110] S. Setiawan, M. Ruffert, and H.-T. Janka. Three-dimensional simulations of non-stationary accretion by remnant black holes of compact object mergers. *Astron. and Astrophys.*, 458:553–567, November 2006.

[111] H. Shen, H. Toki, K. Oyamatsu, and K. Sumiyoshi. Relativistic Equation of State of Nuclear Matter for Supernova and Neutron Star. *Nucl. Phys.*, A637:435–450, 1998.

[112] H. Shen, H. Toki, K. Oyamatsu, and K. Sumiyoshi. Relativistic Equation of State of Nuclear Matter for Supernova Explosion. *Prog. Theor. Phys.*, 100:1013–1031, November 1998.

[113] M. Shibata and T. Nakamura. Evolution of three-dimensional gravitational waves: Harmonic slicing case. *Phys.Rev.D.*, 52:5428–5444, November 1995.

[114] M. Shibata, Y. Sekiguchi, and R. Takahashi. Magnetohydrodynamics of Neutrino-Cooled Accretion Tori around a Rotating Black Hole in General Relativity. *Prog. Theor. Phys.*, 118:257–302, August 2007.

[115] M. Shibata, K. Taniguchi, and K. Uryu. *Phys. Rev. D*, 71:084021, 2005.

[116] Masaru Shibata. A relativistic formalism for computation of irrotational binary stars in quasi equilibrium states. *Phys. Rev. D*, 58:024012, 1998.

[117] Masaru Shibata, Koutarou Kyutoku, Tetsuro Yamamoto, and Keisuke Taniguchi. Gravitational waves from black hole-neutron star binaries I: Classification of waveforms. *Phys. Rev.*, D79:044030, 2009.

[118] Masaru Shibata and Keisuke Taniguchi. Merger of black hole and neutron star in general relativity: Tidal disruption, torus mass, and gravitational waves. *Phys. Rev. D*, 77:084015, 2008.

[119] Masaru Shibata and Keisuke Taniguchi. Merger of black hole and neutron star in general relativity: Tidal disruption, torus mass, and gravitational waves. *Phys. Rev.*, D77:084015, 2008.

[120] Masaru Shibata and Koji Uryu. Simulation of merging binary neutron stars in full general relativity: $\gamma = 2$ case. *Phys. Rev. D*, 61:064001, 2000.

[121] Masaru Shibata and Koji Uryu. Merger of black hole - neutron star binaries: Nonspinning black hole case. *Phys. Rev.*, D74:121503, 2006.

[122] Masaru Shibata and Koji Uryu. Merger of black hole-neutron star binaries in full general relativity. *Class. Quant. Grav.*, 24:S125–S138, 2007.

[123] Carlos F. Sopuerta, Ulrich Sperhake, and Pablo Laguna. Hydro-without-hydro framework for simulations of black hole-neutron star binaries. *Class. Quantum Grav.*, 23:S579–S598, 2006.

[124] B. C. Stephens, W. E. East, and F. Pretorius. Eccentric Black Hole-Neutron Star Mergers. *ArXiv e-prints*, May 2011.

[125] B. C. Stephens, S. L. Shapiro, and Y. T. Liu. Collapse of magnetized hypermassive neutron stars in general relativity: Disk evolution and outflows. *Phys. Rev. D*, 77(4):044001–+, February 2008.

[126] V. Suleimanov, J. Poutanen, M. Revnivtsev, and K. Werner. Neutron star stiff equation of state derived from cooling phases of the X-ray burster 4U 1724-307. *ArXiv e-prints*, April 2010.

[127] R. Surman, G. C. McLaughlin, M. Ruffert, H.-T. Janka, and W. R. Hix. r-Process Nucleosynthesis in Hot Accretion Disk Flows from Black Hole-Neutron Star Mergers. *Astrophys. J. Lett.*, 679:L117–L120, June 2008.

[128] Keisuke Taniguchi, Thomas W. Baumgarte, Joshua A. Faber, and Stuart L.

Shapiro. Black hole-neutron star binaries in general relativity: Effects of neutron star spin. *Phys. Rev. D*, 72:044008, 2005.

[129] Keisuke Taniguchi, Thomas W. Baumgarte, Joshua A. Faber, and Stuart L. Shapiro. Quasiequilibrium sequences of black hole-neutron star binaries in general relativity. *Phys. Rev. D*, 74:041502(R), 2006.

[130] Keisuke Taniguchi, Thomas W. Baumgarte, Joshua A. Faber, and Stuart L. Shapiro. Quasiequilibrium black hole-neutron star binaries in general relativity. *Phys. Rev. D*, 75:084005, 2007.

[131] Keisuke Taniguchi, Thomas W. Baumgarte, Joshua A. Faber, and Stuart L. Shapiro. Relativistic black hole-neutron star binaries in quasiequilibrium: effects of the black hole excision boundary condition. *Phys. Rev. D*, 77:044003, 2008.

[132] J. H. Taylor, L. A. Fowler, and P. M. McCulloch. Measurements of general relativistic effects in the binary pulsar PSR 1913+16. *Nature*, 277:437–440, February 1979.

[133] Saul A. Teukolsky. Irrotational binary neutron stars in quasiequilibrium in general relativity. *Astrophys. J.*, 504:442, 1998.

[134] B. van Leer. Towards the Ultimate Conservative Difference Scheme. IV. A New Approach to Numerical Convection. *J. Comput. Phys.*, 23:276–299, 1977.

[135] S. E. Woosley and J. S. Bloom. The Supernova Gamma-Ray Burst Connection. *Annual Review of Astronomy & Astrophysics*, 44:507–556, September 2006.

[136] Tetsuro Yamamoto, Masaru Shibata, and Keisuke Taniguchi. Simulating coalescing compact binaries by a new code SACRA. *Phys. Rev.*, D78:064054, 2008.

[137] James W. York. In L. L. Smarr, editor, *Sources of Gravitational Radiation*, page 83. Cambridge University Press, Cambridge, England, 1979.

[138] James W. York. *Phys. Rev. Lett.*, 82:1350, 1999.

[139] James W. York Jr. Conformal "thin sandwich" data for the initial-value problem of general relativity. *Phys. Rev. Lett.*, 82:1350, 1999.